Localization of the large angle foil scattering beam loss caused by the multi-turn charge-exchange injection

博士論文

Localization of the large angle foil scattering beam loss caused by the multi-turn charge-exchange injection (陽子加速器における荷電変換入射起因のビーム損失の研究)

加藤　新一

平成２６年

Abstract

This thesis presents the large-angle foil scattering beam loss as the new loss source for a high intensity proton synchrotron or storage ring. Using the 3-GeV rapid-cycling synchrotron (RCS) of the Japan Accelerator Research Complex as an example, the thesis also presents the appropriate countermeasures. In the high intensity proton synchrotron, the multi-turn charge-exchange injection should be adopted in order to storage a lot of particles in the ring. The injection is divided into some numbers of turns and the each injection beam added to the circulating beam repeatedly. In this scheme, H^- beam is usually adopted as the injection beam and it is converted into proton at the injection point using the charge-exchange foil. Thus, because the circulating beam repeatedly collides with the foil throughout this process, it is scattered during the injection period. The survey results of the RCS indicated that the particles scattered at large angles by the foil caused the significant activation at the downstream of the injection area in the high intensity operation. Because the probability of the large-angle scattering was very low, this loss source had not been understood at first. High-precision simulations focusing on the foil scattering identified the large-angle foil scattering beam loss as a loss source for the first time in the world. This loss is expected to become an issue for future high-intensity proton synchrotrons or storage rings. Therefore, a countermeasure is presented here with the RCS being used as an example. Specifically, localization of the loss has been performed with a new collimator because the large-angle scattering of the beam cannot be handled in principle. A realistic simulation model was developed in order to investigate the localization effect. In particular, the optimization method of the absorber included in the collimator was discussed using the model. As a result, it was confirmed that optimization of the absorber angle, which had not been concerned typically, was important for efficient localization. Moreover, we developed an original beam-based angle optimization method. During the experiments, absorber optimization and the loss reduction were achieved using the newly developed method. In addition, the residual dose was estimated for the case of 1 MW power, which is RCS target power, using the realistic simulation. The results confirmed that the residual dose was approximately 1 mSv/h, which is an acceptable level for machine maintenance, around the highest residual dose area of the RCS. In other words, the limitation preventing the achievement of an intensity of 1 MW could be overcome by the research of this thesis. In addition, it was indicated that further suppression of the loss was possible with modifications of the injection scheme.

This thesis presents a novel comprehensive discussion on the large-angle foil scattering beam loss and its appropriate countermeasure for the first time in the world. Moreover, the localization method for dealing with the loss, which could become the standard method for future accelerators, was established.

Contents

List of Figures

List of Tables

1 Introduction

Recently, proton accelerators have been applied to numerous uses. In particle physics, nuclear physics or material science experiments, it is used as a source of secondary beams that include neutrons, muons, kaons, neutrinos, and so on. In order to produce a large number of events and to efficiently perform these experiments, intense secondary beams are required. Therefore, the proton accelerator is desired to be raised the beam power which is the product of the energy and current. Concretely, 1 or multi-MW class proton accelerators have recently been constructed or planned across the world.

In the high energy region, the production value of the secondary beams does not increase with an increase in energy. Therefore, a high-intensity beam whose energy exceeds the thresholds for efficient production should be formed by increasing the beam current. For high-intensity proton accelerators, the beam intensity is restricted by the amount of the beam loss because this loss causes activation. When the activation level is too high, maintenance becomes impossible considering the exposure to radiation. Therefore, the reduction of the beam loss is very important to achieve high-intensity. Specifically, 1 mSv/h is an acceptable level around the each equipment.

In the high-intensity accelerator, some new beam loss sources appear differently from the low-intensity case, for example, a space-charge force which is repulsive force due to the each particle charge, a non-linear force created by magnets that have large apertures, and so on. These new loss sources should be comprehended correctly and the beam loss should be reduced as much as possible during research.

Therefore, the purpose of this thesis was comprehending the characteristic beam loss source of the high-intensity proton accelerator and solving its loss problem. In particular, this study focused on the large-angle foil scattering beam loss caused by the multi-turn charge-exchange injection, which is required by the high-intensity proton synchrotron or storage ring.

The multi-turn charge-exchange injection and the large-angle foil scattering beam loss are as follows. To achieve the high-intensity in the proton synchrotron or storage ring, it is necessary to inject and store a large number of beam in the ring. Therefore, beam injection is often divided into some number of turns and the each injection beam added to the circulating beam repeatedly. This scheme is the multi-turn injection. However, if the injection beam and the circulating beam have the same charge, it is impossible to lead the injection beam to the same phase-space coordinates occupied by the circulating beam at the injection point. This principle is known as Liouville's theorem. Therefore, the H^- ion, which has an opposite charge to that of the circulating beam, must be used as an injection beam. In this case, the charge-exchange foil is placed at the injection point in order to convert H^- ions into protons. This injection scheme is known as the multi-turn charge-exchange injection. When this method is adopted, the circulating beam current can theoretically be increased infinitely without upgrading the injection beam current. Although this injection scheme is a powerful technique for forming a high intensity beam, the circulating beam also repeatedly collides with the foil and it is scattered during the injection period. In particular, the particles scattered at large angles are lost directly without circulating and then they cause activation at downstream of the injection area. This is the large-angle foil scattering beam loss.

This loss can be excluded from the loss sources in the low-intensity accelerator up to present because the foil is very thin and the energy of the particles colliding with it is generally very high. However, in the high-intensity case, this loss becomes conspicuous though the probability of large-angle scattering is very low. In other words, this loss is expected to become a basic issue for future high-intensity proton synchrotrons or storage rings. Therefore, this thesis presents a comprehensive discussion on the large-angle foil scattering beam loss and its appropriate countermeasure.

This study was performed using the Japan Proton Accelerator Research Complex (J-PARC) [1] Rapid Cycling Synchrotron (RCS), in which the beam intensity was restricted by the huge activation at the downstream of the injection area, as an example. In this thesis, first, it is described that the large-angle foil scattering beam loss could become an issue using the survey results of the RCS and the simulation results. Second, the countermeasure against the loss is described. Because the large-angle scattering cannot be handled in principle, the localization of the loss was selected with a new collimator. Third, the optimization method of the absorber included in the collimator is described. To investigate the localization effect, a realistic simulation model was developed. As a simulation result, it was indicated that optimization of the absorber angle, which had not been concerned typically, was important for efficient localization. Therefore, I developed an original beam-based angle optimization method. Fourth, the experimental results of the localization with the collimator are described. Finally, the simulation results for the estimation of the residual dose in the case of 1 MW power, which is RCS target power, are described. In addition, the discussion based on the simulation for further suppression of the loss is performed.

In the following sections, an outline of the RCS and the injection scheme are introduced in section 2; the large-angle foil scattering beam loss and the new collimation system as a countermeasure against this loss are introduced in section 3; the optimization of the system is introduced in section 4; the experimental results are discussed in section 5; the simulation results are discussed in section 6 and conclusion is provided in section 7.

2 A high-intensity proton synchrotron and the injection scheme

As introduced in section 1, in the high-intensity proton synchrotron or storage ring, the beam injection is often divided into some number of turns and the each injection beam added to the circulating beam repeatedly in order to store a large number of beams. In addition, the use of H^- ion is required as an injection beam. During injection, H^- ions are converted into protons by the charge-exchange foil placed at the injection point. This injection scheme is known as the multi-turn charge-exchange injection [1] [2]. In this section, this injection scheme, which causes the large-angle foil scattering beam loss, is mainly introduced.

First, the J-PARC RCS where this study was performed is introduced. Next, the multi-turn charge-exchange injection scheme is introduced. The control method of the transverse and longitudinal beam distribution called painting is also introduced. In addition, the charge-exchange foil is introduced.

2.1 Japan Proton Accelerator Research Complex (J-PARC)

The Japan Proton Accelerator Research Complex (J-PARC) is a multi-purpose and multi-disciplinary facility. J-PARC consists of three accelerators and three experiment facilities. Each accelerator serves as a secondary beam source for the experimental facilities. An over view of the J-PARC is shown in Fig. 1. The accelerators are summarized as follows.

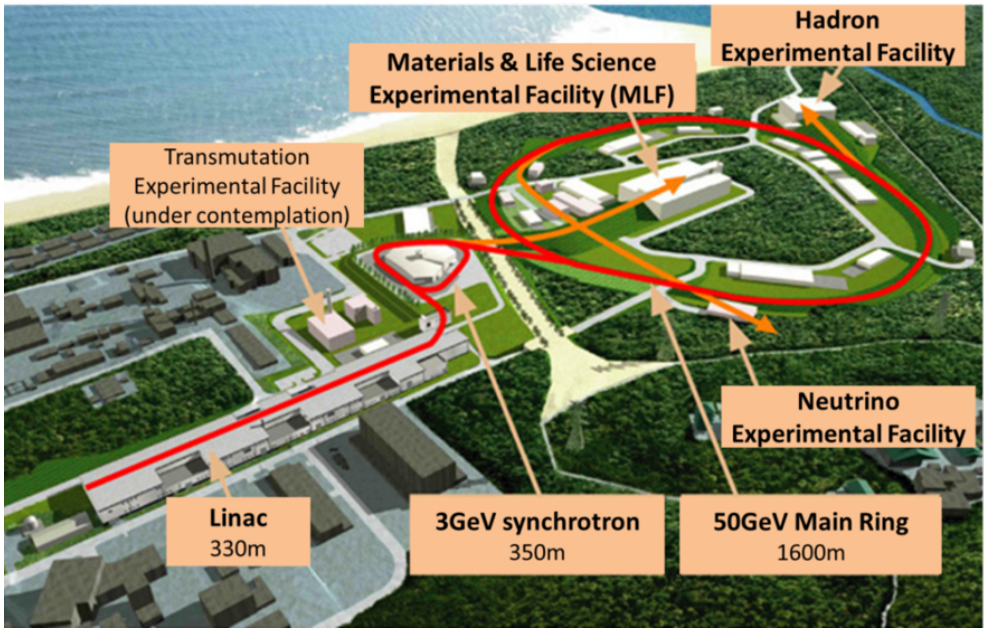

Figure 1: An overview of the J-PARC facilities.

1. Linac
   H^- ions are accelerated up to 400 MeV using the Radio Frequency Quadrupole Linac (RFQ), the Drift Tube Linac (DTL), the Separated-type DTL (SDTL), and

the Annuler Coupled Structure (ACS). Before 2013, the beam energy was 181 MeV because the ACS was not installed.

2. 3-GeV Rapid Cycling Synchrotron (RCS)
   The H^- beams from the Linac are converted into H^+ by the charge-exchange foil at the injection point, and then, they are injected into the ring. Beams are accelerated up to 3 GeV and provided to the Materials & Life Science Experimental Facility (MLF) as a neutron source, and the Main Ring (MR) as an injection beam. The details are provided in the next section.

3. Main Ring (MR)
   The beam from the RCS are accelerated up to 30 GeV with 0.3 Hz repetition. These accelerated beams are provided to the Hadron Experimental Facility using slow extraction and Neutrino Experimental Facility using fast extraction.

The beam energy of the accelerator using fixed target can be roughly classified into two groups: around 1 GeV, used in the Materials and Life Science Research, and more than 10 GeV, applied to nuclear and particle physics experiments. J-PARC is a unique facility because it covers both energy regions in a single facility. J-PARC also aims to achieve the top level of the beam intensity in the world.

2.2 Rapid Cycling Synchrotron (RCS)

The 3-GeV rapid cycling synchrotron (RCS) serves as a proton beam source for the Materials & Life Science Experimental Facility (MLF) and the 50-GeV main ring (MR). The RCS has been providing a 3-GeV proton beam to the MLF since 2008 and during this time the beam intensity has been increased through the beam study [3]. In February 2011, the RCS provided a 220 kW proton beam to the MLF with 181 MeV injection energy [4]. After a long shut down due to the earthquake in 2011, a beam power of 300 kW was achieved in October 2012. Furthermore, through an upgrade of Linac, the RCS provided a 300 kW proton beam with an injection energy of 400 MeV in March 2014 [5]. Further studies and upgrades will be performed in future to achieve a beam power of 1 MW.

An overview of the RCS is shown in Fig. 2. RCS has a three-fold symmetric lattice with a circumference of 348.333 m. The transverse collimator and the injection systems, the extraction systems, and the RF cavity are placed in each straight section. The fundamental RCS parameters are listed in Table. 1. As shown in Table. 1, the RCS consists of 24 bending magnets, 60 quadrupole magnets and 18 sextupole magnets. The quadrupole magnets are divided into 7 families and this large number of families makes it possible to change the lattice parameters flexibly. The RCS even has 54 electro static Beam Position Monitors (BPM) and 52 steering magnets. By detecting the beam position and feeding back the required kick angles to steering magnets, it makes possible to correct closed orbit successfully.

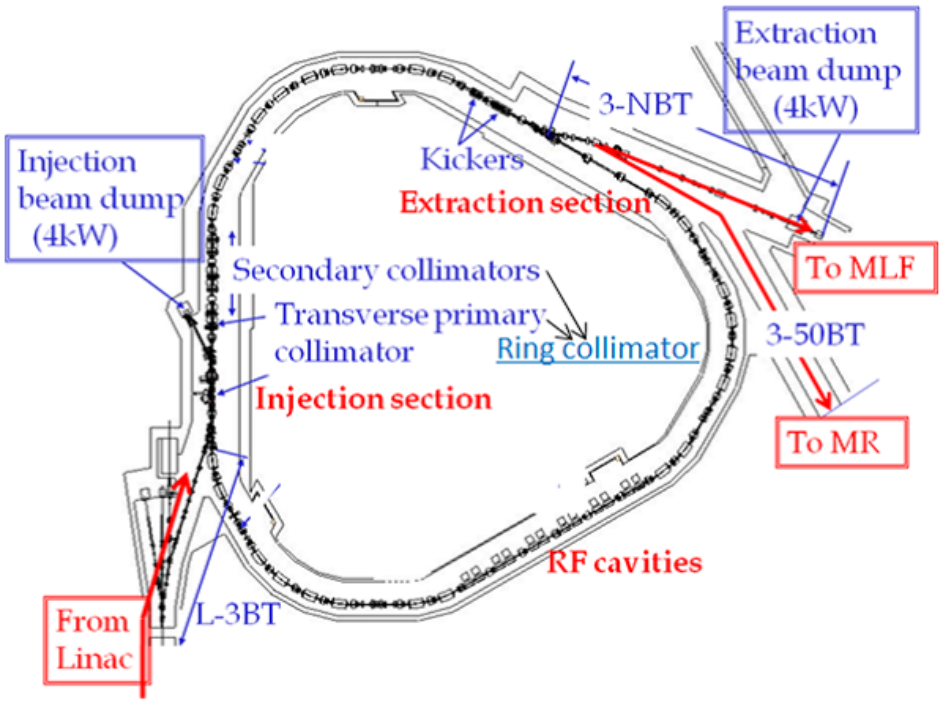

Figure 2: An overview of the RCS.

Table 1: The RCS parameters.

Circumference	348.333 m
Super periodicity	3
Harmonic number	2
No. of bunch	2
Injection energy	400 MeV
Extraction energy	3 GeV
Repetition rate	25 Hz
Particles per pulse	$\sim 8.3 \times 10^{13}$
Output beam power	~ 1 MW
Transition gamma	9.14 GeV
Number of dipoles	24
Number of quadrupoles	60 (7 families)
Number of sextupoles	10 (3 families)
Number of steerings	52
Number of RF cavities	12
Collimator Limit	4 kW

The RCS lattice follows the general FODO type cell. The RCS has a three-fold symmetric lattice and each super-period consists of two 3-DOFO arc modules and one 3-DOFO straight modules. A special feature is that the dispersion of the straight modules is 0. Therefore, the transverse collimator and the injection systems, the extraction systems,

and the RF cavity are not affected by dispersion. On the other hand, in the arc section, the arc module has a missing-bend cell and the horizontal dispersion is a maximum of approximately 5 m. The sextupole magnets for chromatic correction and a longitudinal collimator are installed in this high-dispersion area. In addition, for this lattice, a high transition energy ($\gamma t = 9.2$ GeV), which is sufficiently lower than the extraction energy, is achieved. The RCS beta function and dispersion are shown in Fig. 3.

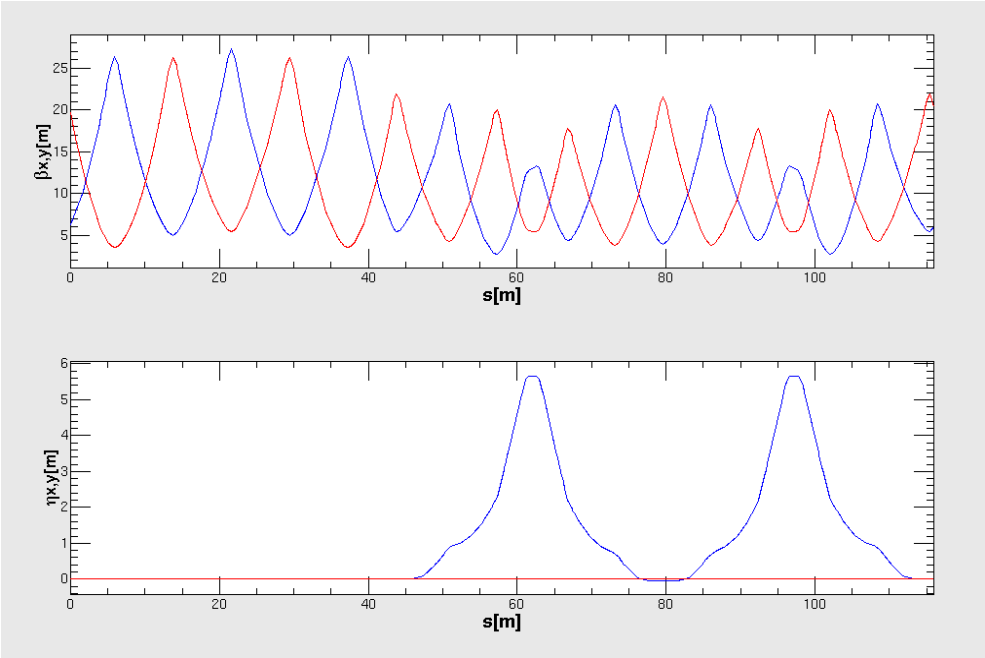

Figure 3: The beta and dispersion functions of the RCS. Only one-third of the circumference of the ring is shown. The upper figure indicates the beta function. The lower figure indicates the dispersion function. The blue and red lines indicate the horizontal and vertical functions, respectively.

To increase the average beam power, the RCS repetition cycle is very fast of 25 Hz. In general, nonmagnetic stainless steel or aluminum is adopted for the vacuum chamber in the accelerator. However, when this type of material is adopted, the chamber will heat up immediately due to the eddy-current effect because of the rapid cycling of the magnetic field in the RCS. To avoid this problem, an alumina-ceramic vacuum chamber is adopted [6]. Electroformed copper stripes are plated outside of the chamber in order to shield the electromagnetic wave from the beam and to pour the image current smoothly to reduce the beam impedance.

The RCS requires a maximum RF voltage of 450 kV per turn in order to accelerate high-intensity beams. This level is too high to achieve using an ordinary ferrite cavity. Therefore, Magnetic Alloy (MA) cavity is adopted as a high gradient RF cavity [7]. Because the saturation field level is high, the permeability and shunt impedance are stable under high RF magnetic conditions. In addition, the RF frequency should sweep from 1.23 to 1.67 MHz, corresponding with 400 MeV to 3 GeV. Because the MA cavity has a wide band of impedance, it is possible to obtain this large RF sweep range.

For the proton accelerator, the beam loss restricts the beam power because the loss causes activation of the instruments. In order to maintain the accelerator continuously, the beam loss should be control at a level that does not affect the human body. The specific value of the allowed beam loss is approximately 1 W/m, which has been proposed on the basis of the experience from the existing accelerators. Even the RCS, it has been inspected that the residual dose around each device is approximately 1 mSv/h less in that condition. However, it is very difficult to achieve this loss rate because the beam which contributes to the loss is of the order of 10^{-4}. Therefore, the transverse collimator (ring collimator) is installed downstream of the injection point [8]. The ring collimator consists of a scatter (primary collimator) and an absorber (secondary collimator). The beam loss is handled by localizing the component of the beam that strays outside of the stable orbit in the ring collimator. In order to localize efficiently, it is important that the large acceptance is kept in another area. Therefore, the duct acceptance of the RCS is 486 π mm mrad for a possible momentum spread of ± 1 % and the primary collimator aperture is set at 324 π mm mrad.

2.3 Multi-turn charge-exchange injection scheme

For the proton synchrotron or storage ring, the multi-turn injection is essential method. In this method, the beam injection is divided into some number of turns and the each injection beam added to the circulating beam repeatedly. This method enables an increase of the circulating beam current without upgrading the injection beam current. In addition, for the formation of the high-intensity beam, H^- ion must be adopted as an injection beam and it must be converted into proton at the injection point. This is known as the charge-exchange injection. The reason why the charge-exchange injection must be adopted is as follows [9].

For the particles having different initial phase-space coordinates of the position and angle with same charge, their coordinates after passing through the magnets are different invariably because the equation of motion which describes passing through the magnets is same. Of course, the initial phase-space coordinates of the injection beam is different from that of the circulating beam. Therefore, if proton is adopted as an injection beam, it is impossible to locate the injection beam onto the phase-space coordinates of the position and angle filled with the circulating beam. Figure 4 shows an example of the multi-turn injection scheme for proton. This injection system consists of the four bump magnet (BM1-4) and the septum magnet (SEPTUM). As shown in top figure of Fig. 4 (a), the local bump orbit is formed by the BMs and the injection beam is led to the ring by the SEPTUM. However, as shown in top figure of Fig. 4 (b), it is impossible to locate the injection beam onto the circulating beam because the circulating bean must avoid the SEPTUM. The injected beam oscillates with large amplitude around the center orbit in the transverse plane. This is called the betatron oscillation. As a result, the circulating beam size increases. Therefore, as shown in bottom figure of Fig. 4 (a), the multi-turn injection must be performed decreasing the bump orbit height in order to prevent the circulating beam collision with the SEPTUM. As a result, the circulating beam size becomes broader as shown in bottom figure of Fig. 4 (b). Hence, the number of injection turn is restricted.

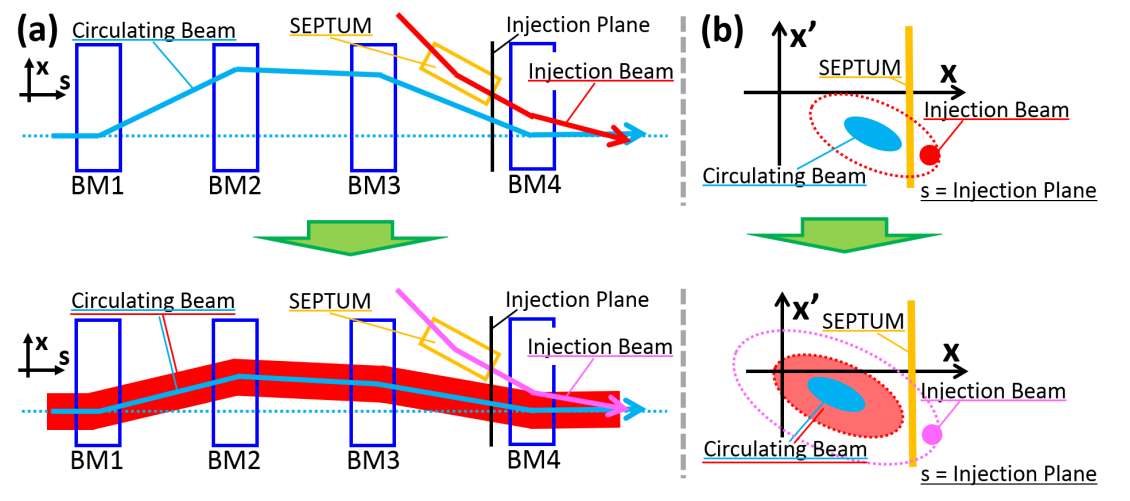

Figure 4: The multi-turn injection scheme using proton. Figure (a) indicates the orbits of the injection and the circulating beam in the horizontal plane. Figure (b) indicates the phase-space of the position and angle at the injection plane. The top and bottom figures indicate the initial and final phase of the injection.

On the other hand, when H^- is adopted as an injection beam, it is possible to locate the injection beam onto the phase-space coordinates of position and angle filled with the circulating beam. The multi-turn charge-exchange injection scheme with H^- in the RCS [10] is described in the following.

Figure 5 shows the H^- multi-turn injection scheme and the arrangement of the injection area. H^- beams from the Linac are transported to the injection point, stripped of electrons, converted into H^+ by the charge-exchange foil, and then injected into the ring. The unstripped beams (H^0 and H^-) are then stripped to become H^+ by the 2^{nd} and 3^{rd} foils downstream of the injection point and led to the H^0 dump. In the case of 181 MeV or 400 MeV injection, the injection is divided into 235 or 307 turns, respectively, during the 500 μs injection period. When the four shift-bump magnets (SB1-4) shape the fixed orbit bump, it becomes possible to locate injection beam onto the circulating beam using H^- as the injection beam, which have the opposite charge to the circulating beam as shown in Fig. 5. Therefore, the circulating beam current can theoretically be increased infinitely without upgrading the injection beam current.

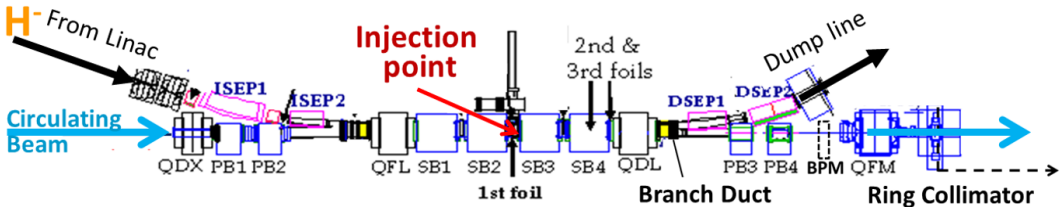

(a) The arrangement of the injection area.

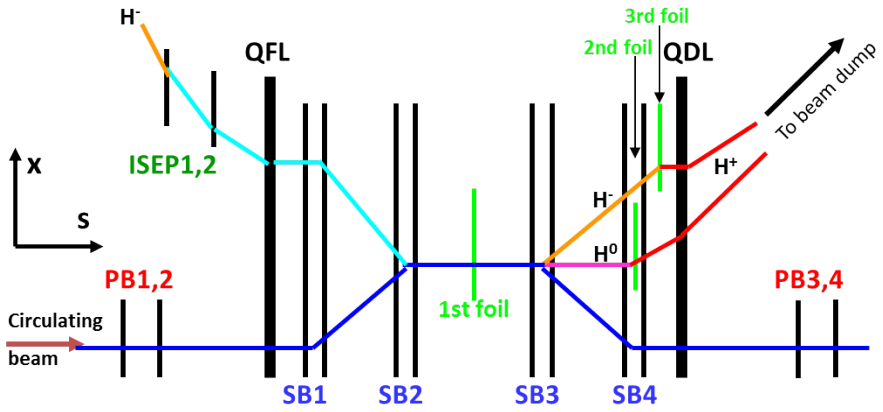

(b) A schematic view of the H^- multi-turn injection.

Figure 5: The H^- multi-turn injection method.

2.4 Transverse painting injection scheme

The multi-turn charge-exchange injection scheme is essential method as described above section. However, when the injection beam is placed on exactly the same position and the same angle as the circulating beam, as shown in Fig. 5, in the high intensity case, the space-charge force cannot be ignored. The space-charge force, i.e., the Coulomb repulsive force due to particle charge, opposes the external convergent force. Therefore, the betatron tune of each particle is decreased from the suitable operating tune point. Furthermore, this decrease is different for each particle. This phenomenon is called incoherent tune (ν_{incoh}) shift and spread. The emittance growth, which can cause beam loss, occurs when the betatron tune approaches the resonance points because of the ν_{incoh} shift and spread. Therefore, we should mitigate the space charge force and suppress the ν_{incoh} shift and spread in order to suppress the beam loss as much as possible. The tune shift due to the space-charge force is called Laslett tune shift. The shift variation is represented by Eq. 1, assuming a long bunch length and uniform transverse distribution:

$$\Delta\nu_{incoh} = -\frac{n_t r_p}{2\pi\beta^2\gamma^3\varepsilon}\frac{1}{B_f} \tag{1}$$

where n_t is the total number of particles, r_p is the classical proton radius, ε is the transverse beam emittance and B_f is the bunching factor corresponding to (average current)/(peak current). This equation indicates that the tune shift particularly occur during the injection period because the β and γ factors become a minimum. This equation also indicates that

the reduction of the ν_{incoh} shift is possible by increasing the value of ϵ. Therefore, it is necessary to form broad beam in the transverse plane.

In addition, in the case of Fig. 5, circulating beams pointlessly hit the foil during injection and beam emittance growth or loss may occur by foil scattering. To suppress the space-charge force and to reduce the number of the charge-exchange foil hits by the circulating beams, the transverse painting injection scheme is adopted in the RCS [10]. The details are as follows.

This scheme is achieved as follows. The horizontal painting injection orbits are shown in Fig. 7a(A). In the horizontal plane, during the 500 μs injection period, four shift-bump magnets shape the fixed orbit bump and four paint-bump magnets (PB1-4) shape the time-decay orbit bump. First, the injection track is matched to this bump orbit. During multi-turn injection, the track of H^- beams is fixed and the central orbit is shifted slightly from the charge-exchange foil by decreasing the time-decay orbit bump height as shown in Fig. 7b(A) and Fig. 7c(A). Therefore, the injection beam changes its position and angles with respect to time in the phase-space of the ring orbit as shown in Fig. 7(B) and the horizontal phase space of the ring is filled with the injection beams. As a result, the stored beam becomes so broader compared with Linac beam in the phase-space. The charge density is formed uniformly and the space-charge force is mitigated. In addition, the number of the charge-exchange foil hits by the circulating beams is decreased because the circulating beam is shifted from the foil.

In the vertical plane, the painting scheme is achieved by two magnets (VPB1, VPB2) installed at the injection line. The vertical painting injection orbits are shown in Fig. 8(A). The injection beam is brought closer to the central orbit from the edge of the painting area or vice versa in the phase-space as shown in Fig. 8(B). Painting from the center to the outside in both horizontal and vertical phase-space is called Correlated Painting. On the other hand, painting from the outside to the center in vertical phase-space different from the Horizontal painting is called Anti-Correlated Painting.

When the injection beam position and angle are painted on the phase-space area in the radial direction in proportion to the square root of the time or turns, the beam is uniformly arranged on the phase-space area because the beam emittance is defined as an area proportional to the square of the radius of the phase-space. Specifically, for an elapsed injection time t, it is described by Eq. 2.

$$\begin{aligned} x\,and\,x' &\propto \sqrt{\frac{t}{500\,\mu s}},\ y' \propto \sqrt{\frac{t}{500\,\mu s}} \quad \text{for Correlated Painting} \\ x\,and\,x' &\propto \sqrt{\frac{t}{500\,\mu s}},\ y' \propto \sqrt{1-\frac{t}{500\,\mu s}} \quad \text{for Anti-Correlated Painting} \end{aligned} \tag{2}$$

In particular, by adopting Anti-Correlated painting, it is possible to bring the beam distribution closer to the uniform distribution, called the "K-V distribution", in which the ν_{incoh} spread theoretically becomes zero [11]. In this distribution, each particle's emittance should satisfy the following relation:

$$\begin{aligned} \gamma_x &= \frac{1+\alpha_x^2}{\beta_x} \\ \varepsilon_x &= \gamma_x x^2 + 2\alpha_x x x' + \beta_x x'^2 \end{aligned}$$

$$\varepsilon_x + \varepsilon_y = const. \tag{3}$$

where α and β are twiss parameters of any point. ε_x and ε_y are the horizontal and vertical emittance of each particle which is invariable, respectively. Figure 6 shows the relation of Eq. 3 and the painting directions in the ε_x-ε_y plane. As shown, the injection beams can be arranged to satisfy the relation given in Eq. 3 in the case of Anti-Correlated painting.

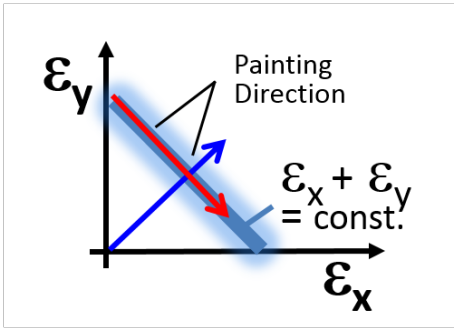

Figure 6: The relation of Eq. 3. The red and blue arrows indicate the directions of Anti-Correlated and Correlated painting, respectively.

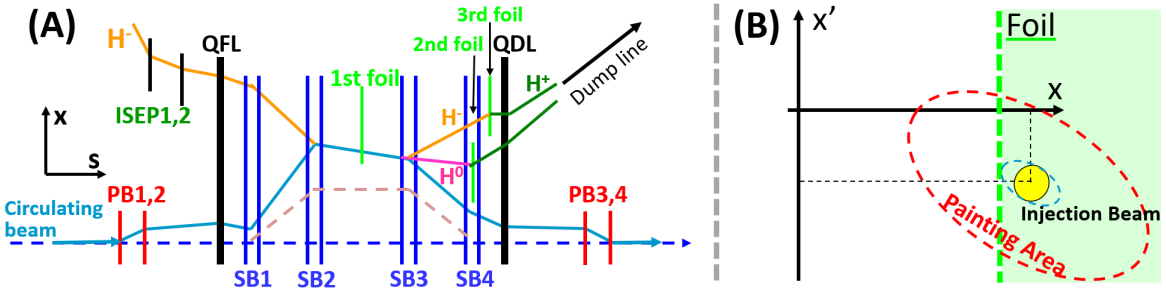

(a) Initial phase of the injection

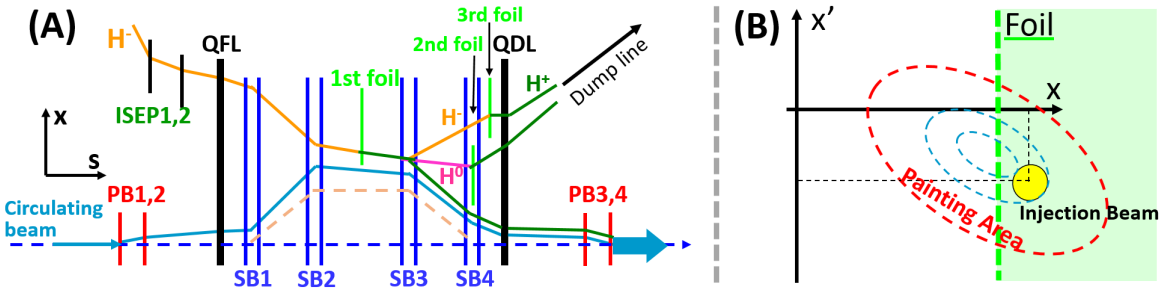

(b) Middle phase of the injection

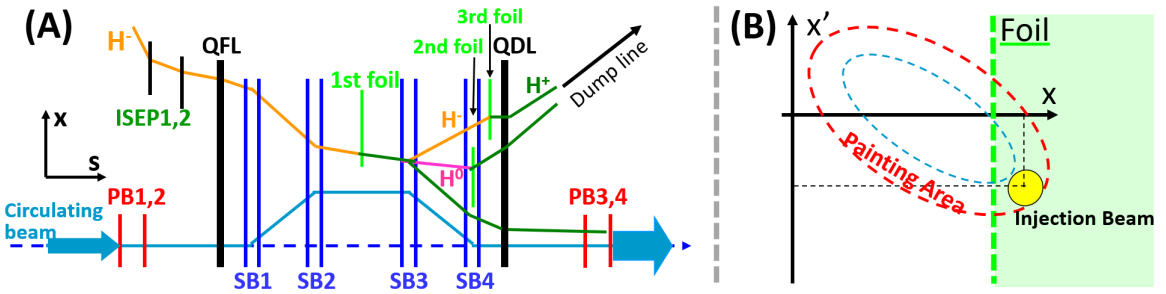

(c) Final phase of the injection

Figure 7: The horizontal variation of the injection and ring orbits during the painting injection period. Figure (A) indicates the orbits of the injection and the circulating beam in the horizontal plane. Figure (B) indicates the phase-space of the position and angle at the injection point.

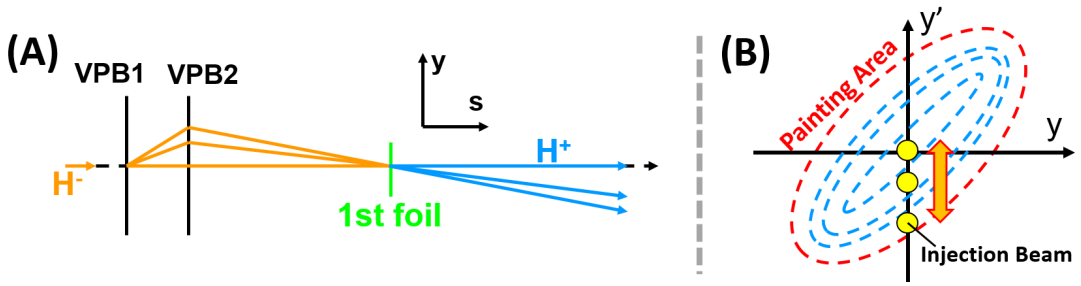

Figure 8: The vertical variation of the injection orbits during the painting injection period. Figure (A) indicates the orbits of the injection in the vertical plane. Figure (B) indicates the phase-space of the position and angle at the injection point.

2.5 Longitudinal painting injection scheme

From the Eq. 1, it is clear that the reduction of the ν_{incoh} shift is also possible by increasing the value of B_f. Therefore, the particles are arranged uniform in the RF bucket during multi-turn injection in the RCS. This scheme is called Longitudinal Painting. Specifically, the two methods are adopted as follows [12] [13]. The schematic drawings of them are shown in Fig. 9.

One method is momentum offset injection. When injected particles are repeatedly arranged at the center of the RF bucket during multi-turn injection, the beam density and the space-charge force become large. Therefore, the beam is injected with a momentum offset as shown in Fig. 9. Thus, a uniform bunch distribution is achieved through emittance dilution by the large synchrotron motion excited by the momentum offset.

Another method is the addition of the second harmonic RF during the multi-turn injection. The second harmonic RF assumes the role of shaping a flatter and wider RF bucket potential, leading to better longitudinal motion, and therefore creating a flatter bunch distribution. In the RCS, the ratio of the second RF voltage to the fundamental RF voltage and the phase difference between two are swept during injection.

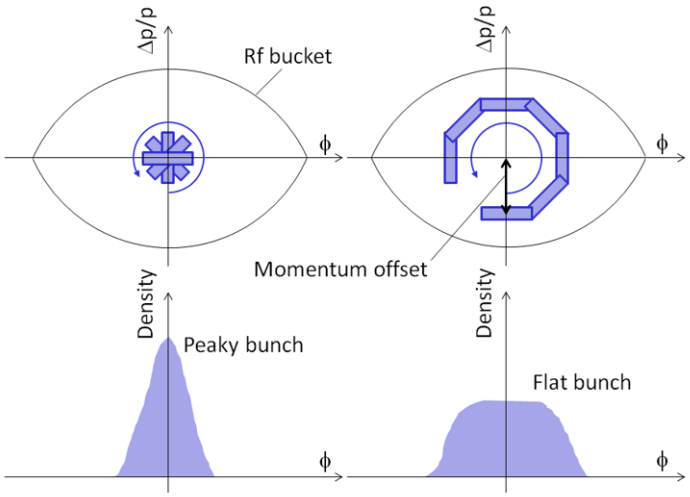

(a) The momentum offset injection scheme. The blue rectangles indicate the injected beam.

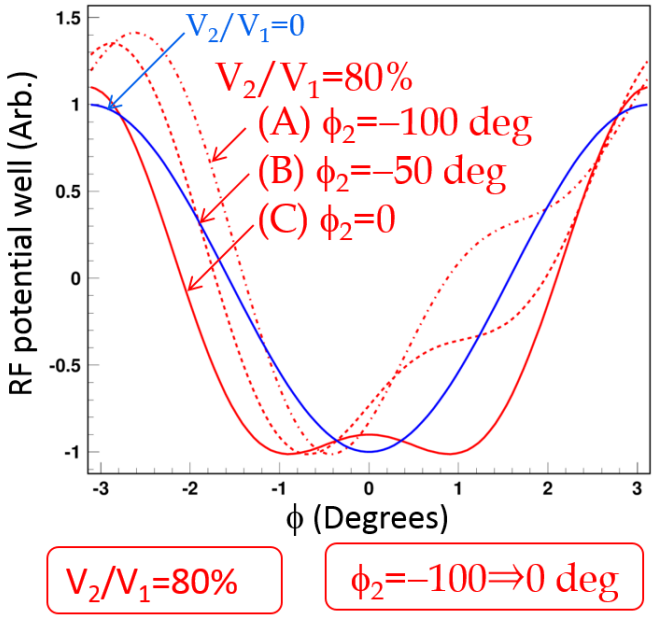

(b) The RF bucket with or without the second harmonic voltage including phase sweep. The V_1 and V_2 indicate the fundamental and second RF voltage, respectively. The ϕ_2 indicates the phase difference.

Figure 9: The longitudinal painting scheme [12] [13].

2.6 Charge-exchange foil in the injection scheme

The charge-exchange foil is a key device for the multi-turn charge-exchange injection. In this section, the property of the foil used in the RCS is described.

The charge-exchange foil is expected to heat up to over 2000 K during injection in 1 MW operation because of the foil hits of the circulating beam. Therefore, development of the foil continues so that its lifetime under high temperatures can be improved. In the RCS, the hybrid boron and carbon foil that consists of 80 % carbon and 20 % boron is adopted [14]. The picture of the foil is shown in Fig. 10.

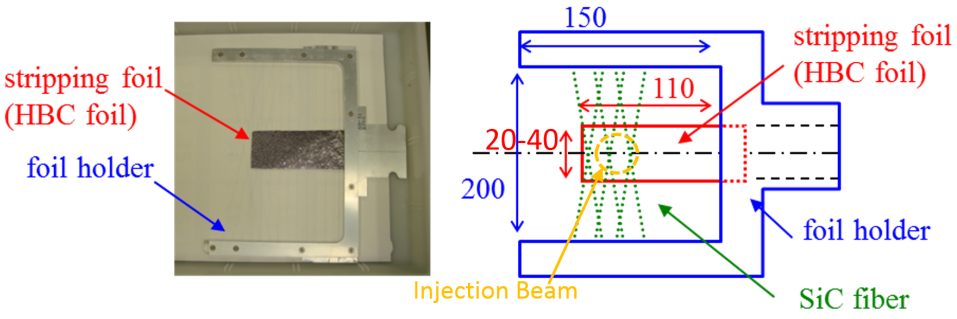

Figure 10: The picture of the foil. The right picture indicates the schematic drawing of the foil and holder.

The thickness of the foil is decided from the requirement of the charge-exchange efficiency. From the point of foil scattering, it seems to be better that the thickness is reduced as much as possible by sacrificing the charge-exchange efficiency. However, this is undesirable because of excited H^0 decay loss. The injection beam becomes H^0 which is in an excited state n ($H^0(n)$) when only one electron is stripped from H^-. In the RCS, this $H^0(n)$ causes uncontrollable beam loss when the $H^0(n)$ is broken down into H^+ by the peripheral magnetic field before reaching the 2^{nd} foil.

The $H^0(n)$ lifetime of each state in the magnetic field is shown in Fig. 11 [15]. The orange dashed line indicates the time of flight from 1^{st} to 2^{nd} foil. The pink dashed line indicates the maximum SB field. Therefore, the states which are inside of yellow square area could cause the excited H^0 decay loss. Specifically, H^0 which is in a excited state ≥ 6 causes uncontrollable beam loss. The total yield of excited state with $n \geq 6$ is estimated by assuming that the yield of the excited state is proportional to n^{-3} as follow in Eq. 4 [16] [17].

$$\text{Total yield}(n \geq 6) = (\text{ratio of } H^0) \times \sum_{n=6}^{\infty} \frac{1}{n^3} / \sum_{n=1}^{\infty} \frac{1}{n^3} \tag{4}$$

The charge-exchange efficiency of the carbon foil is shown in Fig. 12 [18]. In the RCS, in the previous 181 MeV injection case, the foil thickness of 200 $\mu g/cm^2$ was selected in order to achieve a charge-exchange efficiency over 99.6 % and the H^0 decay loss was estimated to be 1.4 W at 300 kW operation. In the case of 400 MeV injection, a foil thickness of 300 $\mu g/cm^2$ was selected in order to achieve the same efficiency and the loss in this case was estimated to be 7.3 W at 1 MW operation.

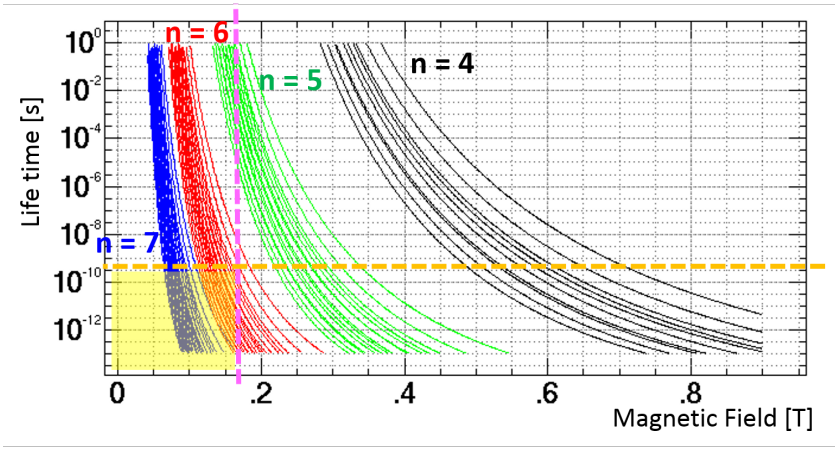

Figure 11: The H^0(n) lifetime of each state in the magnetic field for 400 MeV [15]. The orange dashed line indicates the time of flight from 1^{st} to 2^{nd} foil. The pink dashed line indicates the maximum SB field. The states which are inside of yellow square area could cause the excited H^0 decay loss.

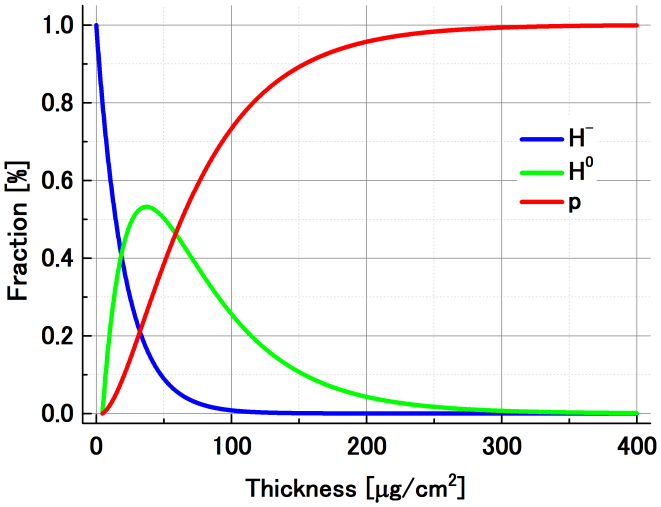

Figure 12: The charge-exchange efficiency of the carbon foil for H^- in the case of 400 MeV [18].

3 The large-angle foil-scattering beam loss and the countermeasure

As introduced in section 2, the multi-turn charge-exchange injection scheme is required for the the high-intensity proton synchrotron or storage ring. However, the circulating beam repeatedly collides with the foil and it is scattered during the injection period unfortunately. In particular, the particles scattered at large angles are lost directly without circulating and then they cause activation at downstream of the injection area. This is the large-angle foil scattering beam loss. In this section, it is described that the large-angle foil scattering beam loss could become an issue for the high-intensity proton synchrotron or storage ring using the survey results of the RCS and the simulation results. And then, the countermeasure against the loss is described.

3.1 Beam loss issue around the injection downstream area

In the RCS, unexpected losses were observed during 181 MeV injection between the H^0 branch duct and the horizontally focusing quadrupole magnet (QFM) located downstream of the injection point. The residual dose distribution is shown in Fig. 13. As shown in right figure of Fig. 13, the residual dose was under 100 μSv/h on contact expect the end of the ring collimator after a 4 hours cooling period following a 200 kW cycle operation. In other words, the beam losses were localized at the ring collimator successfully. However, in the injection area, the residual doses were 4.5 mSv/h at the branching of the H^0 dump line and 6.2 mSv/h at the inside of the beam position monitor (BPM). These losses were not small considering the exposure to radiation during maintenance. Therefore, this beam loss limited the progress of increasing the beam intensity. From the results of some experiments and simulations, it became clear that these significant losses were caused by the large-angle foil scattering of the injection and circulating beams [19] [20]. Because the number of foil hits increases with increasing beam intensity, this problem had to be solved.

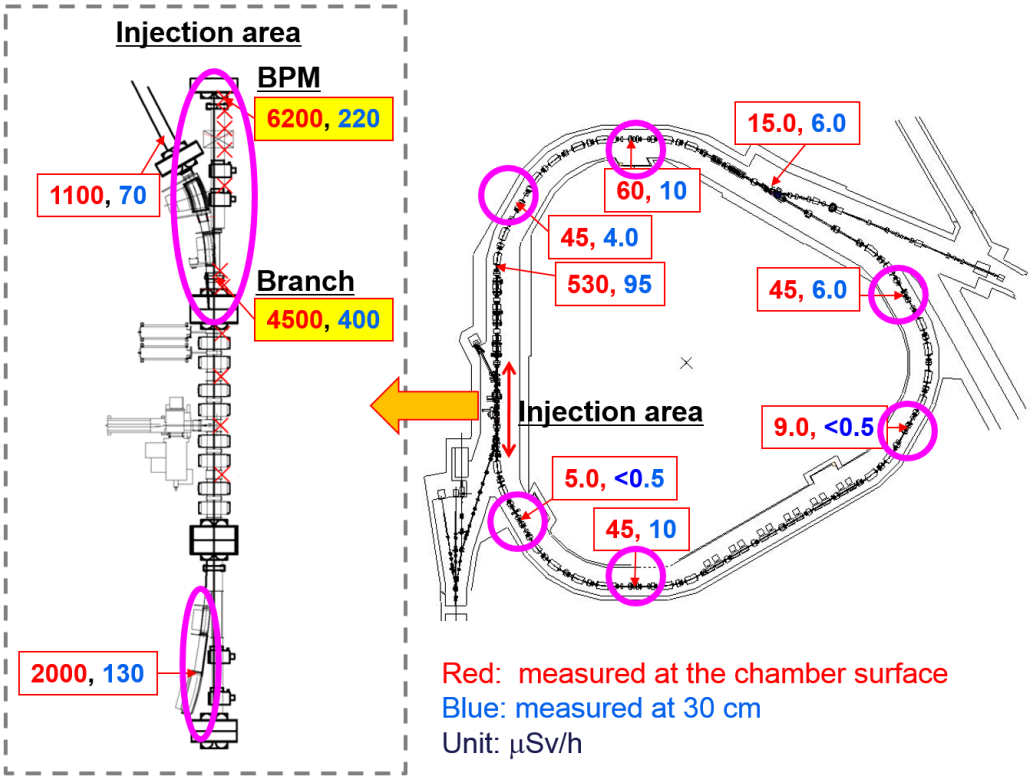

Figure 13: The residual dose distribution after 4 hours cooling down period following one 200 kW cycle operation in 2011.

3.2 Tracking simulation of the foil scattered particle

By the tracking simulation, it was confirmed that the scattered particles by the foil was lost at downstream of the injection area. This simulation was performed using the SAD [21]. SAD is a computer program that has been developed in KEK since 1986 for accelerator design, simulation, commissioning and improvement. The lattice structures are defined by the arrangement of the components such as the drift space and the magnet. SAD has rich matching functions. For example, the optics such as the betatron tune and the geometry such as the duct size can be matched simultaneously. In addition, the matching can be performed not only for the central orbit but also for the particle which has off-momentum or finite-amplitude. The particle tracking is performed by the 6D full-symplectic transformation [22].

In the RCS, the the nonlinear field cannot be ignored because the magnet aperture is large. Therefore, the field which expanded to multi-pole components is incorporated into the accelerator model based on the field measurement result. For example, the SB magnet has the large aperture because the both injection and the circulating beam pass through. The interference of the field also occurs because the SB magnets are closely installed between quadrupole magnets which are QFL and QDL shown in Fig. 5. In addition, the circulating beam is shifted largely in the horizontal plane during the injection period. Consequently, the nonlinear fields may affect the circulating beam. To consider the nonlinear field and the interference, the SB magnets are divided into the pieces having

20 mm longitudinal effective length and the fields which expanded to decapole components are incorporated into the model [10].

The tracking simulation results for the scattered particles between the injection point and the ring collimator are shown in Fig. 14. The particles were given arbitrary angles at the injection point and tracked. The maximum angle was ±25 mrad and the pitch was 0.5 mrad. In the vertical plane, as shown in Fig. 14, the large-scattered particles whose angles are several milliradians pass through the ring collimator. On the other hand, in the horizontal plane, the large-angle scattered particles are lost at the H^0 branch and the BPM, which has a small aperture because the scattered particles are subjected to the influence of the QDL, which is a horizontally defocusing quadrupole magnet that increases the horizontal angle. The acceptances of each component from the injection point are shown in Fig. 15. Thus, it became clear that the minimum horizontal scattering angle at which particles might be lost was approximately ±3 mrad, while the minimum vertical scattering angle at which particles might be lost was approximately ±10 mrad. In other words, the source of the losses was mostly horizontally large-scattered particles.

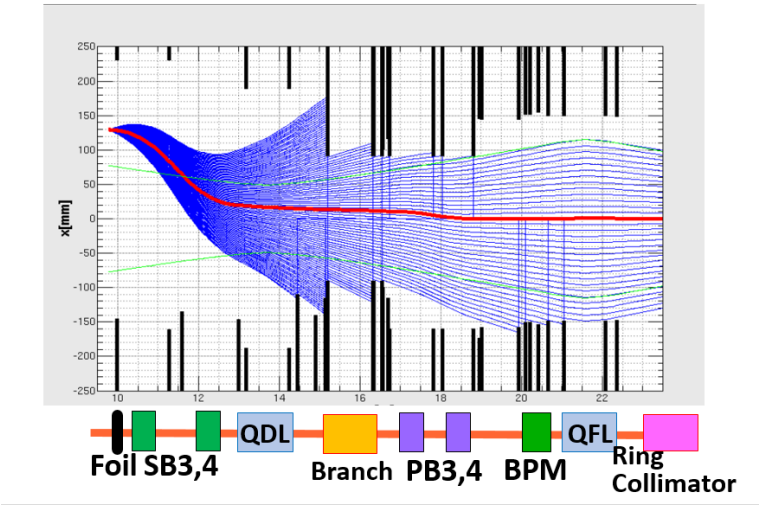

(a) Horizontal plane

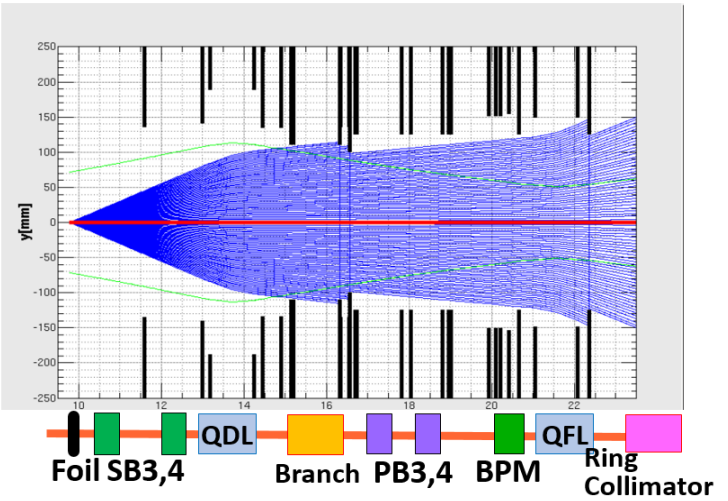

(b) Vertial plane

Figure 14: The tracking simulation of the horizontally and vertically scattered beam at the start of the injection period. The blue lines are the tracks of particles that had arbitrary angles at the injection point. The green lines indicate the 486 π mm mrad beam envelope. The red line indicates the closed orbit.

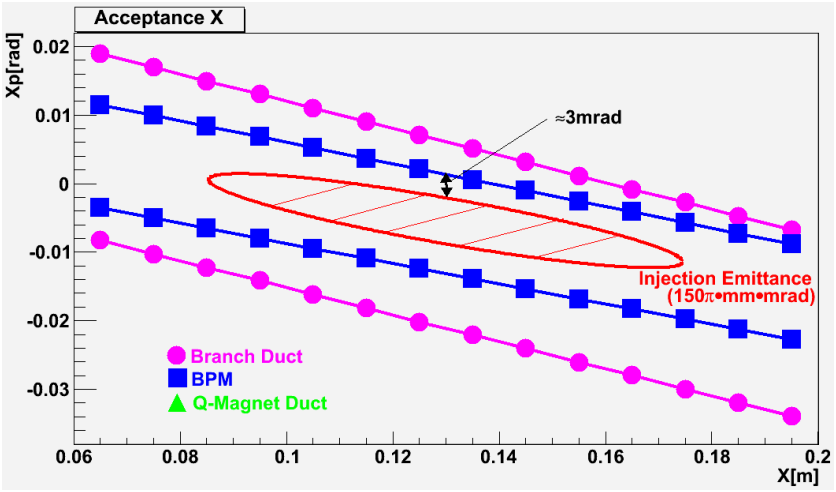

(a) Horizontal plane

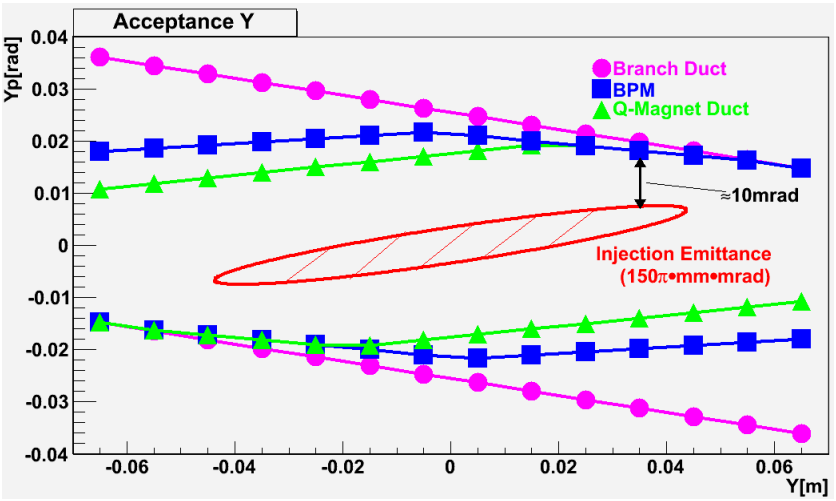

(b) Vertial plane

Figure 15: The acceptance of each component from the injection point. For each component, the particles whose phase-space coordinates at the foil are the interior of the two lines are acceptable.

3.3 Estimation of the event rate of the large-angle foil-scattering

To obtain the angle distribution of the large-scattered proton due to the foil and to estimate the probability of the large angle scattering occurrence, GEANT4 [23] simulation was performed. GEANT4 is a toolkit for the simulation of the passage of particles through matter. In other words, it is function libraries based on the C^{++} language. The interaction, such as a particle production and a scattering, between the particle and the materials is calculated using the Monte Carlo Method. By defining the 3D geometry such as the detector in the simulation space, the user can reproduce the real construction of the equipment. The user also should define the characteristics of the particle source such as a particle type, position and energy distribution. In the simulation., the particles are

tracked by one shot and the interactions are calculated for each step length determined by GEANT4.

The large angle scattering due to the foil is mainly caused by the multiple Coulomb scattering. In the GEANT4, multiple scattering (MSC) approach is used instead of calculating all collisions in order to have acceptable CPU performance of the simulation [24]. For considering MSC process, the condensed simulation algorithms, in which the global effects of the collisions are simulated at the end of a track segment, is used. In the GEANT4, the Urban MSC model, which is based on the the multiple scattering theory of Lewis [25], is used. The details of this model are described at Ref. [24].

The simulation results of scattering angle due to the foil using GEANT4 are shown in Fig. 16. The number of events in the simulations was increased to 10^9; therefore, approximately 10^4 events that had a scattering angle exceeding ± 3 mrad were obtained for the first time. Because these events were caused by the multiple Coulomb scattering, the energy loss hardly results. The probability of the occurrence of such large-angle scattering cases looks like very low, which is approximately 10^{-5}. However, the total losses between the 1^{st} foil and the ring collimator become conspicuous due to repeated collisions of the circulating beam with the foil during the multi-turn injection. In the RCS, the number of foil hit par particle is 117 when all beams hit the foil repeatedly during the multi-turn injection with 235 turns. Because the injected beam is 12 kW in the 181 MeV injection case for 200 kW operation shown in Fig. 13, the total losses between the 1^{st} foil and the ring collimator are estimated to be, at most, 14 W. In addition, the distance between the 1^{st} foil and the ring collimator is approximately 10 m and the residual dose is expected to be 1 mSv/h when the loss is 1 W/m. Thus, the large-angle foil scattering beam loss become conspicuous as shown in Fig. 13.

In addition, when the injection energy is 400 MeV, the number of events with a scattering angle of over ± 3 mrad will decrease to only 80 % of the 181 MeV injection case. Therefore, the total losses are expected to increase by a factor of 9 during 1 MW operations because of the increases in kinetic energy and peak current compared with the 181 MeV injection and 200 kW operations. Thus, the large-angle foil scattering beam loss must be solved.

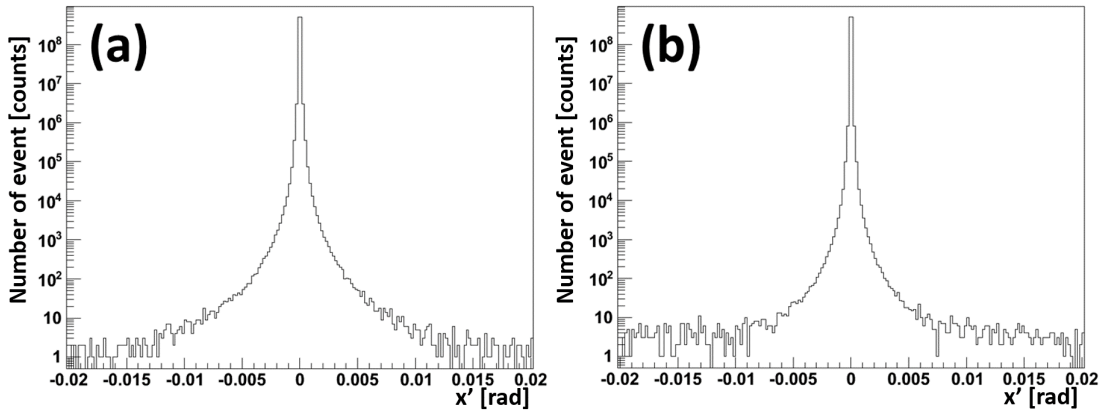

Figure 16: The proton scattering distribution by the charge-exchange foil at (a) 181 MeV with 200 μg/cm^2 foil thickness, and (b) 400 MeV with 300 μg/cm^2 foil thickness.

3.4 Countermeasure of the large-angle foil-scattering beam loss

The countermeasure of the large-angle foil scattering beam loss is required. However, in principle, complete prevention of foil scattering is impossible. Therefore, as a countermeasure against the loss, it was decided that an additional collimation system was developed to locally collect the large-angle-scattered particles and restrict the activated area [19]. Because the source of the loss is the nearly horizontally scattered particles, the absorber of the collimation system was designed to limit the horizontal aperture and directly remove these particles. With respect to the installation point, just upstream of the loss points is a suitable localization point because the particles are more separated from the core beam in the downstream area as seen in Fig. 15. Specifically, installing the absorber just before the BPM is desirable. However, the loss at the H^0 branch cannot be localized further upstream because the upstream magnet arrangement is too tight. In addition, it is desirable that losses between the H^0 branch and the ring collimator are localized in one place in order to confine the high activation area. Therefore, a new H^0 branch duct was developed as a new collimation system including absorbers. It is called the Large Scattered Beam Collimation System (LSB-Collimator). A schematic of the collimation system and the removal effect is shown in Fig. 17.

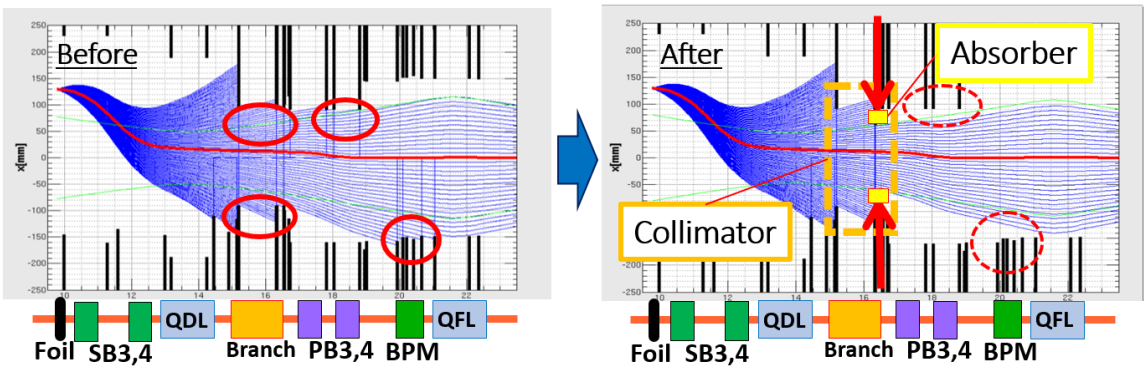

Figure 17: A schematic view of the collimation system and the removal effect. The left and right figures indicate the horizontally tracking simulation with and without the absorber.

3.5 LSB-Collimator

The construction of the LSB-Collimator is shown in Fig. 18. This system consists of three elements: the H^0 branch duct, a radiation shield and two absorbers. The H^0 branch consists of a curved duct connected to the H^0 dump line and a linear duct connected to the ring. The linear duct is fabricated from SUS430, which is a magnetic steer, to shield the leakage field from the dump septum magnet (DSEP1) [26]. The radiation shield covers the H^0 branch duct and DSEP1 in order to confine the loss of the H^0 branch and enable maintenance in this area. Two absorbers were added at the downstream end of the linear duct to remove the particles that would otherwise have been lost between the absorbers and ring collimator. The shield width is 450 mm, which was selected on the basis of simulation results using the MARS [27] particle reaction simulation code. The simulation indicated that the residual dose on the shield surface would be less than 1 mSv/hr after

one operation cycle if the amount of the beam loss at the absorber was 100 W [19]. The entire system, including the DSEP1, is installed on a linear motion guide and can thus be readily removed if it needs to be replaced. The picture of the system is shown in Fig. 19. Removal can be completed in approximately 40 min and the risk of the exposure can be suppressed.

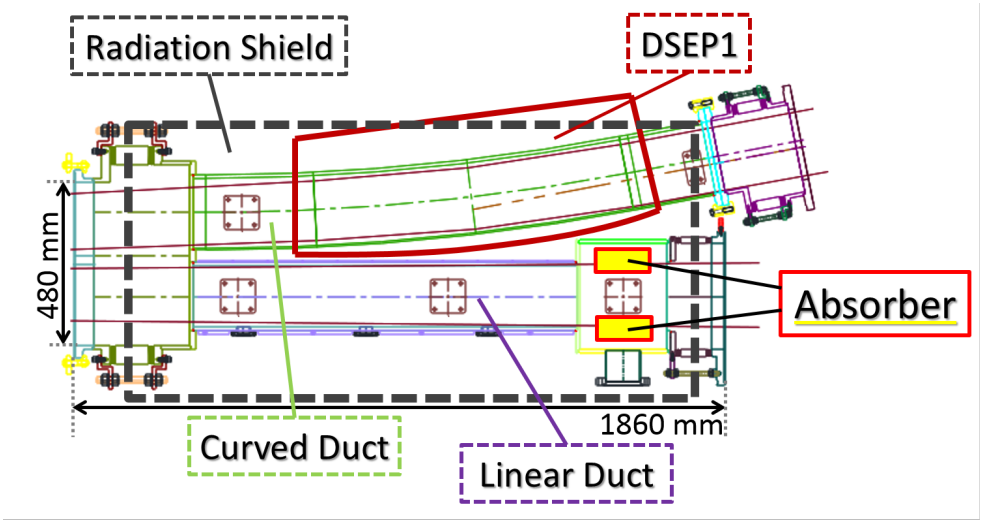

Figure 18: Construction of the LSB-Collimator.

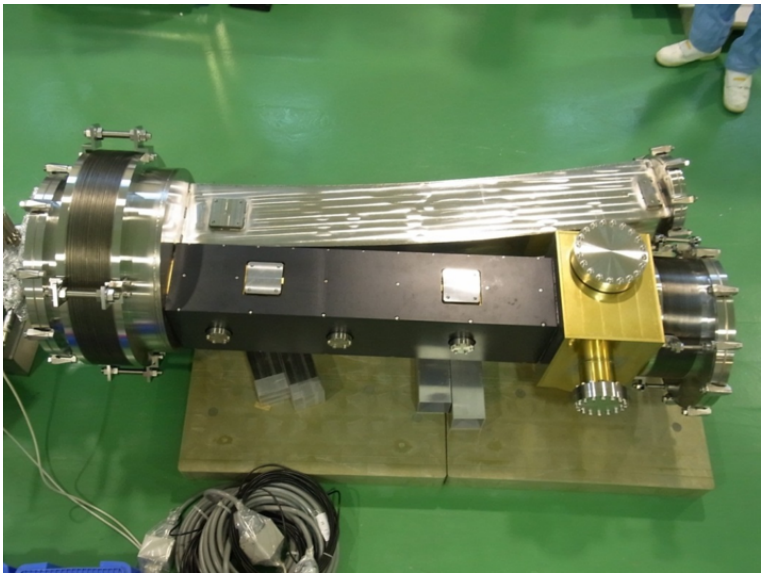

(a) A picture of the new H^0 branch duct

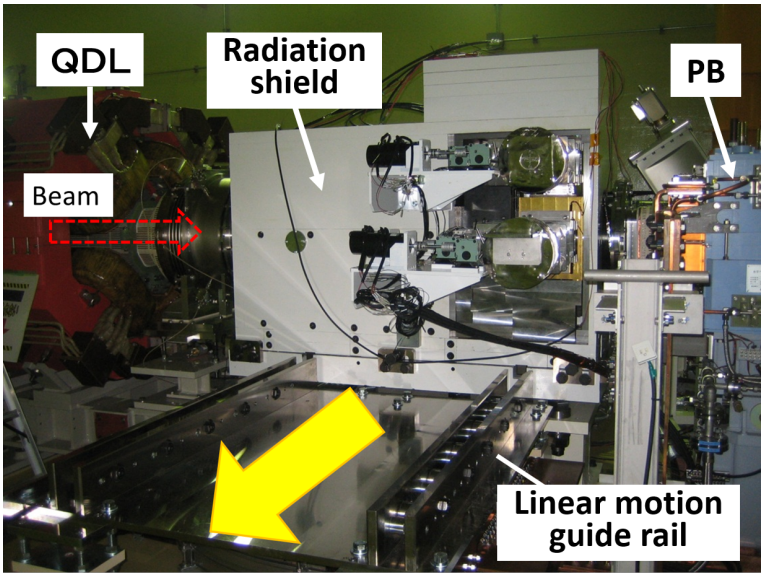

(b) A picture of the whole LSB-Collimator

Figure 19: The pictures of the LSB-Collimator.

3.6 Design of the collimator absorber

The absorbers must also meet certain requirements. First, they must have a low outgassing rate and enhanced thermal conduction for cooling. Particularly, it is desired to have an air cooling system because the coolant could be activated. Therefore, oxygen-free copper, which was used as the ring collimator in the RCS [8], was selected. In addition, this is cooled naturally in air, because it was confirmed by finite element method calculations that the increase in the absorber temperature would be 80 degrees at most if the beam loss at the absorber was 100 W [19].

Second, the absorbers must be located on the right and left sides in the horizontal plane and must also have sufficient longitudinal length. Because the range of a 400 MeV proton in oxygen-free copper is calculated to be approximately 130 mm using the Bethe-Bloch equation, the necessary absorber length was determined to be 200 mm, including a reasonable margin.

Third, it was assumed that the beam side of the absorbers must have a particular angle. A schematic drawing is shown in Fig. 20. If the absorber is a rectangular parallelepiped, the horizontally spread scattered particles collide with the side of the absorber. In this case, the sufficient flight distance in the absorber is not maintained, and the particles cannot be absorbed well. Therefore, the absorbers were designed with an angle such that the scattered particles would collide with the front of the absorber. As a result of an investigation [28], the angles of the inside and outside absorbers were decided to be 18.5 mrad and 8.5 mrad respectively.

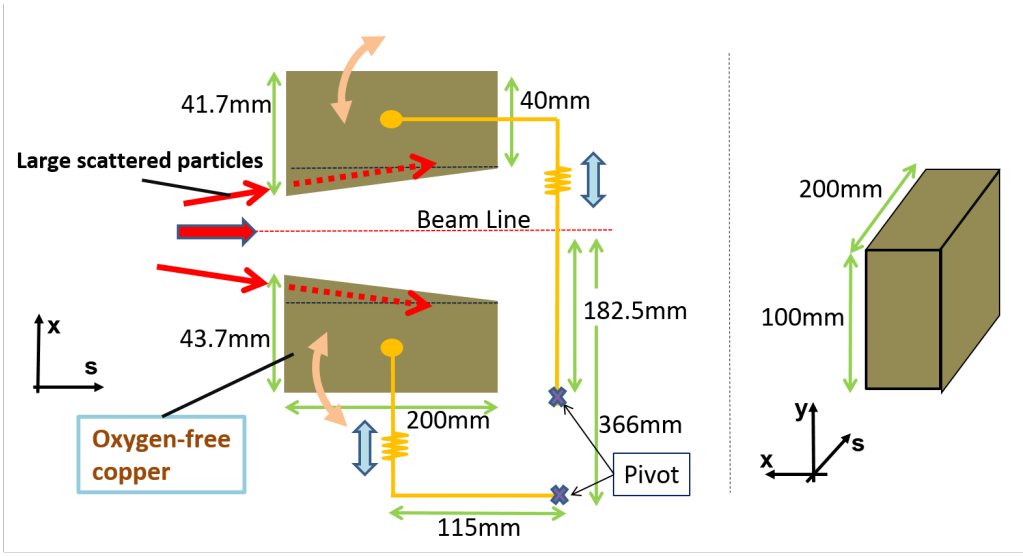

Figure 20: A schematic drawing of the absorber.

Finally, the position and angle of the absorbers were required to be adjustable because the beam width and scattered particle angle at the absorber changed if the operational parameters changed. Therefore, the absorbers support rods were designed to be adjustable through expansion and contraction. In addition, the absorbers were also designed to be rotatable around pivots located at the downstream end of the absorbers. A schematic drawing of the absorber chamber and a picture of the inside of the absorber chamber are shown in Fig. 21.

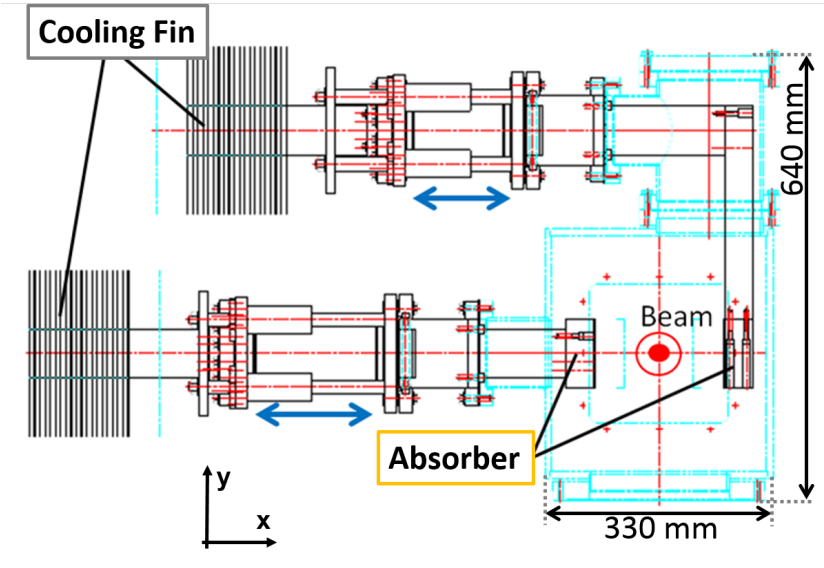

(a) A schematic drawing of the absorber

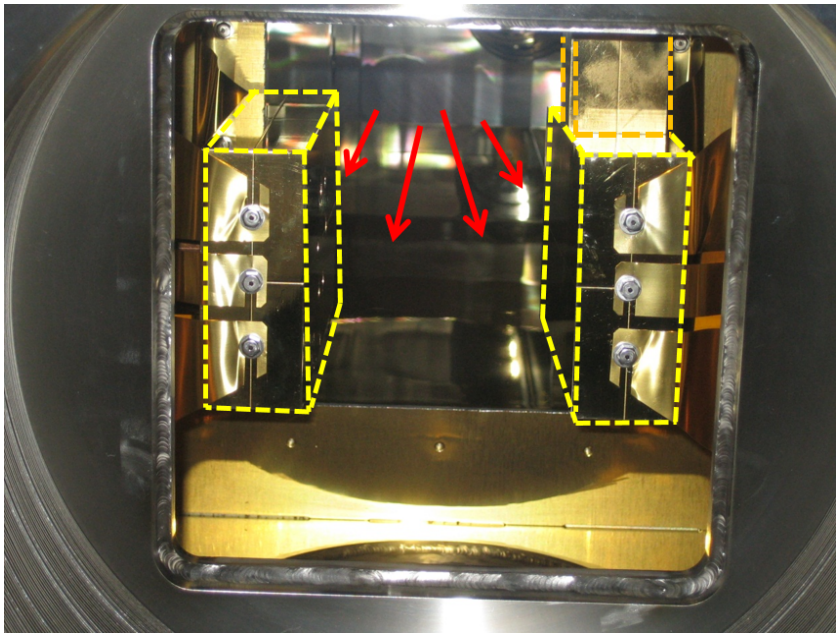

(b) A picture of the inside of the absorber chamber. This was taken at the end of the H^0 branch duct.

Figure 21: A schematic view and picture of the absorber chamber.

4 Optimization method of absorbers for sufficient localization

As described in section 3, the position of the absorber included the LSB-Collimator can be adjusted. The absorber has surface angle and can be rotated such that the scattered particles will collide with the front of it. Therefore, in this section, the optimization method is described. In particular, the original beam-based angle optimization method is described. First, the simulation model constructed for the investigation of the angle optimization method is described. This model is also used for the discussion of the experimental results in section 6. Next, the position optimization method is described. Finally, the importance of the angle optimization and the its method are described.

4.1 Simulation model of the Large Scattered Beam Collimation System

To examine the optimization method of the absorber and the localization effect, a realistic simulation model was constructed. This model was also useful for better comprehending the absorber states during experimental optimization and estimating the amount of during high-intensity operations.

In the RCS, beam commissioning has been successfully performed using SAD in which the RCS lattice is constructed in detail including error sources, for example, alignment errors, individual differences of the magnets, and the leakage field of the extraction kicker. On the other hand, the beam loss, extraction beam emittance, and others, have been demonstrated well with the SIMPSONS [29] [30] simulation (see 4.1.1) that considered the space-charge force. Therefore, these simulation codes are suitable for constructing the simulation set.

In the particle simulation, one of the issues is how to get the large number of events. In particular, the large-angle scattered particles that should be eliminated by the absorbers occur with a very low probability, approximately 10^{-5}. Given this fact, some effective simplifications were applied to obtain sufficient statistics.

This simulation model was constructed by dividing it into 4-sections and codes as follows. A schematic drawing of the model is shown in Fig. 22. The first section is the determination of the simulation particle source. This multi-particle simulation is performed during the injection period using SIMPSONS. The distributions of the beams at the foil are stored for each turn. In this SIMPSONS simulation, the space-charge force was considered. In addition, foil scattering was also considered, although the scattering angles were obtained using the 10^6 events of GEANT4 simulation and large-angle scattering was neglected. Next, scattering angles greater than ± 3 mrad, which were obtained from the 10^{10} events of the GEANT4 simulation, were added to that stored distribution. This distribution was considered to be the simulation source. In other words, one simplification is that the circulating beams that were not related to the losses between the foil and ring collimator were omitted, and another is that the decrease in the number of particles caused by large-angle scattering was neglected.

The second section of the model is particle tracking. Particles are tracked to ring collimator using SAD. In other words, the simulation area was restricted to the ring

collimator, which collects the particles at a distance from the stable region.

The third section is the simulation of the particle collision with the absorbers. The absorber structure and adjustment mechanism were constructed in detail using GEANT4. When the interaction between particles and materials should be considered, this GEANT4 simulation replaced the absorber part of the second section.

The fourth section is the calculation of the radio-activation level. The BPM chamber, where beams were particularly lost, was modeled using the PHITS code [31] and the residual dose was evaluated using tracked particles. PHITS is the Monte Carlo simulation code which can calculate the behavior of the radiations in the space or materials. User defines the 3D geometry and initial particle property like GEANT4. The difference between the two is that PHITS can evaluate the residual dose caused by the created radionuclide. For example, PHITS can simulate the accelerator operation cycle including the cooling period. And then, the temporal transition of the residual dose can be evaluated.

Using these simplifications and divisions, the time needed for calculation was drastically reduced. Specifically, the required results could be obtained within a few days.

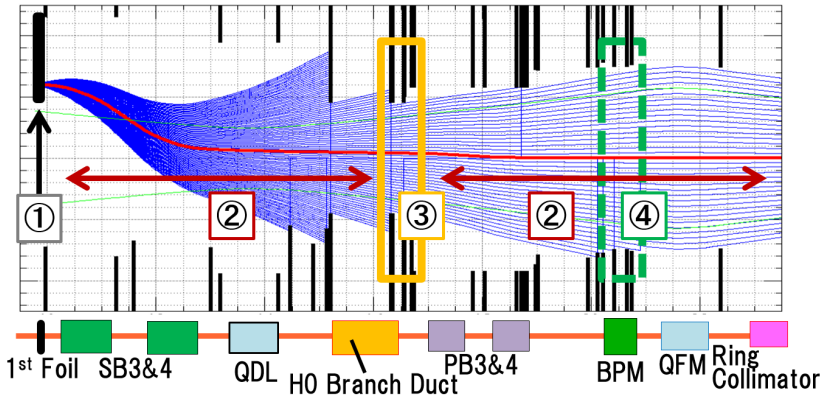

Figure 22: A schematic drawing of the simulation model. The number 1 in the figure indicates the section of determination of the initial distribution by SIMPSONS and GEANT4. The number 2 indicates the tracking section using SAD. The number 3 indicates the GEANT4 section for particle interactions with the absorber. The number 4 indicates the estimation section of the residual dose by PHITS.

4.1.1 SIMPSONS simulation

SIMPSONS is a beam tracking simulation code for the storage ring and the synchrotron [29]. The 6-dimensional phase-space distributions of the beam are calculated by the multi-particle simulation. This code also can simulate a space charge force. The code was developed by Dr. S. Machida of Rutherford Appleton Laboratory. In order to suit the code to the RCS, the code has been improved by the RCS commissioning members including the author.

The details of the simulation are explained as follows. First, the magnets and the drift spaces are arranged in the simulation. The thin lens approximation which ignore the magnet thickness of the s direction applies to the magnets. The simulation particles are

tracked each time step of Δt to the $+s$ direction. Figure 23 shows the injection scheme in the SIMPSONS. Before start of the simulation, the injection beam, which is the Linac beam in the RCS, is prepared. After start of the simulation, this beam is moved to the $+s$ direction with the time step of Δt. And then, the particles which pass through the injection point are tracked in the ring. When the particles pass through the magnet components, the kick angles are added to the particles. The details are explained in Appendix A.

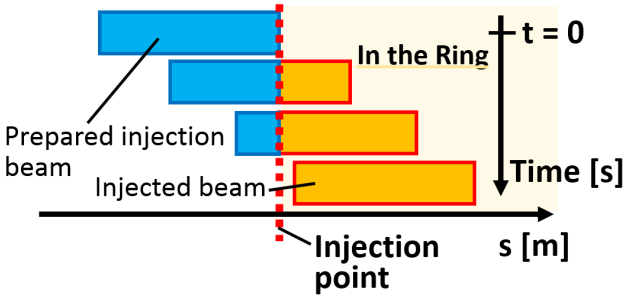

Figure 23: The injection scheme in the SIMPSONS.

In this way, the SIMPSONS is a time dependent simulation code. Therefore, it is easy to input the time variable components. For example, the magnetic field, the acceleration electric field (rf voltage), and the error components such as a ripple due to the power supply. In addition, the self-consistent calculation of the space charge force can be performed. The calculation method is explained in the following.

In the multi-particle simulation, each particle is called macro-particle because a large number of particles located closely are represented by this particle for the reduction of the number of the simulated particle. In the calculation of the space charge force, if Coulomb interactions are calculated for all macro-particle, the calculation time become too large. Therefore, the Particle-In-Cell method (PIC) is used in the SIMPSONS [32].

For the PIC, the source of the space charge force is considered as the mean field made from the charge distribution of the beam. The calculation of the space charge force using PIC is performed as follow processes.

1. The mesh dividing the 3D space uniformly is prepared.
2. The each charge of the macro-particle is allocated to the near grid points which are the cross point of the mesh.
3. The potential and the electric field are calculated at each grid point.
4. The electric fields at each grid point are allocated to the near macro-particles.

In this method, the potential is calculated only once and the number of grid point is smaller than that of macro-particle. Therefore, the calculation time can be shortened. In the SIMPSONS, this four processes are performed repeatedly with the time step of Δt.

In the process of the 2 and 4, Area Weighting Method is usually adopted. This method for the 2D rectangular coordinate system is explained using Fig. 24 as follows. First, the

mesh is divided to be four area by the two lines which cross at the coordinates of the macro-particle. Next, the charge of the macro-particle is allocated to the four grids. The partition ratio of the each grids is considered the percentage of the opposite area size. Specifically, it is shown in Eq. 5. For the 3D, the cubic mesh is divided to eight volume.

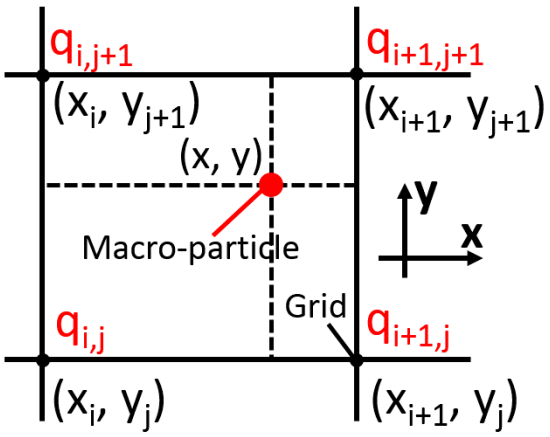

Figure 24: The mesh for the 2D rectangular coordinate system.

$$
\begin{aligned}
q_{i,j} &= \frac{(x_{i+1}-x)(y_{j+1}-y)}{(x_{i+1}-x_i)(y_{j+1}-y_j)} \\
q_{i+1,j} &= \frac{(x-x_i)(y_{j+1}-y)}{(x_{i+1}-x_i)(y_{j+1}-y_j)} \\
q_{i,j+1} &= \frac{(x_{i+1}-x)(y-y_j)}{(x_{i+1}-x_i)(y_{j+1}-y_j)} \\
q_{i+1,j+1} &= \frac{(x-x_i)(y-y_j)}{(x_{i+1}-x_i)(y_{j+1}-y_j)}
\end{aligned}
\tag{5}
$$

In the process of the 1 and 3, the cylindrical coordinates seems to be natural because the distribution of the beam and the shape of the beam pipe which is a boundary condition are cylindrical. In the SIMPSONS, the Poisson equation is solved by the Fourier transform in the cylindrical coordinates. The potential is expanded with the harmonic components of the azimuthal direction. The details are explained in Appendix B. In addition, the results of the comparison between the experimental results and the SIMPSONS simulation is explained in Appendix C.

4.2 Optimization method of absorber position

By inserting absorbers to the beam center, downstream losses can be removed. In the experimental optimization, the absorber position at which the loss is completely removed should be selected. However, there are two notable points. One relates to excessive insertion of absorbers, another to the variation of the required insertion distance during the injection period.

The first point can be explained as follows. In the RCS, a large aperture of 486 π mm mrad is kept all around the ring without ring collimator in order to prevent the radio-activation. However, the absorber position may become lower than this aperture depending on the operation conditions. In this case, the absorber could play a role similar to the primary collimator and distribute the beam halo over the downstream area. In other words, the absorber could become the new loss source. Thus, absorber optimization should be performed alongside monitoring of the loss in the downstream area. And then, the absorber position that does not create additional losses should be selected, even the loss cannot be completely removed.

The second point can be explained as follows. For painting injection, the required insertion distance changes between the start and end of injection period. The tracking simulation results for the loss at the inside of the BPM are shown in Fig. 25. The particles, which are given arbitrary angles at the injection point, are tracked. The calculated absorber positions that are required for removing downstream loss are shown in Fig. 26. Because the inward kick angle of the PB3 gradually decreases (ref. 2.3.1), the inside absorber requires a large insertion distance at the start of the injection period. On the other hand, the outside absorber is required at the end of the injection period. Therefore, the injection period should be divided into initial or final period during optimization experiment.

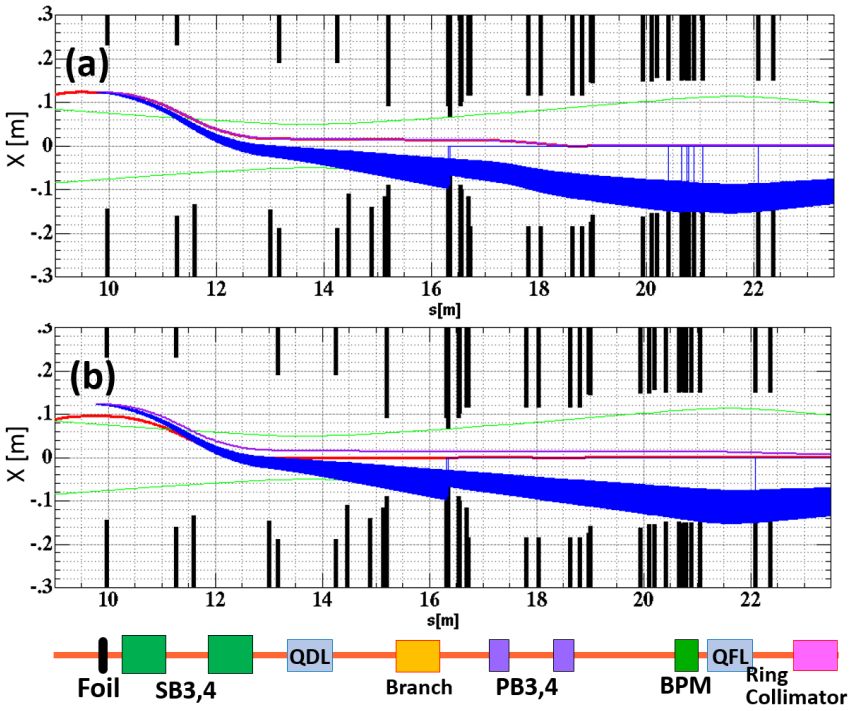

Figure 25: The tracking simulation results for the loss of the inside BPM. The figures (a) and (b) indicate the case of the 1^{st} turn and 305 turns, respectively. The red line is the ring orbit. The purple line is the track of the injection beam. The blue lines are the tracks of scattered particles.

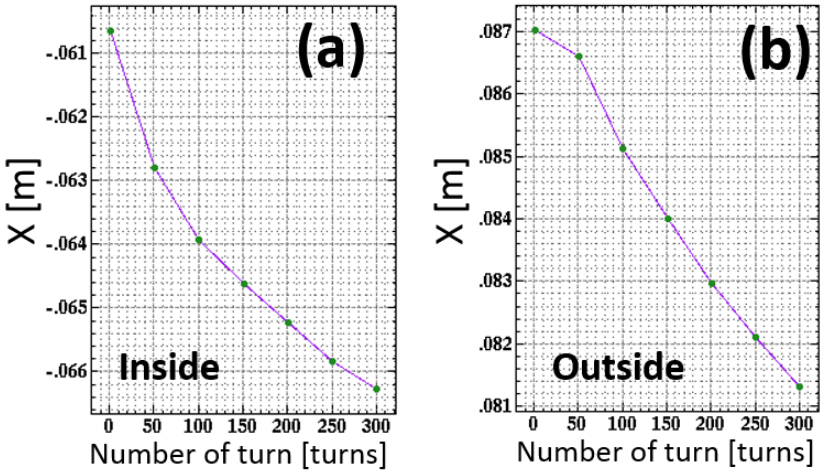

Figure 26: The calculated absorber positions which are required for removing downstream loss. The figures (a) and (b) indicate the cases of inside and outside the absorber, respectively.

4.3 Optimization method of absorber angle

First, the dependence of the localization effect on the absorber surface angle is discussed as follows [33].

A simulation of the protons that collide with the inside absorber and the resulting leakage was performed. The kinetic energy of the protons was 400 MeV. The results are shown in Fig. 27. In this simulation, the same additional simplification were applied to the simulation model as were introduced in the above section in order to restrict the discussion to the angle dependence. The simulation particle source at the foil was different from the simulation model introduced in the above section. From the results of the foil-scattering simulation, it became clear that the angular distribution of the particles that had to be removed at the absorbers was nearly uniform. Therefore, particles that had the same position and additional uniform horizontal angles at the foil was defined as the simulation source. In other words, the beam distribution and vertical angle were not considered. In addition, the bump orbit formed by the SBs and PBs magnets was fixed.

The inside absorber was inserted to reduce the losses located at the inside of the ring. These results indicated that, when the scattered particles and the beam side of the absorber were parallel, the losses were efficiently reduced. On the other hand, when the scattered particles and the beam side of the absorber were not parallel, the losses remained, because the particles that collided with the absorber leaked. These results confirmed the concept of the absorber design and indicated that the angular optimization of the absorbers is important. In addition to the dependence of the localization effect on the angle, the results also clarified that some of the particles colliding with the absorber leaked out to the opposite side.

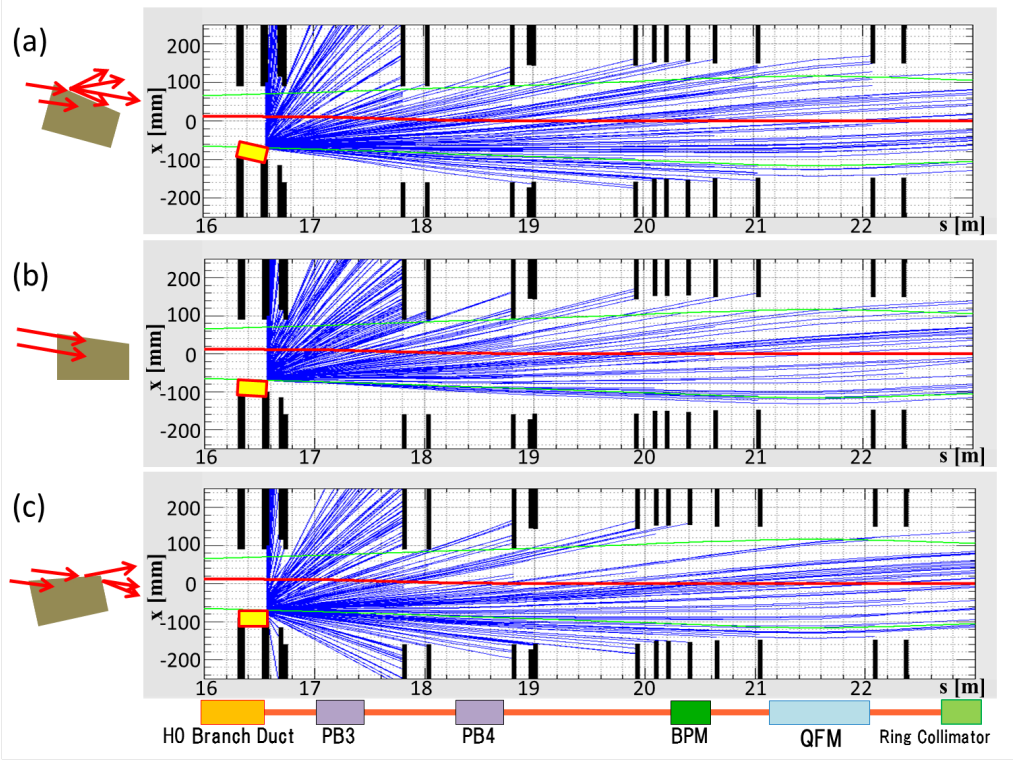

Figure 27: Tracking of the particles leaking from the absorber between the absorber and the ring collimator: (a) rotated 1° toward the beam center; (b) no rotation; (c) rotated 1° away from the beam center.

The large-angle scattered particles and the sides of the absorbers should be aligned in parallel to efficiently localize the losses occurring between the absorber and the ring collimator. Therefore, developing a method to regulate the angle of the absorber was necessary. In particular, the method was desired to be based on the actual beams, instead of only on the calculations performed using the accelerator model. Thus, we explored a method using the simulation model introduced in the above section. Hence, a method was devised for regulating the angle of the absorbers, which was named the loss monitor method (LMM). The details of this method are explained using Fig. 28 as follows.

The inside absorber case is described. From the simulation, it became clear that when losses occurring at the inside of the BPM were intentionally left by not completely inserting the inside absorber, and the absorber was rotated, the characteristic loss dependence with respect to rotation at the inside of the BPM could be determined. This loss dependence is shown in the right-hand part of Fig. 28 and can be explained as follows. Because the pivot of the absorber is downstream, the inner edge downstream of the absorber is nearly fixed. In case 2 of Fig. 28, the scattered particles and the beam side of the absorber are parallel. In case 1, the loss decreases in comparison with that of case 2, because the upstream edge of the absorber approaches the beam center, and more particles collide. On the other hand, in case 3, the loss increases gradually in comparison with that in case 2, because the particles that collide with the front of the absorber in case 2 collide with the side of the absorber and leak out in case 3. Overall, these results indicate that the inflection point of the loss dependence on the absorber rotation is the absorber angle

that is the same as that of the scattered particles. The LMM, therefore, is an effective method for determining the inflection point using a beam loss monitor at the BPM. In addition, the loss dependence on the angle of the absorber between the absorber and the QFM was examined, and the results confirmed that not only a sufficient flight length in the absorber can be maintained for the scattered particles, but also the losses occurring between the absorber and the QFM can be minimized by optimization using the LMM. The loss distributions are shown in Fig. 29. The outside absorber also can be regulated using BLM placed at the outside of the PB4 downstream.

It should be noted that, as a matter of course, an additional insertion after the optimization of the angle using the LMM is required to completely eliminate the losses.

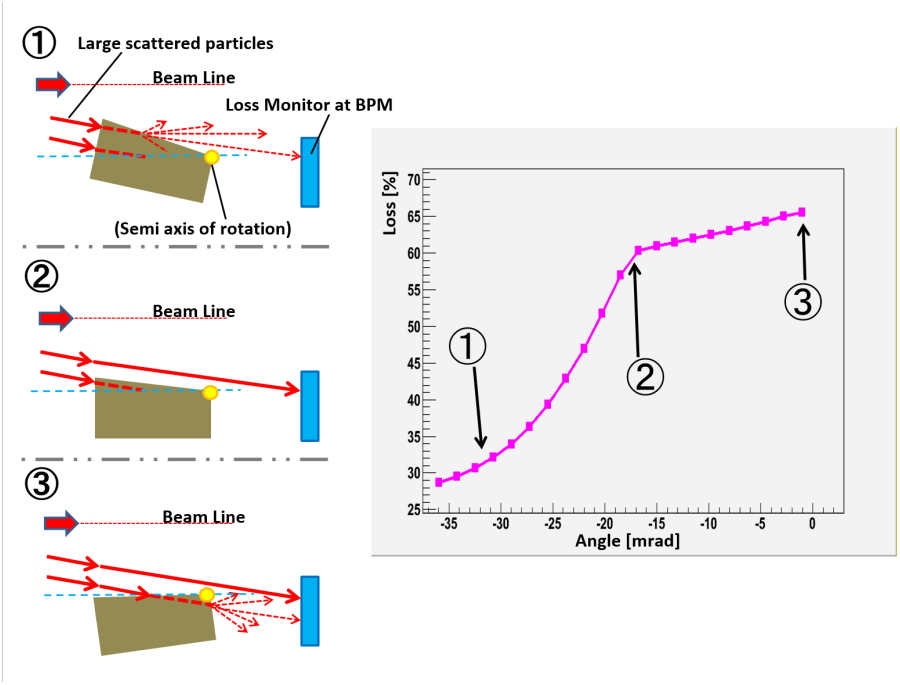

Figure 28: Details of the LMM. The left figures show the schematics of the rotation of the absorber placed on the inside of the ring. The right figure shows the loss dependence on the absorber rotation at the inside of the BPM.

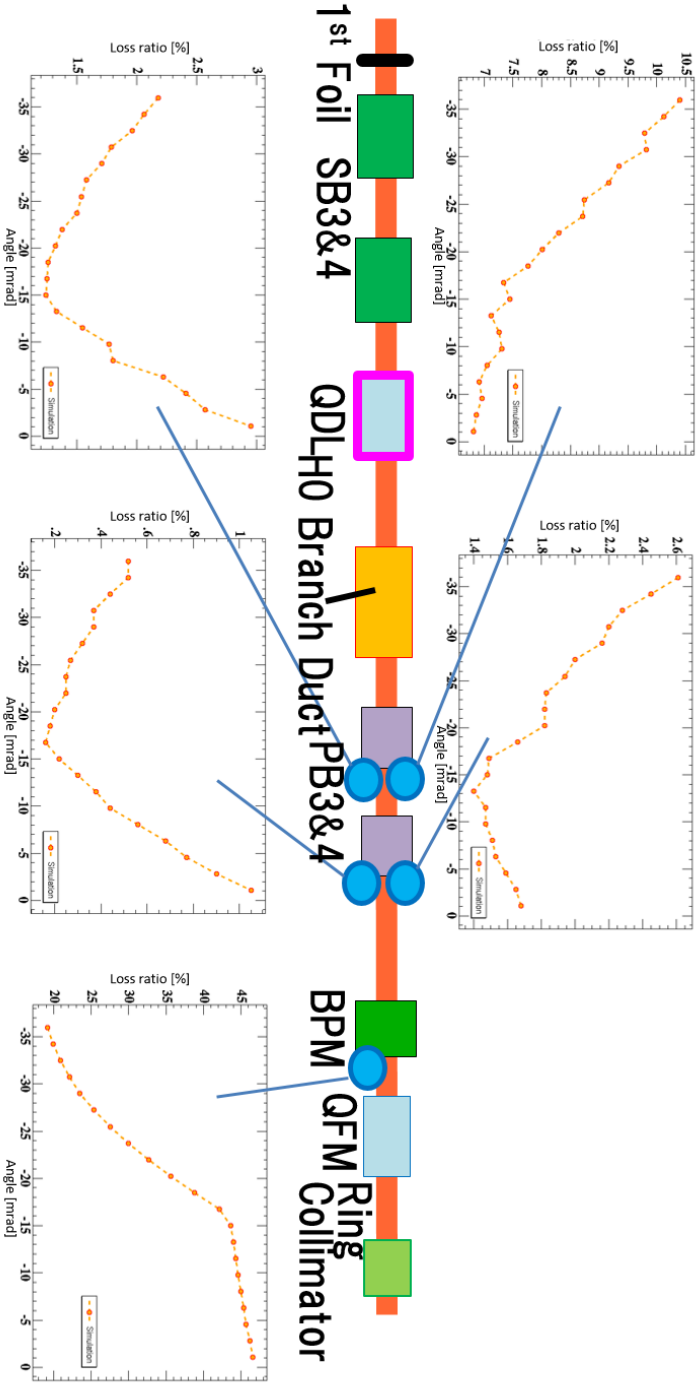

Figure 29: The loss dependence on the inside absorber surface angle at each point.

5 Experimental results

For the LSB-Collimator, the experiment of the absorber optimization was performed in the beam commissioning. In addition, the loss reduction at downstream of the injection area by the LSB-Collimator was confirmed. In this section, first, the setup of the experiment is described. Second, the optimization result of the absorber position is described. Third, the optimization result of the absorber angle with the original method introduced in section 4 is described. Finally, the results of the beam loss reduction at downstream of the injection area by the LSB-Collimator is described.

5.1 Setup of the experiment

The BLM was placed at downstream of the injection area for the LMM and the confirmation of the loss reduction. The experiment was performed with the different condition from the user operation in order to regulate the absorber effectively. In addition, the injection scheme which was different from the normal one was applied in order to compensate for the trouble of SB power supply. These three topics are described below.

5.1.1 Detection system of the beam loss

To detect the beam loss, seven plastic scintillators were placed horizontally as BLMs between the LSB-Collimator and the QFM, and a BLM signal was obtained for 2 ms after the initiation of multi-turn injection. The arrangement of the BLM is shown in Fig. 30. The plastic scintillators were BC-400 series manufactured by Bicron and the photomultiplier tubes (PMT) were H3164-10 manufactured by Hamamatsu-photonics. The details are shown in Table. 2 and 3. The plastic scintillator was 200-mm-long rectangular with 10 mm $\times$ 10 mm cross-section. This structure is shown in Fig. 31.

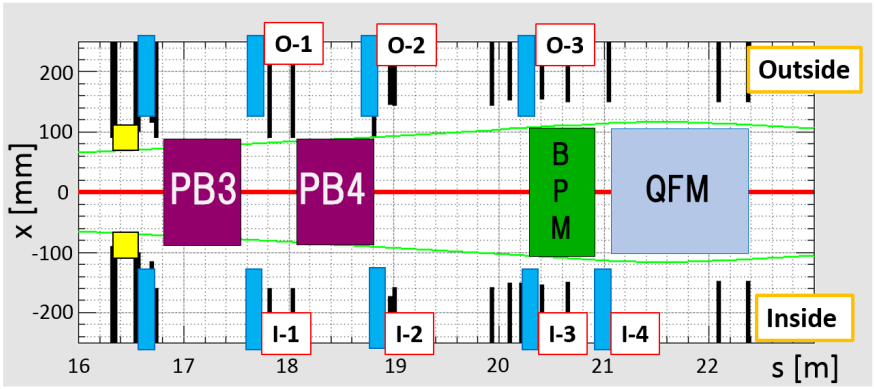

Figure 30: The arrangement of the BLM.

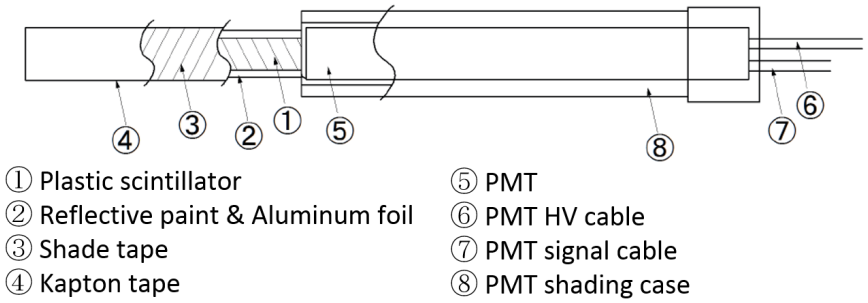

Figure 31: The BLM Structure.

Table 2: The plastic scintillator parameters.

Base Material	Polyvinyltoluene
Density	1.032 g/cm^3
Flexibility	1.58
Luminous efficiency (ratio to Anthracene)	38 $\sim$ 68 %
Rise time	0.7 $\sim$ 1.0 ns
Fall time	1.8 $\sim$ 4.0 ns
Decay length	140 $\sim$ 210 cm

Table 3: The PMT parameters.

Pipe diameter	ϕ: 10.5 mm
Light receiving surface size	ϕ: 8.0 mm
Acceptable Wavelength (Short)	300 nm
Acceptable Wavelength (Long)	650 nm
Acceptable Wavelength (Peak)	420 nm
Rise time	0.8 ns
Fall time	9.0 ns
Transit time	0.5 ns

The sum of the rise and fall times of a plastic scintillator,the PMT, and the transit time spread of the PMT is approximately 15 ns. On the other hand, the bunch length is approximately 400 ns because the cycling time is 1.6 μs with 2 bunches and 50 % chopping at 400 MeV. In addition, the wave data was sampled by the oscilloscope with a sampling rate of 50 MHz corresponding to 20 ns. Therefore, the bunch structure of the loss can be observed. For noise reduction, the wave data of approximately 500 cycles was averaged.

A picture of the placed BLM is shown in Fig. 32. The BLM was locked on the side wall of the chamber. The BLM detects the secondary beams like electron and gamma,

which are created by the proton beam hitting the chamber rather than by the proton beam itself.

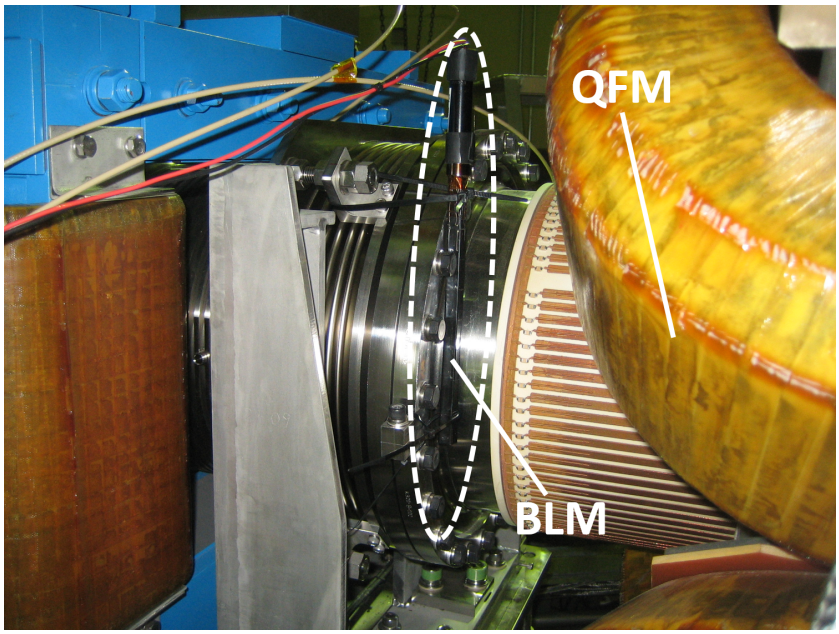

Figure 32: A picture of the placed BLM.

5.1.2 Beam conditions for the experiment

In this section, the beam parameters are summarized. The main parameters are provided as follow and a schematic drawing of the injection beam structure is shown in Fig. 33.

- Peak Current of Linac

  15 mA

- Bunch length of injection beam (chopping length)

  456 ns (90 ns for absorber adjustment)

- Injection period (macro pulse length)

  500 μs (100 μs for absorber adjustment)

- Number of bunch

  2 (1 for absorber adjustment)

- Beam bare tune

  $\nu_x = 6.45$, $\nu_y = 6.42$

- Foil size and horizontal insertion distance

  Vertical size = 20 mm

  Horizontal insertion distance from injection beam center = 10 mm

- RF pattern

  With 2nd RF sweep (Only Fundamental RF for absorber adjustment)

- Transverse painting pattern

  100 π mm mrad Correlated

For the macro pulse length, 500 μs corresponds to 305 turns. The output beam current corresponding to the number of particles is decided according to the peak current, the chopping length, and the macro pulse length. When these parameters are chosen as mentioned above, the beam current is 300 kW, equivalent to 25 Hz. The experiment to adjust the LSB-Collimator was performed after the operational parameter search such as the COD correction by the steering magnets, the chromaticity correction by the sextapole magnets and the foil position search. The painting pattern was chosen from several patterns because the loss was minimized. The experiment was performed with different beam parameters as above in order to decrease the beam power and to avoid synchrotron oscillation. As a result, it became possible to operate with 25 Hz cycling though the extraction beam dump can accept only maximum 8 kW beam. By averaging the BLM data during approximately 20 s corresponding to 500 shots, the low dispersion data were obtained. In addition, by avoiding synchrotron oscillation, the loss signal data became clearer because the timing of the BLM loss signal for each turn became constant.

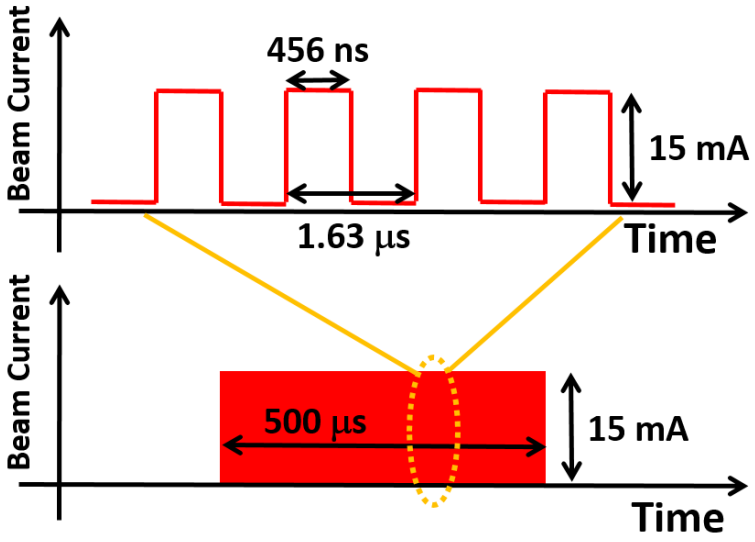

Figure 33: The schematic drawing of the injection beam structure.

5.1.3 Particular injection scheme at 2014 first operation

In the RCS, the ring orbit variation during the painting injection was different from the design owing to the restriction of the SB power supply during the first operation in 2014. This difference is outlined below.

During the painting injection, the ring orbit height decreased along time as explained in section 2.4 and Fig. 7. Normally, the field created by the SBs is fixed and that created by the PB is decreased during injection. Therefore, the injection beam, which passes through SB1 and SB2, can be fixed at the same position and angle. However, in the first operation in 2014, the field created by the SBs decayed owing to the restriction of the SB power supply. The current variation of the SB is shown in Fig. 34. The difference in output between the start and the end of the injection period was 9.17 %. In this case, the ring orbit and the injection line were, unfortunately, gradually separated from normal orbit during the injection period. The difference between the ring orbit and the injection line was 17 mm at the end of the injection period as shown in Fig. 35. Therefore, additional corrections were applied as follows.

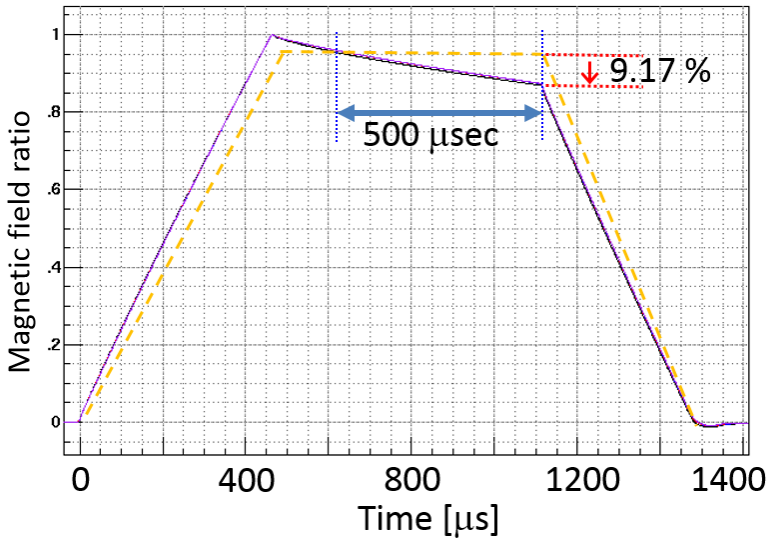

Figure 34: The current variation of the SB. The dashed line indicates the normal case. The solid line indicates the restricted case in this time.

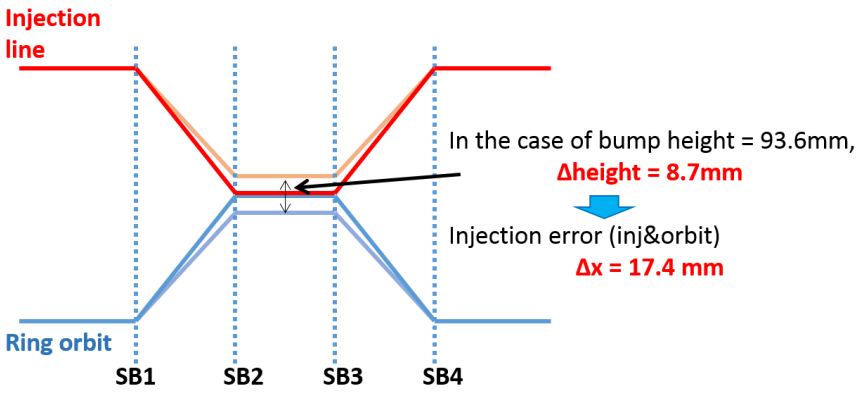

Figure 35: The mismatch between the injection and ring orbit due to the SB problem.

The decay of the SB could be regarded as linear. For the injection beam, the correction was achieved with the PSTRs which originally converted the painting area [34]. The additional kick, which increased along time, was added. Figure 36 shows the time variation of the position which was detected by the Multi-Wire Position Monitor (MWPM) installed at the same position of the foil. As a result, the injection beam could be fixed during the painting injection [35].

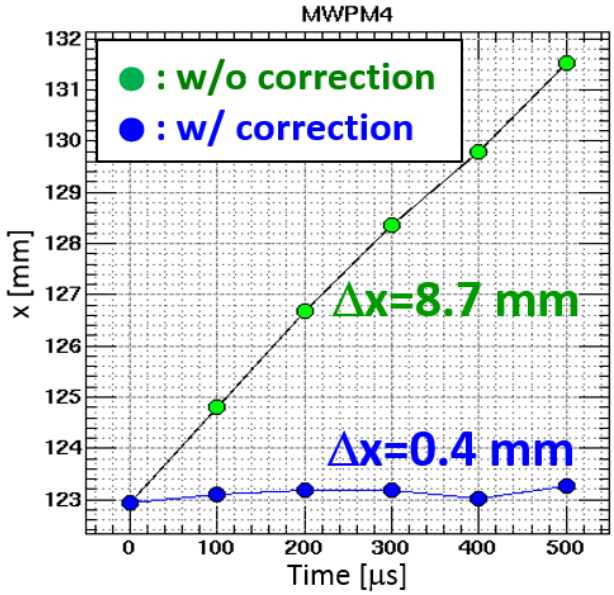

Figure 36: The injection beam position detected by MWPM4, which is located the same position of the foil [35]. The green plots indicate the case without the correction. The blue plots indicate the case with the correction.

For the ring orbit, the deficient height was corrected with additional output of the PBs. The current patterns of the PBs are shown in Fig. 37. The narrow lines indicate normal current patterns. The dashed lines indicate additional patterns used for the correction. The wide lines indicate the sums of these two. Using the wide line patterns, the painting injection became possible as usual on the phase-space at the foil.

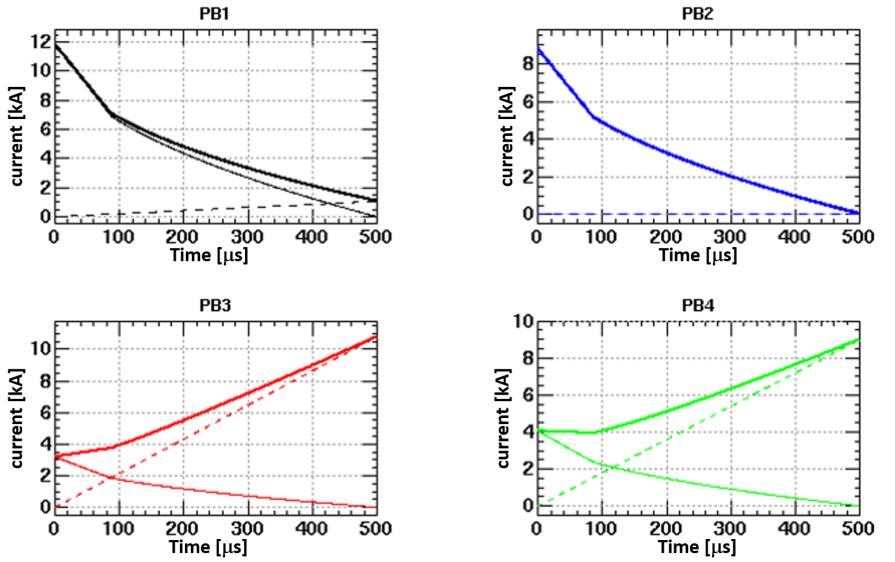

Figure 37: The current patterns of each paint bump magnet [28]. The narrow sold lines indicate the normal pattern. The dashed lines indicate the additional current patterns for the correction. The bold solid lines indicate the corrected patterns corresponding to the sum of the narrow solid and dashed lines.

However, this correction of the ring orbit was undesirable for the LSB-Collimator. Figure 38 shows the ring orbits around the injection area at 0 s and 500 μs. Normally, the ring orbit around the LSB-Collimator returns to the designed center at the end of the injection. However, in the correction case, the ring orbit was kicked out to outside between 16 m and 19 m. Therefore, the scattered particles, which should have been removed by the inside absorber, were also kicked out outside. Thus, the inside absorber had to be inserted with a longer distance than normal case. The estimated results of the required insertion distance are shown in Fig. 41. This is the result of a single tracking from one scattering point on the foil. This tracking is similar to that shown in Fig 25. Although the spread of the scattering point was not considered, the averaged values of the x and x' distributions on the foil were defined as the scattering point for each turn. The beam distributions on the horizontal phase-space during the painting injection are shown in Fig. 39. The averaged values of the x and x' distributions on the foil calculated from the results of Fig. 39 are shown in Fig. 40. This is different from the case of Fig. 26 where the scattering point was fixed as the injection point.

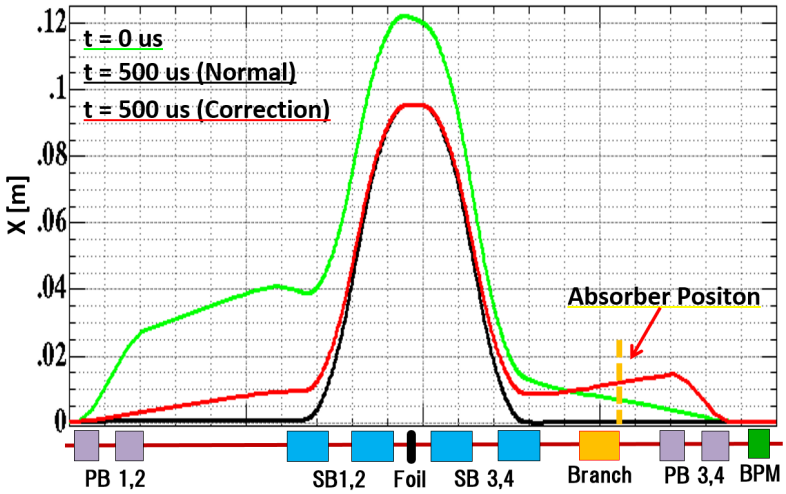

Figure 38: The ring orbits around the injection area. The green and black lines indicate the orbits of the normal case at 0 s and 500 μs, respectively. The red line indicate the orbits with the correction using PB at 500 μs.

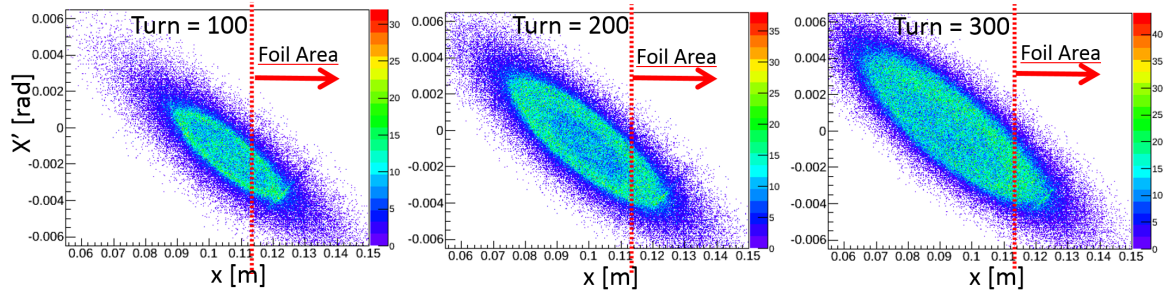

Figure 39: The beam distributions on the horizontal phase-space during painting injection. The painting pattern is 100 π mm mrad Correlated painting. The dashed red lines indicate the edge of the foil.

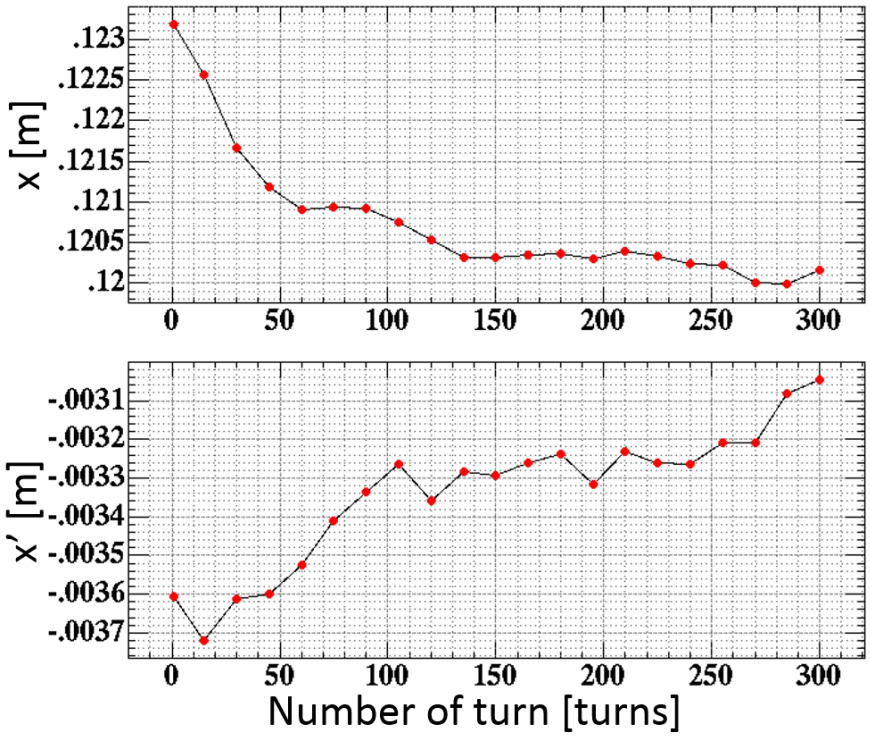

Figure 40: The averaged values of the x and x' distributions on the foil calculated from the Fig. 39. This values are adopted for the calculation of the Fig. 41.

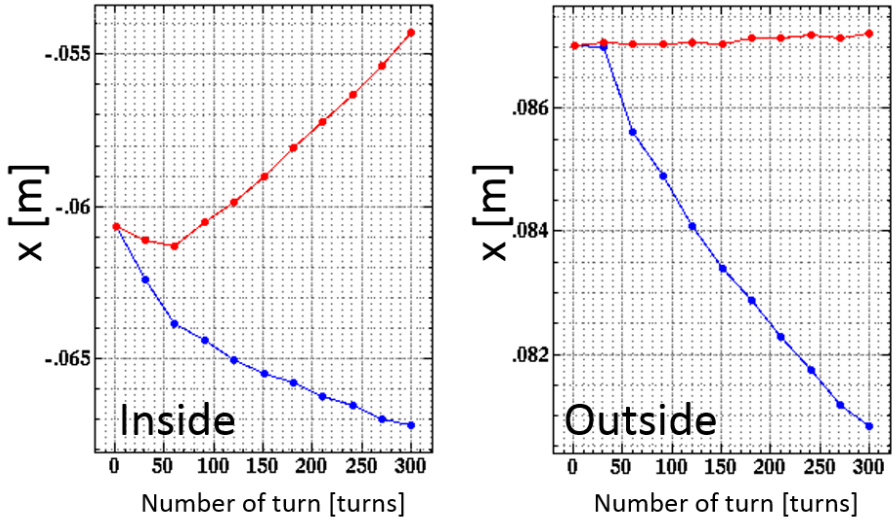

Figure 41: The required absorber positions for removing downstream loss. The left and right figures show aboutthe cases for the inside and outside absorber, respectively. The blue lines indicate the normal SB case. The red lines indicate the corrected case using PB.

From the result of the Fig. 41, it became clear that a long insertion distance is required for the inside absorber at the start or end of the injection period in the normal or correction case, respectively. Moreover in the correction case, the absorber aperture must be set to a narrow 320 π mm mrad, corresponding to -54.3 mm, to completely remove the scattering loss. In this case, the absorber may shave the core-beam and the additional beam loss may occur. On the other hand, for the outside absorber, the insertion distance can be expected to be smaller than that in the normal case.

In addition, the SB decay itself was undesirable for the LSB-Collimator. Normally, the scattered particle angles at the absorber hardly change because these particles pass through only the SBs and QDL whose current is almost constant during the injection period. However, in the correction case, the angles change because of the current variation of the SBs. The time variation of the particle angles at the absorber is shown in Fig. 42. For the inside absorber, the angles may change at approximately 0.7 mrad during the injection period. In other word, the mismatch of the absorber surface angle cannot be prevented during the injection in this case.

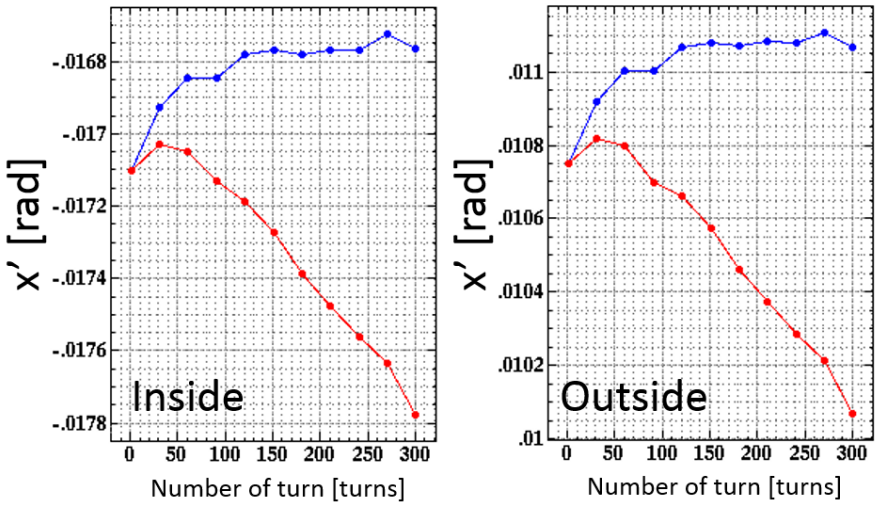

Figure 42: The scattered particle angle at the surface of the absorbers. The absorbers are set at 67 mm from the center corresponding to 486 π mm mrad. The left and right figures show the cases of the inside and outside absorber, respectively. The blue lines indicate the normal SB case. The red lines indicate the corrected case using PB.

5.2 Optimization results of absorber position

This section explains the optimization results of absorber position. Figure 43 shows the time structure of the loss on No. I-4 and O-2 of the BLM indicated in Fig. 43. The injection period was 500 μs. The rapid increase between 0 s and 100 μs is caused by the increase in accumulated particles. Because the ring orbit hardly changes during this time, the number of foil hits approximately increases in proportion to the number of accumulated particles. For I-4, corresponding to the location of the BPM inside, the increment of the loss after 100 μs becomes small because the ring orbit is kept apart from

the foil by the painting injection scheme. On the other hand, for O-2, corresponding the location of the PB4 outside, the foil scattering loss decreases after 100 μs. Because the scattered particles are kicked back inside by PB3 and because the kick angle became more intense along with the injection period in this particular injection scheme, the loss disappears at the end of the injection period. On the basis of the results in Fig. 41, two injection timing were prepared for the optimization. The first is that the beam is injected between 0 s and 100 μs during the painting injection scheme. The second is that the beam is injected between 400 and 500 μs. These timing are called First injection Timing (F-Timing) and End injection Timing (E-Timing), respectively. A schematic drawing of two timing is shown in Fig. 44.

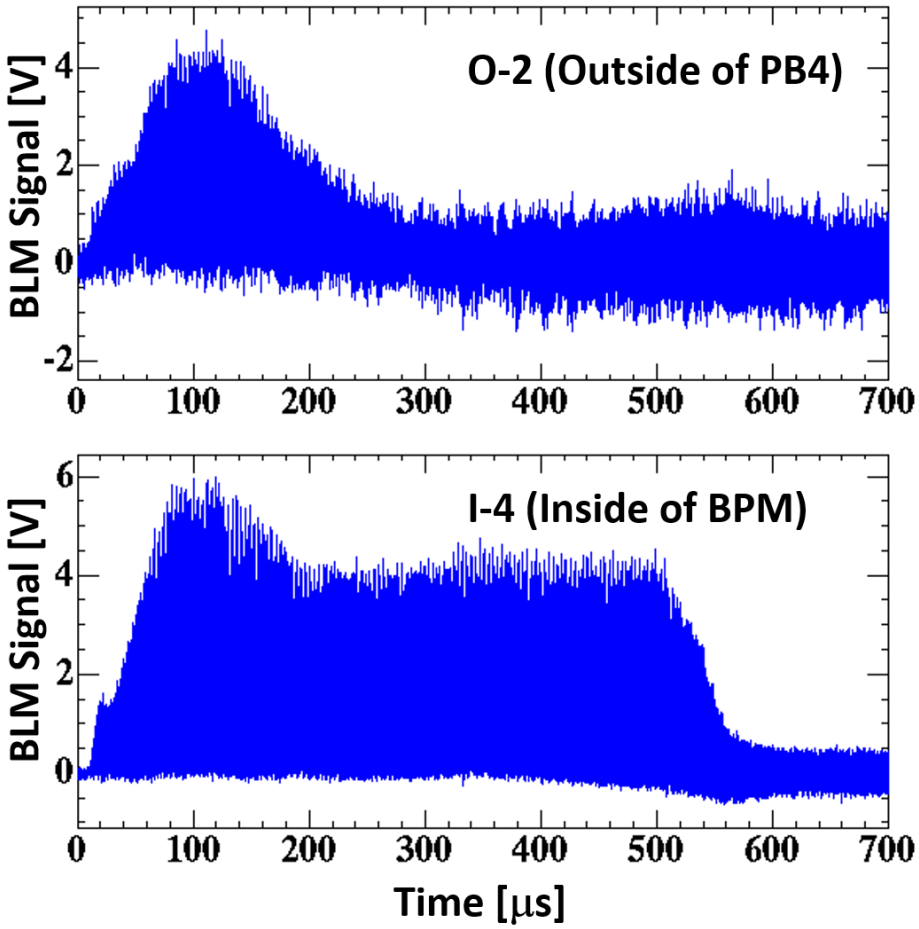

Figure 43: The time structures of the loss. The top and bottom figures indicate the BLM signal at the No. O-2 and I-4, respectively. The beam was injected during 500 μs which was equivalent to 300 kW of output power. The painting pattern was 100 π mm mrad Correlated.

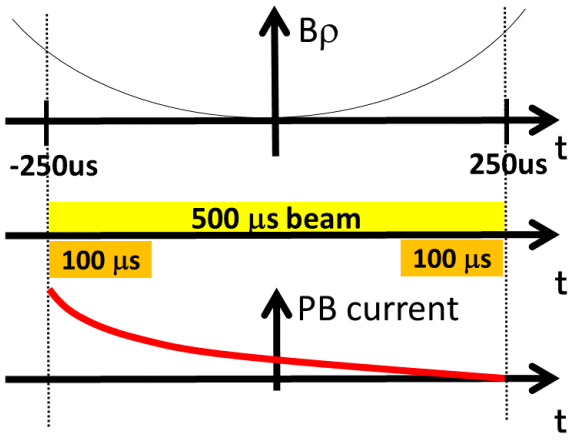

Figure 44: A schematic view of the injection timing. The top, middle, and bottom structures indicate the momentum corresponding to the kick angle of the bending magnets, the beam timing and the decay pattern of the PB current, respectively. The yellow and orange squares indicate the 500 μs and 100 μs beam length, respectively. The left and right orange squares indicate the case of F-Timing and E-Timing, respectively.

The dependence of the loss on the inside absorber insertion at I-4 is shown in Fig. 45. The F-Timing was applied for the case shown on the left side of the plots. For the case shown on the right side of the plots, the E-Timing was applied. The vertical axis indicates the sum of the loss during each injection timing. The error was defined by the fluctuation of the 10 data taken without absorber insertion corresponding to 1 sigma. This error was applied to all data points. As seen in the figure, it was confirmed that the losses caused by foil scattering were suppressed by inserting the absorber. Moreover, it was also confirmed that the required insertion distance for loss reduction was different between the start and the end of the injection period as explained previously. In addition, the increase in the losses caused by leakage from the opposite side of the absorber (e.g., at O-2) was minor.

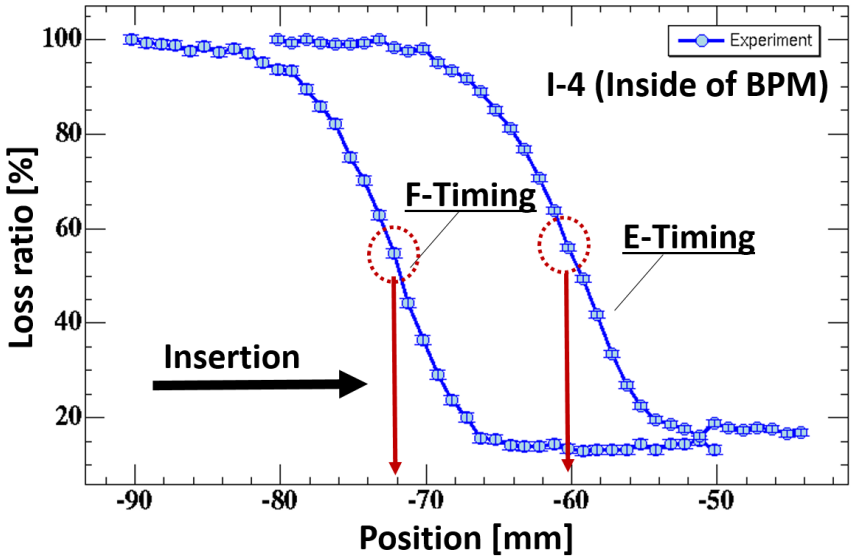

Figure 45: The loss dependence on the inside absorber position insertion at No. I-4 BLM. The loss was defined as the integral between the injection period, corresponding to 100 μs. The left and right plots indicate the case of the F-Timing and E-Timing, respectively. The vertical axis is normalized by the maximum data point. The horizontal axis indicates the absorber position.

On the other hand, the losses that increase along with absorber insertion were observed on the other side of the inserted absorber additionally. The loss dependence on the inside absorber insertion at O-1 is shown in Fig. 46. In this figure, the vertical axis indicates the sum of loss after 700 μs when the injection has already finished. This loss was caused by the halo of the core-beam. When the absorber was inserted too far, the absorber behaved similar to the first collimator of the ring collimator and shaved the halo. The time structure of the losses at the ring collimator and O-1 are shown in Fig. 47 and 48 . As seen, the losses occur with the same timing.

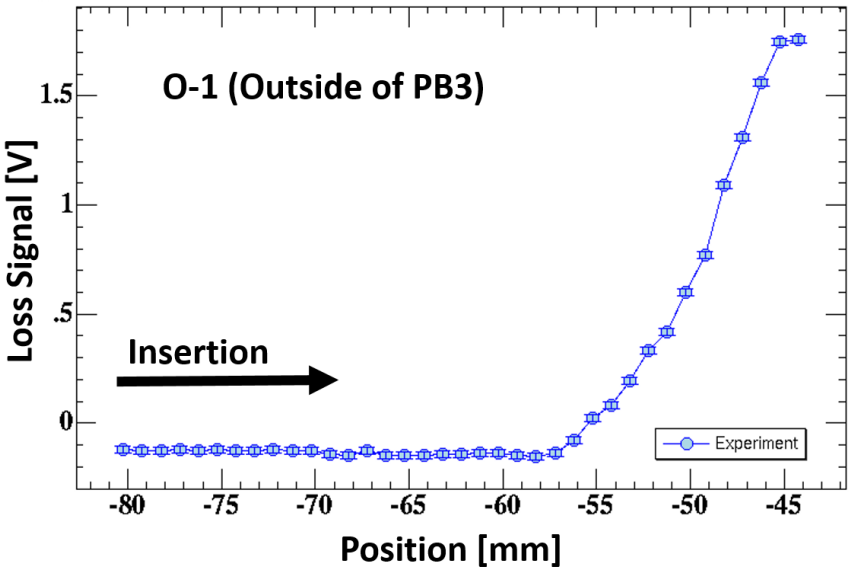

Figure 46: The loss dependence on the inside absorber position insertion at No. O-1 BLM. E-Timing was adopted. The loss was defined as the integral between 700 μs and 2000 μs.

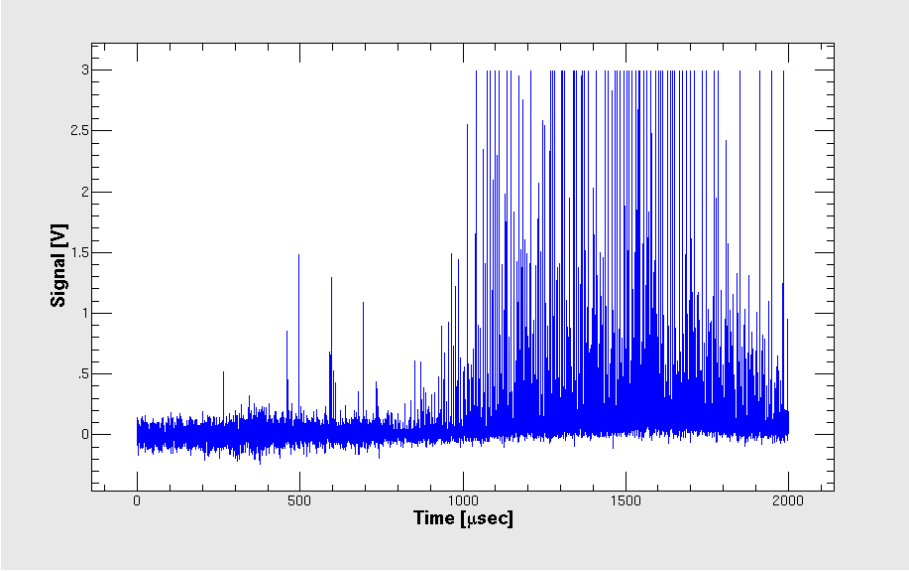

Figure 47: The time structure of the loss at the ring collimator. This data was detected in January 2012 with 181 MeV injection.

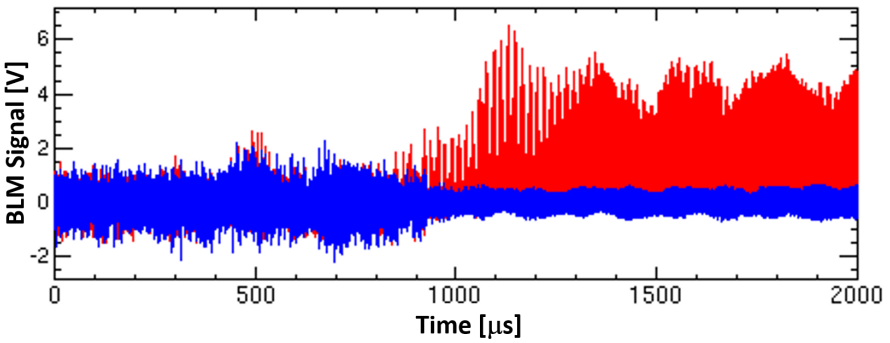

Figure 48: The time structure of the loss at No. O-1 BLM corresponding to that at the outside of the PB3. E-Timing was adapted in the same way as Fig 46. The blue and red plots indicate the loss with -80.23 mm and -55.23 mm inside absorber positions, respectively.

On the basis of the results in Fig. 45 and Fig. 46, the absorber position was decided to set -58 mm though the loss could not be completely removed in this particular injection scheme. However, when the SB power supply is repaired, the maximum insertion distance for loss reduction will be required at the start of the injection, corresponding with the left plots of Fig. 45. Therefore, the loss can be removed without the occurrence of additional loss.

In the same manner, results for the insertion of the outside absorber were obtained. The loss dependence on the outside absorber insertion at O-2 is shown in Fig. 49. Only F-Timing was applied. Thus, it was confirmed that the loss caused by foil scattering at the outer circumference of the PB4 was suppressed by inserting this absorber.

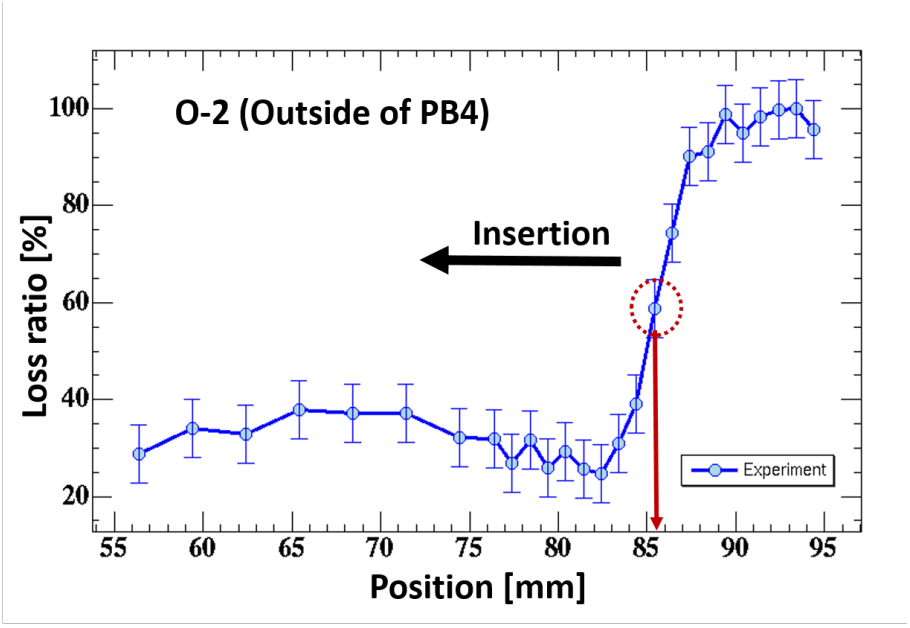

Figure 49: The loss dependence on the outside absorber position insertion at No. O-2 BLM. The loss was defined as the integral between 0 μs and 100 μs. The vertical axis is normalized by the maximum data point. The horizontal axis indicates the absorber position.

5.3 Optimization results of absorber angle

As the next step, the possibility of optimizing the absorber angle using the LMM obtained from the simulation results was investigated. The absorber position was adjusted to retain some losses. On the basis of the results in Fig. 45, the LMM was performed at the inside of the BPM with the -72.23 mm and -60.23 mm inside absorber position using F-Timing and E-Timing, respectively. The loss dependence on the surface angle is shown in Fig. 50 and 51. The error was defined by the fluctuation of the 10 data corresponding to 1 sigma taken in the absorber angle of -18.5 mrad. This error was applied to all data points. The typical loss dependence was obtained as expected. From these results, the angles were determined to be -20.39 mrad for F-Timing and -18.77 mrad for E-Timing. Moreover, in the F-Timing case, it was confirmed that the losses at other points were minimized when the angle of the absorber corresponded with this inflection point. These results are in agreement with those of the simulation.

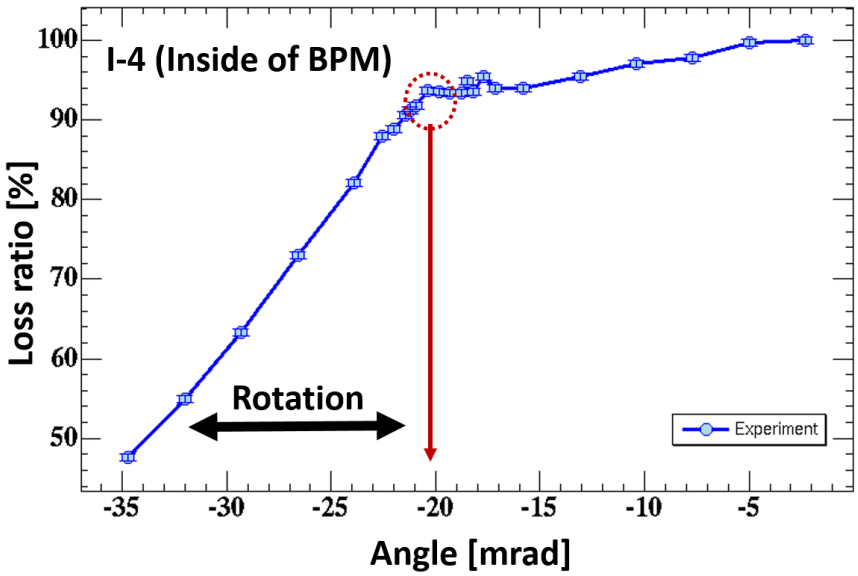

Figure 50: The loss dependence on the inside absorber surface angle with F-Timing at No. I-4 BLM. The loss was defined as the integral between the injection period corresponding 100 μs. The vertical axis is normalized by the maximum data point. The horizontal axis indicates the absorber angle.

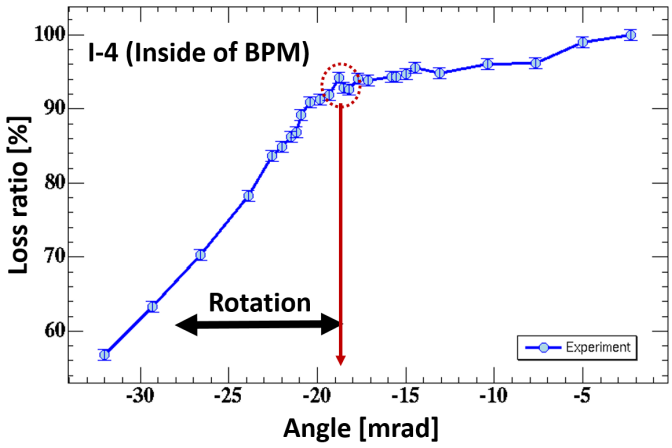

(a) At No. I-4 BLM corresponding to the inside of BPM

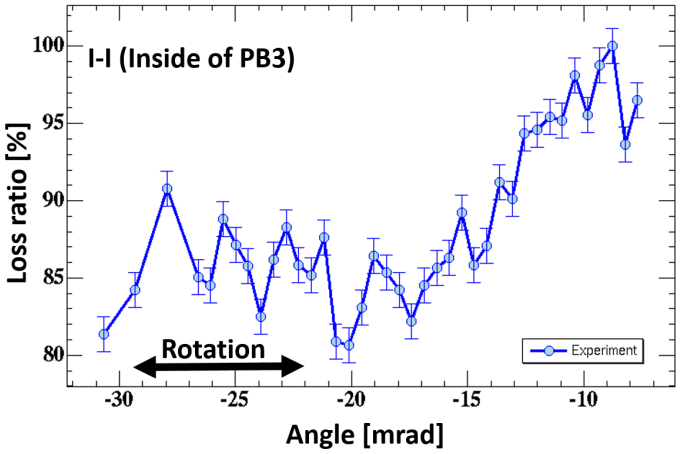

(b) At No. I-1 BLM corresponding to the inside of PB3

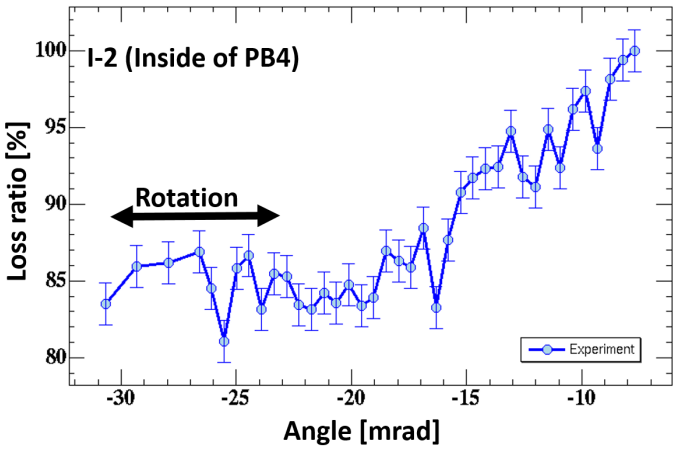

(c) At No. I-2 BLM corresponding to the inside of PB4

Figure 51: The loss dependence on the inside absorber surface angle with E-Timing. The loss was defined as the integral between the injection periods, corresponding to 100 μs. The vertical axis is normalized by the maximum data point. The horizontal axis indicates the absorber angle.

In the same manner, the outside absorber was optimized using only F-Timing. The loss dependence on the surface angle is shown in Fig. 52. The absorber position was set to 85.41 mm and was rotated. The error was defined by the fluctuation of the 10 data corresponding to 1 sigma taken in the absorber angle of 8.5 mrad. This error was applied to all data points. From the inflection point, the absorber surface angle was determined to be set to 20.93 mrad.

Thus, it was confirmed that the LMM can be used for the optimization of the absorbers.

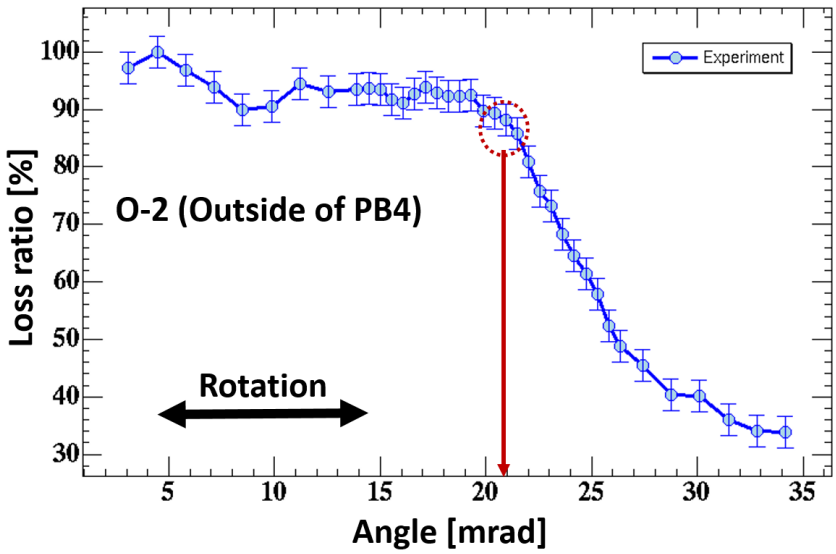

Figure 52: The loss dependence on the inside absorber surface angle with F-Timing at No. O-2 BLM. The loss was defined as the integral between the injection periods, corresponding to 100 μs. The vertical axis is normalized by the maximum data point. The horizontal axis indicates the absorber angle.

5.4 Loss suppression result in 300 kW user operation

The suppression of the beam loss was confirmed during 300 kW user operation. The inside absorber position and angle were determined from E-Timing results. Figure 53, 54, 55 and 56 show the time structure of the loss with and without insertion of the absorbers. The vertical axis indicates the integral of the loss per turn.

Figure 53 and 54 show the case with or without insertion of the inside absorber. Because of leaking from the inside absorber, the loss increased by 1.5 times at O-1 which was on the opposite side from the absorber. However, this increase is not an issue because the original residual dose is several hundreds of μSv/h on contact. For the losses at I-1 and I-2, it was expected that the scattered particles did not collide with the apertures around PB3 and PB4 from the results of the simple tracking simulations such as Fig. 14. In reality, the gain of the BLM was set too higher than that of I-4 or O-2 and the loss barely decreased with insertion of the absorber. Therefore, the secondary particles, mainly gamma-rays, created by collision with the ducts around the branch were expected to be detected in these areas. In addition, it was confirmed that the additional loss caused by

the angle mismatch did not occur at I-1 and I-2.

Figure 53 and 55 show the case with or without insertion of the outside absorber insertion. Because of the leak from the outside absorber, the loss increased by 1.5 times at I-1. However, this increase is also not an issue for the reasons similar to the inside case.

Figure 53 and 56 show the case with or without insertion of both absorbers. On the inside of the BPM, although the loss around the end of the injection period remained owing to the time decay of the shift-bump magnets current, the scattering beam loss was reduced to 25.4 %. At the outside of the PB4, the loss was reduced to 21.3 %. The residual doses were 0.90 mSv/hr and 0.26 mSv/hr after one operation cycle at a 300 kW, respectively on contact. After all of this, maintenance of the devices around the BPM became possible. In addition, the loss at the inside of the BPM will be suppressed further when the power supply of the shift-bump magnet will be upgraded.

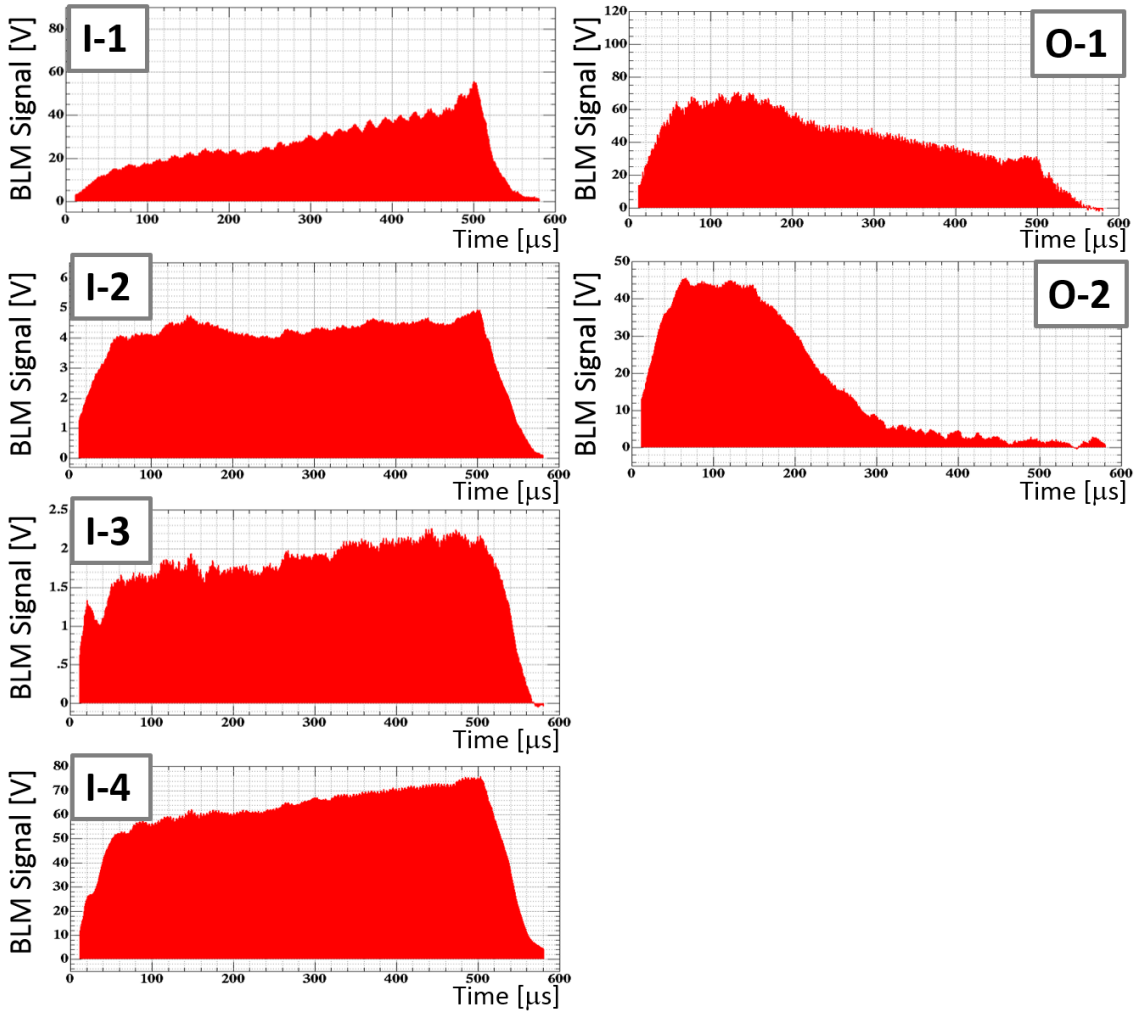

Figure 53: The time structures of the loss without absorber insertion. The pictures show the loss at each BLM indicated in the upper right or left of pictures.

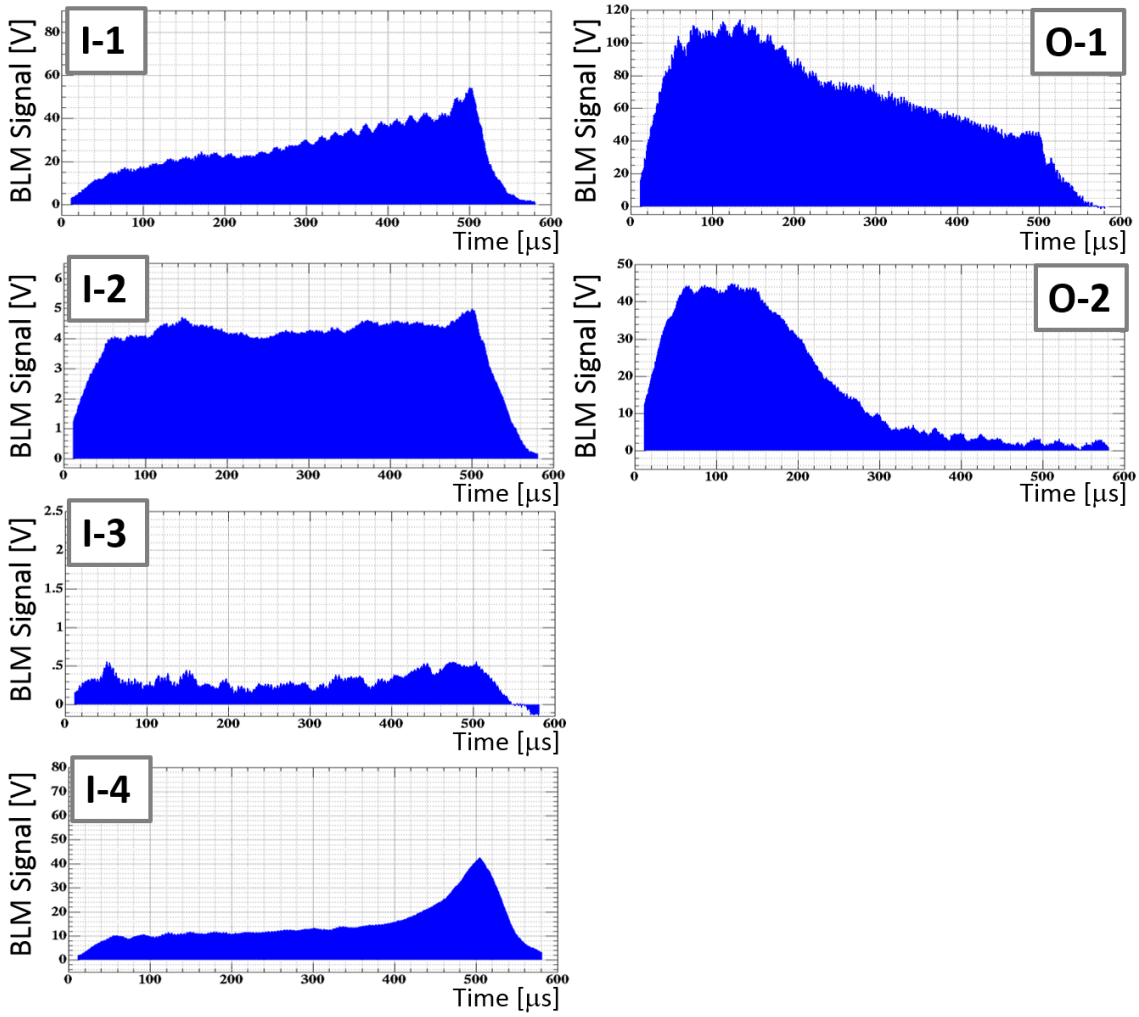

Figure 54: The time structures of the loss with inside absorber insertion. The pictures show the loss at each BLM indicated in the upper right or left of pictures.

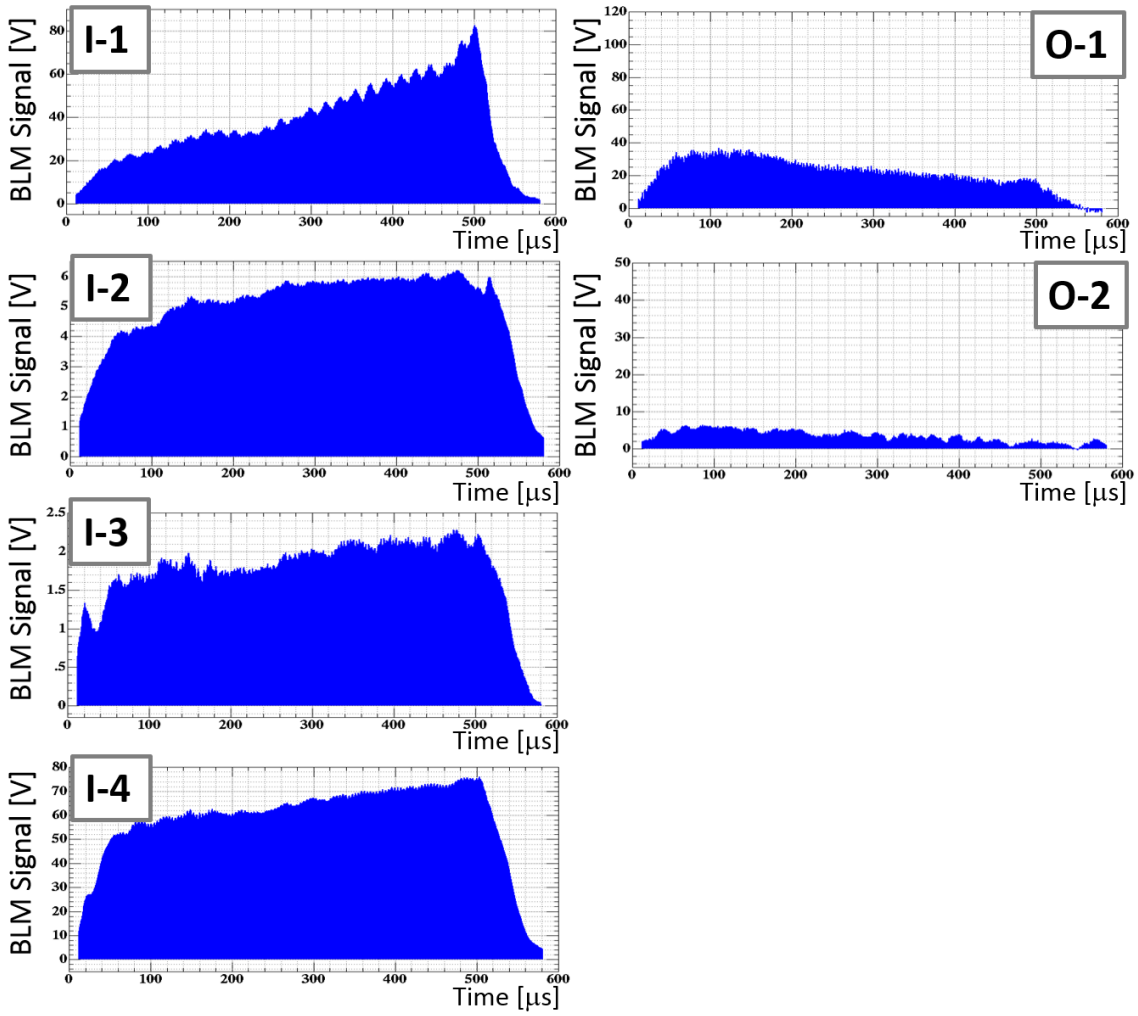

Figure 55: The time structures of the loss with outside absorber insertion. The pictures show the loss at each BLM indicated in the upper right or left of pictures.

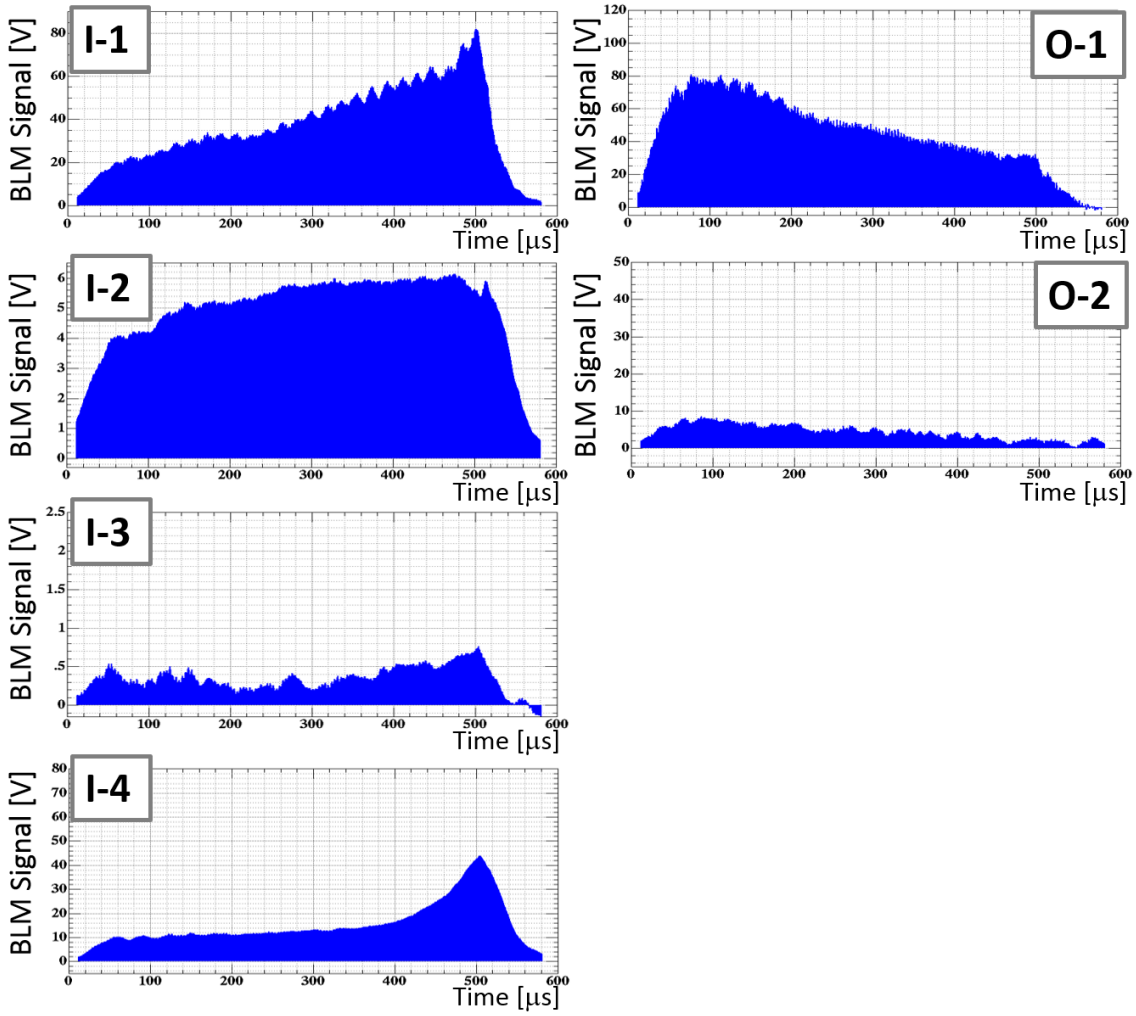

Figure 56: The time structures of the loss with inside and outside absorber insertion. The pictures show the loss at each BLM indicated in the upper right or left of pictures.

6 Simulations and Discussion

From the results of the experiments, localization of the loss was achieved. In other words, the large-angle foil scattering beam loss was solved for the 300 kW operation. However, the target beam power of the RCS is 1 MW. Hence, the estimation of the residual dose for the 1 MW power is desired. Therefore, it was performed through the comparison between the experimental and simulation results. First, it was confirmed that the large-angle foil scattering beam loss was reproduced well by the simulation for the 300 kW operation. And then, the estimation was performed by applying the ratio of the simulation result to the detected residual dose value in the 300 kW operation to the 1 MW simulation result.

In this section, first, the modeling of the beam condition for the realistic simulation is described. Second, the results of the comparison between the experimental and simulation results are described. In particular, it is described that the loss at the inside of the BPM was reproduced well by the simulation for the 300 kW operation. Finally, the estimation result of the residual dose for the 1 MW power is described. In addition, the method of the further beam loss suppression is discussed.

6.1 Modeling of the beam condition for the realistic simulation

In the simulation, the particle distribution calculated by SIMPSONS at the foil is especially important because it becomes the source for other simulations which are introduced in Fig. 22. If the distribution is inaccurate, the number of particles that hit the foil cannot be correctly determined. Because the multi-turn injection is adopted in the RCS, the distribution after the injection period is primarily determined by the painting injection pattern and the injection beam shape. Therefore, these two factors were applied to the SIMPSONS parameters on the basis of the experimental data. The details of this will be described in the following sections.

6.1.1 Injection beam

On the basis of the past commissioning experience, the standard injection beam for simulations was defined as a Gaussian beam with a beam emittance of 4 π mm mrad, which corresponds to 4 σ. However, for the first operation in 2014, the measured injection beam was broad compared with the design beam. In addition, the beta and alpha functions of the injection beam were also different from the design parameters at foil. Therefore, the distribution was constructed using experimental data.

Figure 57 shows the detected injection beam distributions at MWPM4, installed in the same position on the foil. The u and v planes of MWPM were tilted at 17.7 degrees from the horizontal and vertical planes. The distributions were fitted using Gaussian. The design and analyzed injection parameters are summarized in Table 4.Thus, the horizontal and vertical emittances were 5.4 and 2.5 π mm mrad corresponding to 4 σ, respectively. Figure 58 shows the phase-plane plots of the injection beam for the painting injection. When the beam is painted as designed with 100 π painting, the beam is formed with 280 π in the horizontal and 95 π in the vertical, respectively. This horizontal emittance growth may cause an increase in the foil hit probability.

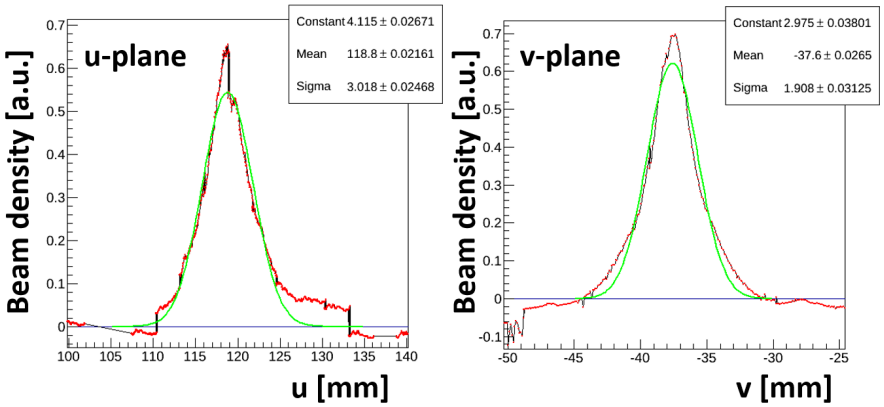

Figure 57: The detected injection beam distributions at MWPM4. The left and right figures indicate the u and v plane distributions. The red plots are experimental data. The green lines are the Gaussian fitting results.

Table 4: The injection beam parameters.

	Design	Analysis
α_x	-1.252	-5.867
β_x	10.226	31.434
α_y	-1.822	-1.476
β_y	8.995	19.154
4σ-ε_x	4 π mm mrad	5.38 π mm mrad
4σ-ε_y	4 π mm mrad	2.50 π mm mrad

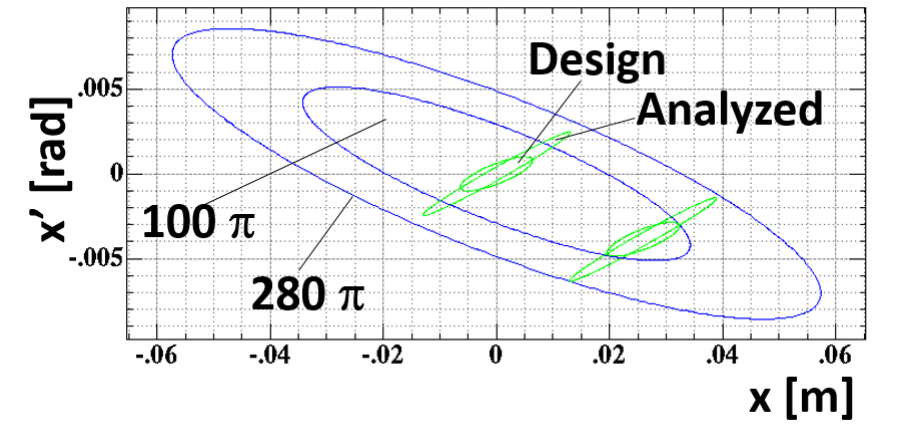

(a) x-x' plane

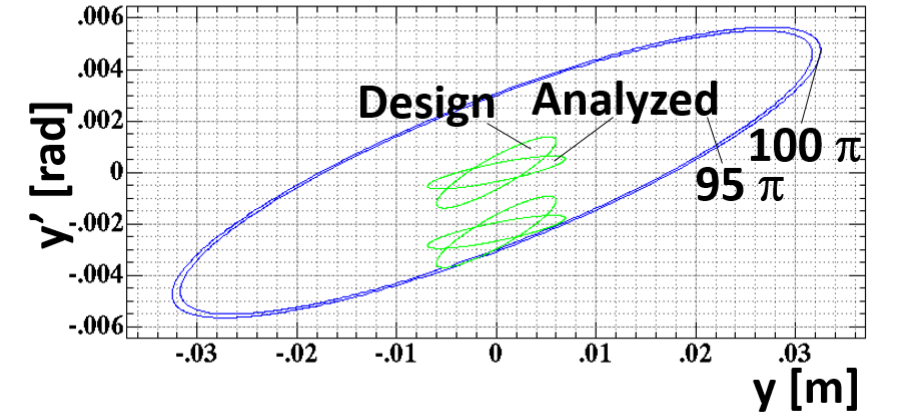

(b) y-y' plane

Figure 58: The phase-space plots of the injection beam at the start and end of injection period. The design and analyzed injection beams are shown. The top and bottom figures indicate the x-x' and y-y' plane, respectively.

6.1.2 Time variation of ring orbit during painting injection

For the painting injection, the injection beam position and angle are changed proportional to the square root of time in order to put the injection beam on the phase-space uniformly. However, in practice, these two parameters are changed proportional to the time from the beginning of injection to several tens of microseconds because the rate of change at 0 s is infinite in this case. During the operation of the accelerator, a few tracking errors occur at the paint-bump magnet power supply and the time variations of the position and angle diverge from design pattern. Therefore, the simulation must use the measured time variations.

Figure 59 shows the beam position data from the BPM and Figure 60 shows the beam

and data taking trigger timing. Because the injection was finished until 0 μs, the beam position data could be obtained including $t = 0$ μs during the painting injection period. By fitting this data using only PB1-4, the ring orbit could be obtained and the positions and angles at the foil could be obtained each time. As shown in Fig. 59, the COD occurred at the start of the injection because of the imbalance of PBs currents.

Figure 61 shows the time variations of the ring orbit position and angle at the foil in the horizontal plane during the injection period. The measured position was different from the designed one. For the vertical plane, the time variations were directly detected using MWPM4.

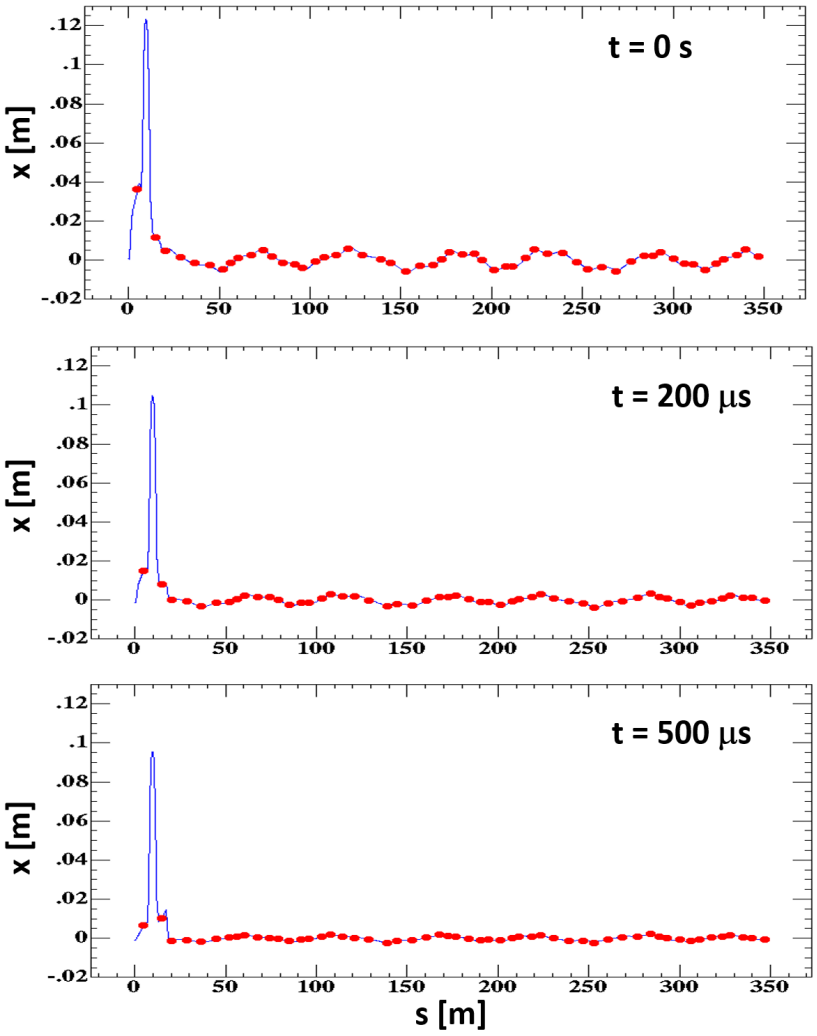

Figure 59: The time variations of the ring orbit. The red plots indicate the BPM experimental data. The blue lines indicate the fitting results using PB1-4. The top, middle and bottom figures indicate the ring orbits at 0, 200 μs and 500 μs from the start of injection, respectively.

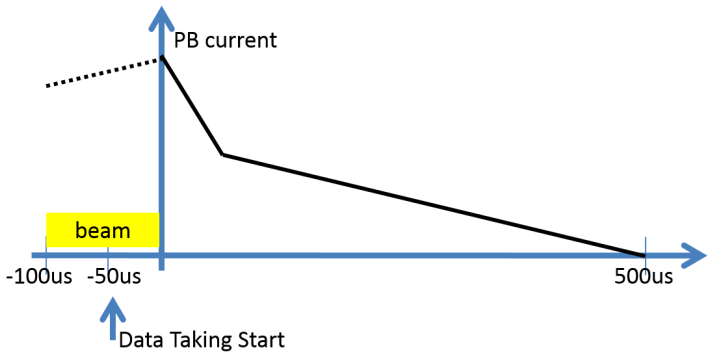

Figure 60: The beam and data taking timing.

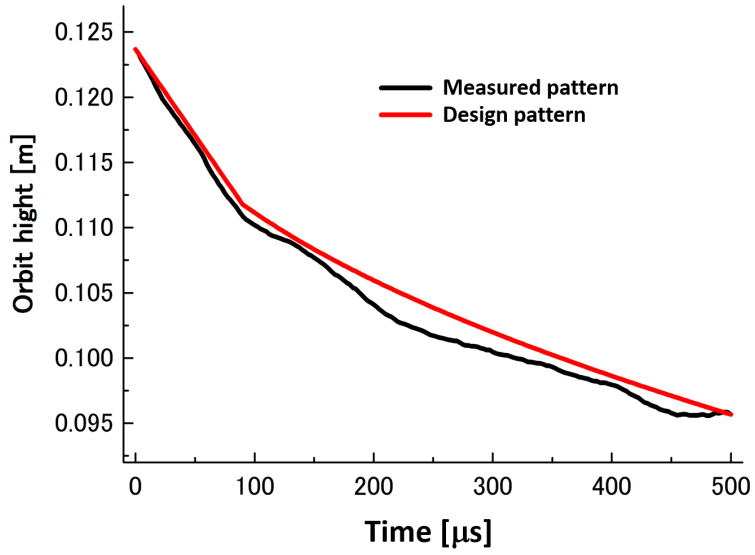

(a) Time variation of x

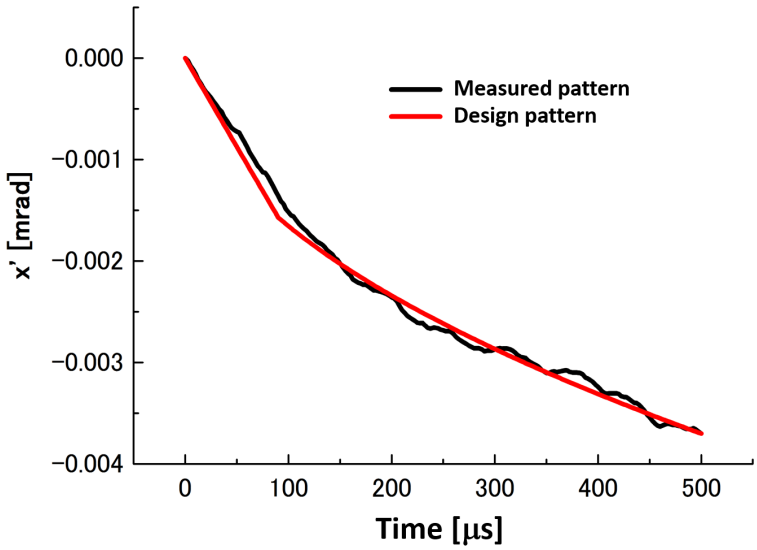

(b) Time variation of x'

Figure 61: The time variations of the ring orbit position and angle at the foil in the horizontal plane. The red and black lines indicate the design and analyzed painting patterns, respectively.

6.1.3 Other error sources

For the SIMPSONS simulation, various error components were considered in order to reproduce the experimental results. In reality, the simulation could reproduce as introduced

in the section of RCS introduction. In this section, some components will be introduced.

The first is the shift bump ripple [36]. This rectangular ceramic chamber is placed between shift bump magnet yokes. Because the electroformed copper stripes are plated on the outside of the chamber, an induced current flow is created by the shift bump magnet field when the passes of stripes arent symmetrical or the magnet power supply itself has a ripple. Because the current also produce an additional AC field, the beam is kicked, unfortunately. For the previous 181 MeV injection energy, this ripple was a serious problem for the beam loss because the frequency of the ripple was near the operational tune. For the present 400 MeV injection energy, the frequency was separated from the operational tune, and the passes of stripes were formed symmetric using a new condenser and the ripple of the power supply was reduced. Thus, the ripple did not cause the beam loss.

The second is the leakage field at the extraction area. In the RCS, the leakage field from the extraction septum and the magnets installed on the extraction branch line disordered the symmetry of the lattice particularly. Therefore, an additional magnetic shield was applied. In addition, a chamber, which has a magnetic shielding effect was developed and installed at the extraction area [37]. Thus, the leakage field was suppressed. In the simulation, the leakage field was applied as kick angles based on the experimental results. Specifically, the ring orbit was detected with or without the field of the extraction magnets and fitted with additional kick angles.

In the SIMPSONS simulation, an alignment error, an individual difference in magnets, the ripple of bending magnet, and others were also considered on the basis of the experimental results.

6.2 Comparison between experiment and simulation results

6.2.1 Foil hitting probability

Figure 62 shows the simulated number of foil hits. The injection beam parameters summarized in Table 4 are applied. The painting patterns shown in Fig. 61 are applied. The foil edge was set at a distance of 10 mm from the beam center. The foil positions and the foil hit conditions on the phase space are shown in Fig. 63.

For the design paint pattern and beam size, the number of foil hits increases up to several tens of microseconds and then decreases as time goes on. For the design paint pattern and measured beam size, the number of foil hits increases overall compared with the former case. On the other hand, for the measured paint pattern and beam size, the number of foil hits is roughly constant during the injection period. Thus, the number of foil hits depends on the difference between the painting pattern and the beam size. In particularly, when the injection beam was wide, the number of foil hits did not decrease at the end of the injection with the painting scheme because the circulating beam became wide. Figure 64 shows the BLM signal during injection without absorber insertion at I-2. The loss was defined as the integral over each turn. At the I-2, it is expected that the secondary particles, mainly gamma-ray, created by collisions with the ducts around the branch are detected as explained in a previous section. Because the scattered particles that create the secondary particles are only affected by SB and QDL which hardly change their currents during the injection period, the acceptance of BLM by the secondly particles

is almost constant during the injection period. In other words, the time structure of the beam loss at I-2 is expected to directly reflect the number of foil hits. Actually, a comparison of this result with Fig. 62 revealed that the time structures corresponded well with the simulation result of the number of foil hits. These results confirm that the simulation can reproduce the experiment.

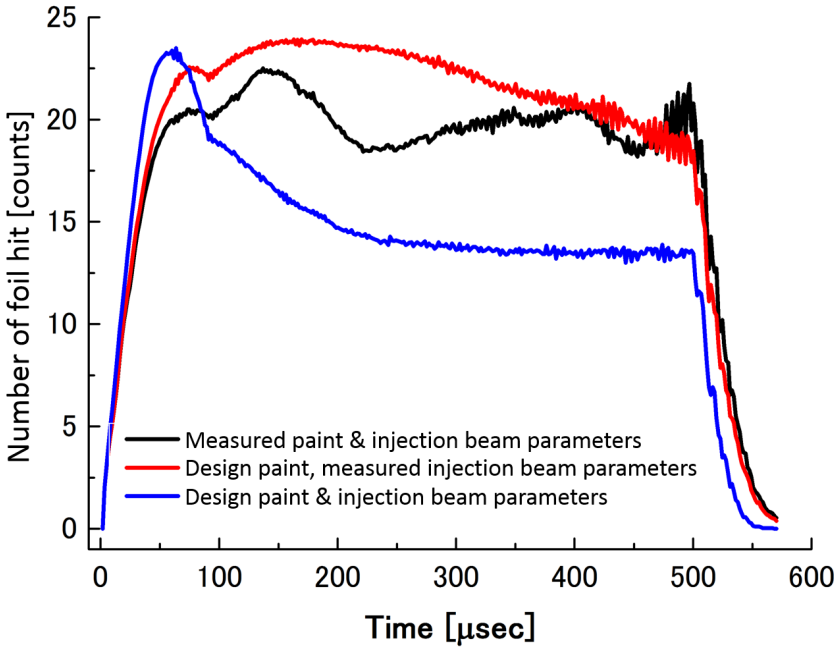

Figure 62: Simulation results for the number of foil hits. The black, red, and blue lines indicate the simulation results given the measured paint and measured injection beam parameters, design paint and measured injection beam parameters, and design paint and design injection beam parameters, respectively. The vertical axis means the number of hits among 305 particles which corresponds to the total number of injected particles in the simulation.

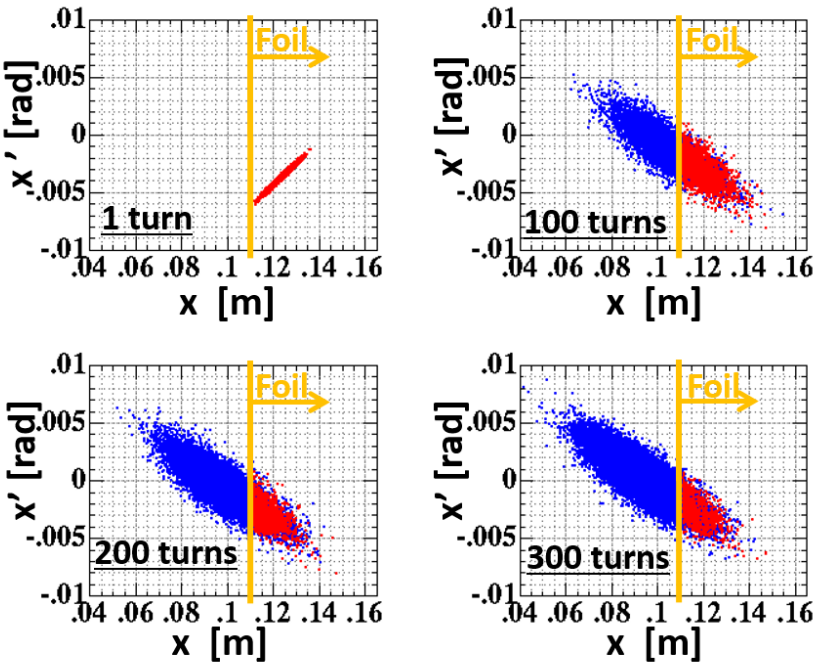

(a) x-x' plane

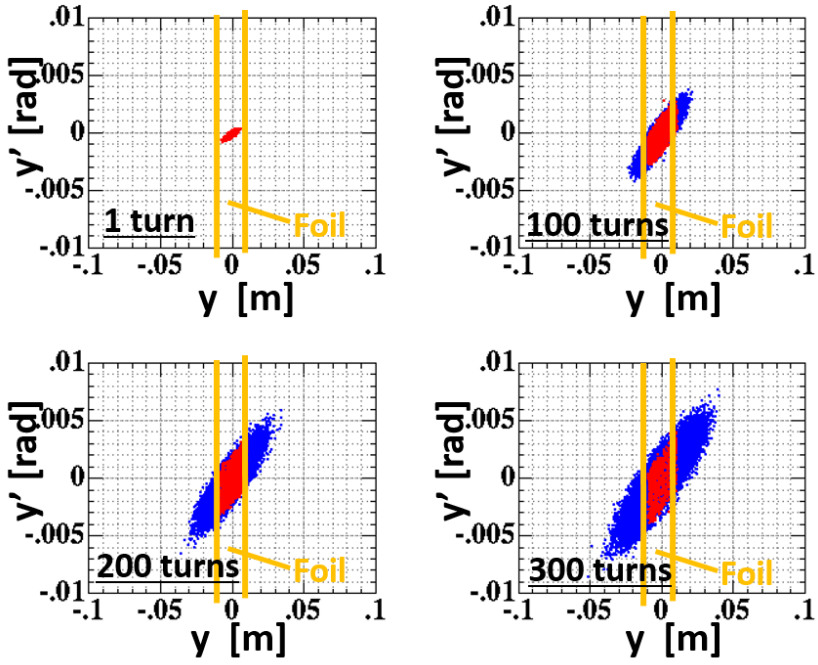

(b) y-y' plane

Figure 63: The foil positions and the foil hit distribution on the phase-space during the painting injection period. The red and blue plots indicate the particles that collide and do not collide with the foil, respectively.

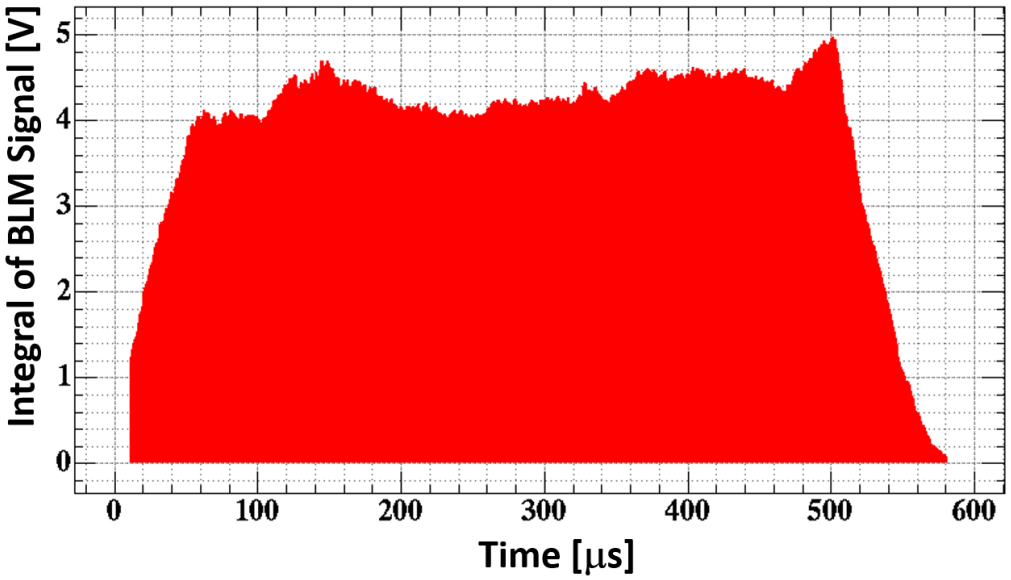

Figure 64: The time structure of the loss at I-2. This is experimental data. The loss was defined as an integral for each turn. The beam power was 300 kW equivalent with 100 π mm mrad Correlated Paint.

6.2.2 Absorber position

Figure 65 and 66 show the simulation results for the loss dependence on the inside absorber position at the I-4 and the outside absorber position at the O-2. The experimental data corresponding with Figs. 45 and 49 are also shown in same plot. In this simulation, the absorber model created using GEANT4 was not applied. The beam tracking was performed using only SAD. The apertures which were substituted for the absorbers were inserted. Because these completely remove the colliding particles, the zero values of the simulation results were considered as the average value of experimental data over -64 mm or -50 mm in Fig. 65 and under 80 mm in Fig. 66. In addition, in order to consider BLM acceptance, two modifications were applied around the BPM. The first was that the perpendicular wall was defined as the duct aperture around the BLM. A schematic drawing is shown in Fig. 66. The BLM was placed on the chamber surface, and the detectable particle collision area was restricted owing to the BLM length. This area is indicated by the purple arc in Fig. 66 (a). Accordingly, when the aperture was defined with a circular duct, a miscount of loss occured as indicated in Fig. 66 (a). Therefore, the perpendicular wall was set to cover only the detectable area. As a result, for the loss dependence at I-4, the absorber positions where the loss disappeared became clear.

The second modification was that the sum of the losses at some apertures, which were arranged around the BPM, were determined as the simulation results. For the BPM, the loss disappears from the upper stream to the lower stream along insertion of the absorber. When it was defined that the beam loss in the upstream region of the BPM was detectable by the BLM, the loss reduction occurred with a small insertion distance in the simulation result. On the other hand, when it was defined that the loss at the downstream region

of the BPM was detectable, the loss remained even with large distances. In other words, the extent of the apertures where the loss is detectable by the BLM corresponds to the slope width of the loss dependence. By selecting the suitable extent of the apertures, the slope of the loss dependence corresponded with the experimental one very well.

The results in Figs. 65 and 66 confirmed that the time variation of the ring orbit owing to the SB issue and the apertures considered the BLM acceptance were reconstructed in the simulation very well. Therefore, simulating the angle optimization using same scheme as in the experiments became possible.

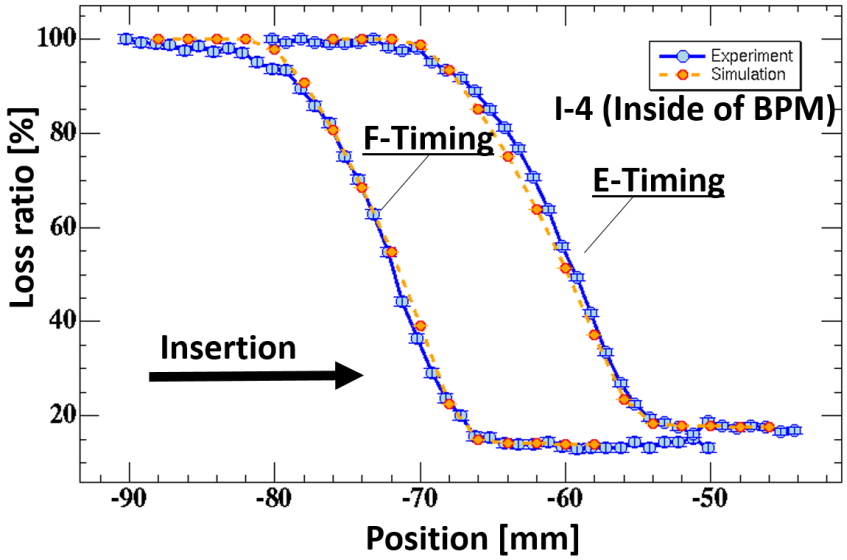

Figure 65: The simulation results of the loss dependence on the inside absorber position at I-4. The blue plots are experimental data corresponding to Fig. 45. The orange plots are simulation results. The vertical axis is normalized by the maximum experimental data point. The horizontal axis indicates the absorber position.

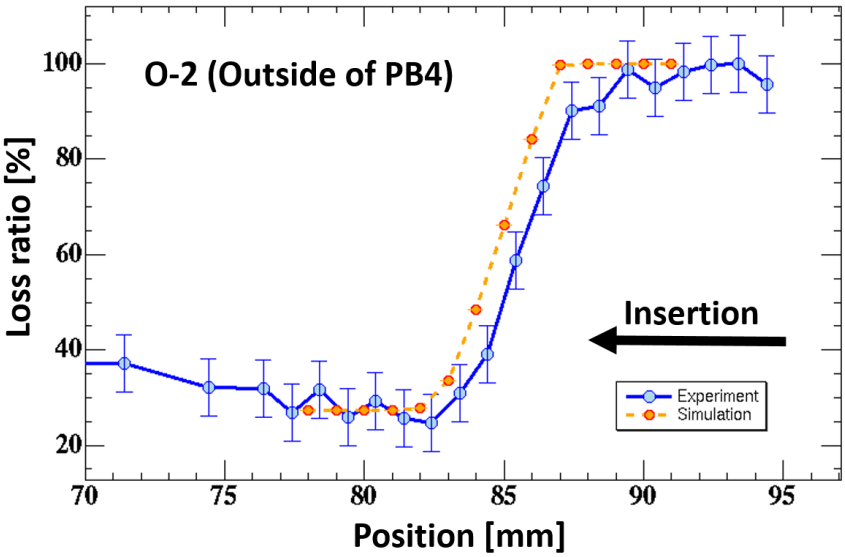

Figure 66: The simulation results of the loss dependence on the outside absorber position at O-2. The blue plots are experimental data corresponding to Fig. 49. The orange plots are simulation results. The vertical axis is normalized by the maximum experimental data point. The horizontal axis indicates the absorber position.

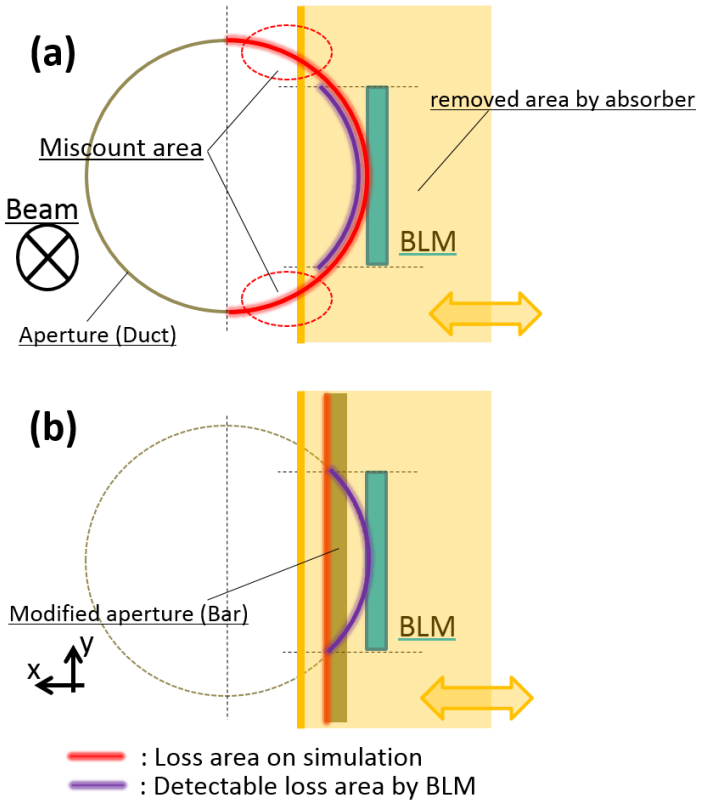

Figure 67: A schematic drawing of the duct aperture around the BPM in the simulation.

6.2.3 Absorber angle

Figure 68 and 69 show the simulation results of the loss dependence on the inside absorber angle at the I-4 and the outside absorber angle at the O-2. The experimental data corresponding to Fig. 50, 51and 52 are also shown in the same plot. In these figure, the horizontal axis of the simulation result was corrected to be the same as the experimental result based on each inflection point. The loss values of the simulation results were normalized using only the value of each inflection point. Thus, these simulation results were in good agreement with the experimental data. In other words, the horizontal axis of the experimental result was shifted from that of the simulation result. In the Fig. 68, the difference in the horizontal axis between the simulation and the experiment was approximately 3.3 mrad in the case of both F-Timing and E-Timing. In the Fig. 69, the difference was 5.8 mrad. The causes of these differences were survey error and ring COD because the horizontal axis of the experimental data was defined on the basis of the survey. In particularly, the absorber angle was defined indirectly by the survey result at the stand attached to the cooling fins. Therefore, the error might occur due to the plural connections of rods. From these results, it can be pronounced that the beam based regulation method is effective in achieving the angle optimization for efficient localization.

Incidentally, a difference between the experimental and simulation results exists in the E-Timing case of Fig. 68. The cause was saturation of the BLM gain. The loss dependence

on the inside absorber angle at the I-4 with two patterns of BLM High Voltage (HV) is shown in Fig. 70. The loss increases along with an increase of the angle. However, when the HV is high, the amount of the increase is smaller than that in the low HV case. Therefore, it can be pronounced that the detected range of the increase of the loss was small as compared with the real one owing to the high HV in the E-Timing case of Fig. 68.

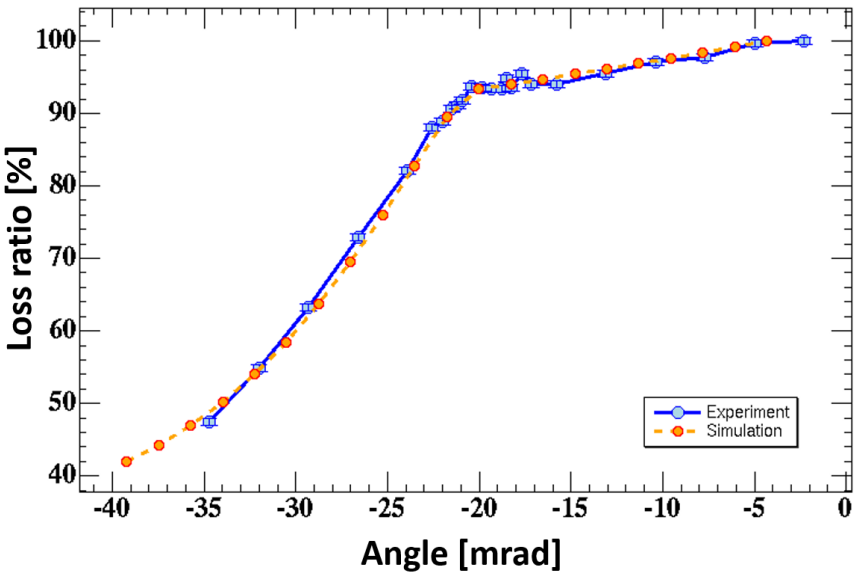

(a) F-Timing

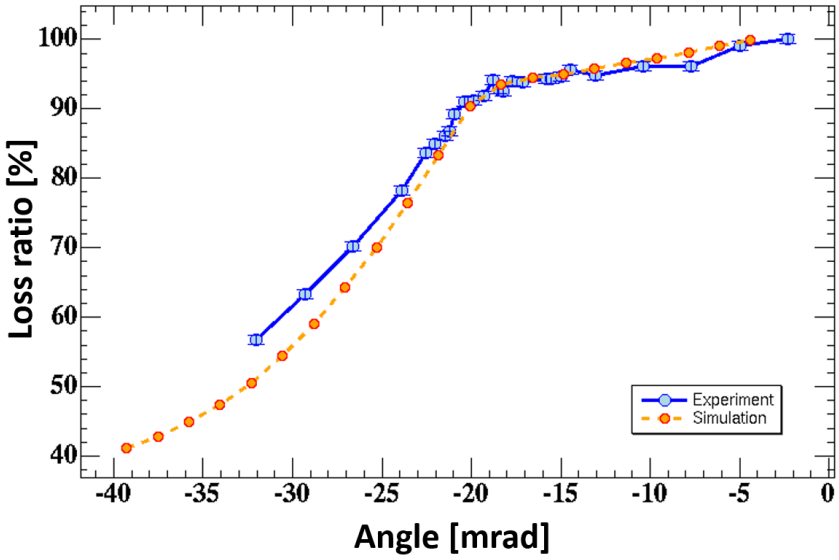

(b) E-Timing

Figure 68: The simulation results of the loss dependence on the inside absorber angle at I-4. The blue plots are experimental data corresponding with Figs. 50 and 51. The orange plots are simulation the results. The vertical axis is normalized by the maximum experimental data point. The horizontal axis indicates the absorber angle.

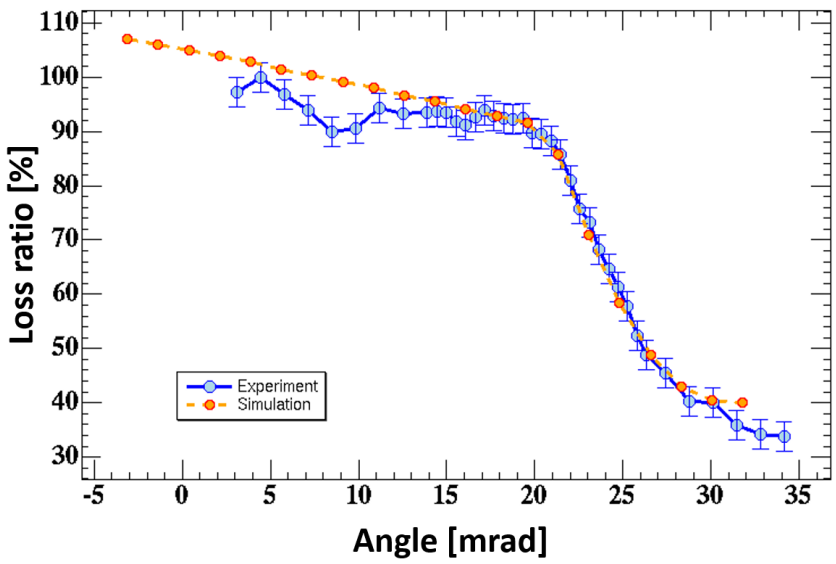

Figure 69: The simulation results of the loss dependence on the outside absorber angle at O-2. The blue plots are experimental data corresponding with Fig. 52. The orange plots are simulation results. The vertical axis is normalized by the maximum experimental data point. The horizontal axis indicates the absorber angle.

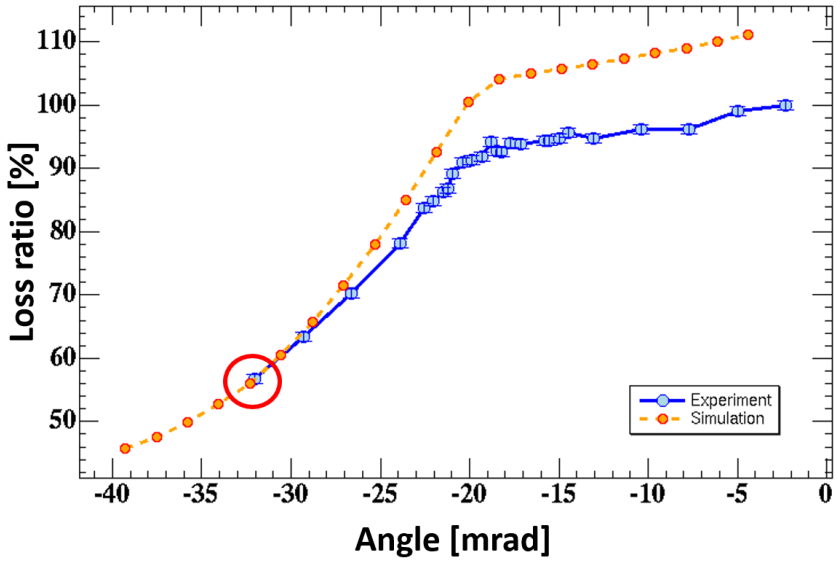

(a) The low BLM HV case. The plots are same as Fig. 68b though the experimental data are shifted to the bottom.

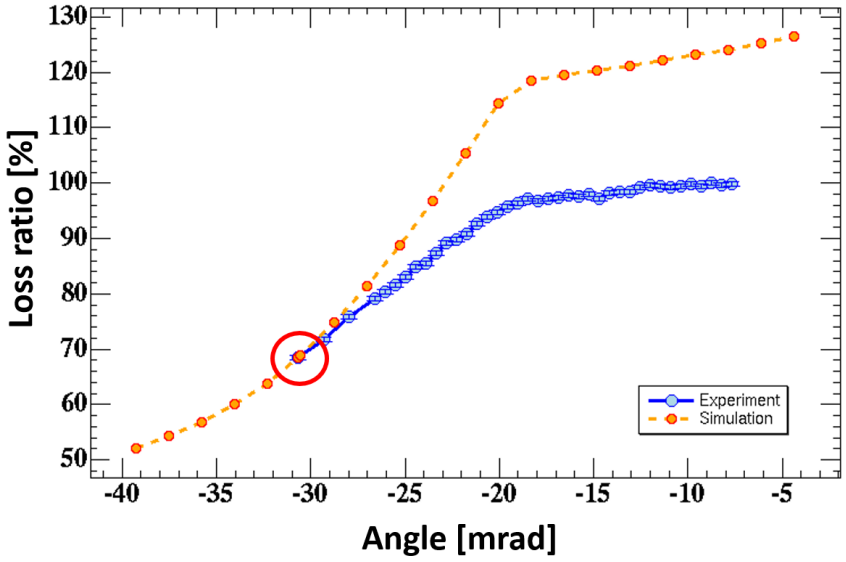

(b) The high BLM HV case. The plots of the simulation results are same as Fig. 68b.

Figure 70: The comparison of the loss dependence on the inside absorber angle at I-4 between simulation and experimental results at E-Timing. The experimental data are shifted to the bottom to be same as the simulation results at the red circle point. The vertical axis is normalized by the maximum experimental data point. The horizontal axis indicates the absorber angle.

6.2.4 User operation results

The time structure of the loss was simulated. The absorber positions were assigned to be the same as in the experimental results. On the other hand, the angles were assigned to be the sum of the experimental results and the difference which described in the above section. Figure 71 and 72 show the time structures of the loss at I-4 and O-2. The experimental and simulation results are placed side by side. The vertical axis indicates the integral of the loss per turn.

In the I-4 case, the time dependent acceptance of the BLM was considered on the basis of the experiment. Specifically, the time structure of the loss was detected in 1/3 Mode in which the injected beams are immediately transported to the 3-NBT Line without circulation or being accelerated. Under this condition, the scattering point at the foil was constant during the injection period, corresponding to 500 μs. In addition, the number of scattered particles was also constant for each bunch. Figure 73 shows the time structures of the loss at I-4 with 1/3 Mode. The loss increases along with the injection time. From the tracking simulation result of SAD, the scattering angle of a particle that collided with the BPM at the foil was approximately 8.5 mrad and changed at most by 0.3 mrad during injection owing to a change in the PB currents. From the scattering result of Fig. 16, it was assumed that the amount of collision particles with the BPM was almost same during the injection period in this case. On the other hand, the absolute collision angle of a particle at the BPM increases along with the injection time and changes as much as 2 mrad. Therefore, the loss increase in Fig. 16 could be considered as the time variation of the acceptance of the BLM owing to the change in the collision angle. This slope were applied to the simulation results of Fig. 71.

In Fig. 71, the results of the simulation show the same trend as the experimental results by adopting the measured injection parameters and BLM acceptance which were described in the previous section. Figure 74 shows each bunch time structures of loss without the absorber insertion. These reflect the longitudinal bunch shape. The results of the simulation also show the same trend as the experimental results. Thus, these results confirm that the conditions of the foil hits, orbit variations, and other effects were reproduced well by the simulation models. On the other hand, in Fig. 72, the simulation result was not in good agreement with the experimental one. The cause of this may be the neglecting of the BLM acceptance.

For the absorber insertion case, the losses only increase at the end of the injection period because of the SB issue in Fig. 71. These losses will be removed by upgrading the SB magnet power supply. Figure 80 shows the simulation results of the time structures of the loss at I-4. In this simulation, the SB current was flat during the injection period and the painting pattern was normal as described in Fig. 37. The absorber positions and angles were the same as in the cases of Fig. 71. Thus, the loss at the end of the injection was removed. Specifically, the loss will become 61 % of that of the present SB decay case.

Regarding the residual dose at the BPM chamber, in order to consider the dependence on the collision points and angles, PHITS calculations were performed for the area around the BPM. In addition, PHITS also considers the irradiation and cooling cycles. Thus, the calculated residual dose of the entire BPM chamber was 1.7×10^4 Bq/cc in the case with absorber. On the other hand, the measured dose was 900 μSv/hr on contact as described in section 5. Therefore, the evaluation of the residual dose for the various power and

injection patterns became possible by using the ratio of the experimentally detected dose to the calculated dose.

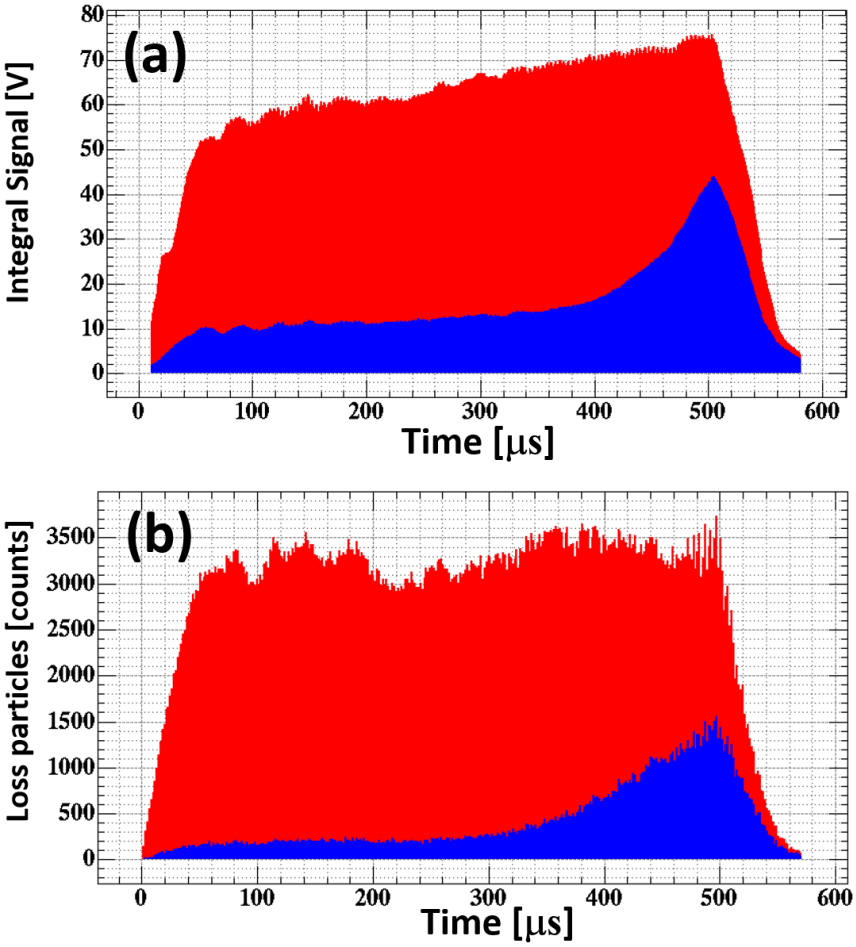

Figure 71: The time structures of the loss at I-4. The figures (a) and (b) indicate the experimental data and simulation results, respectively. The blue and red plots indicate the cases with and without the absorber, respectively.

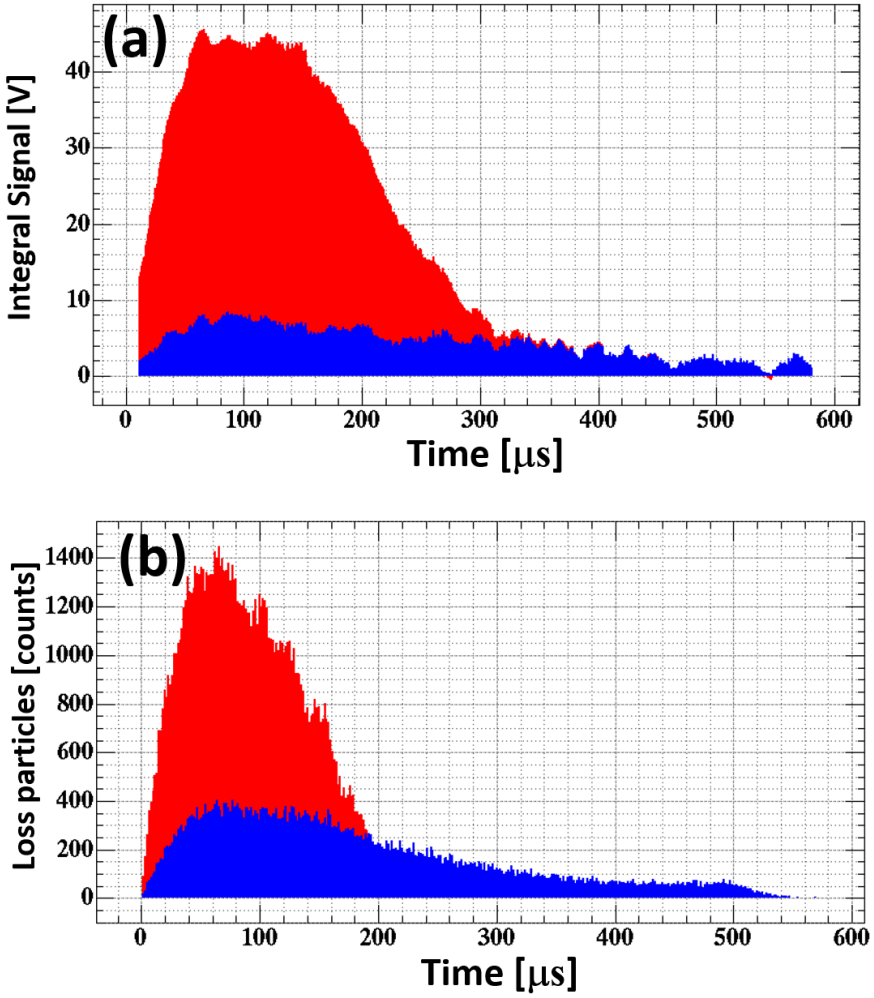

Figure 72: The time structures of the loss at O-2. The figures (a) and (b) indicate the experimental data and simulation results, respectively. The blue and red plots indicate the cases with and without the absorber, respectively.

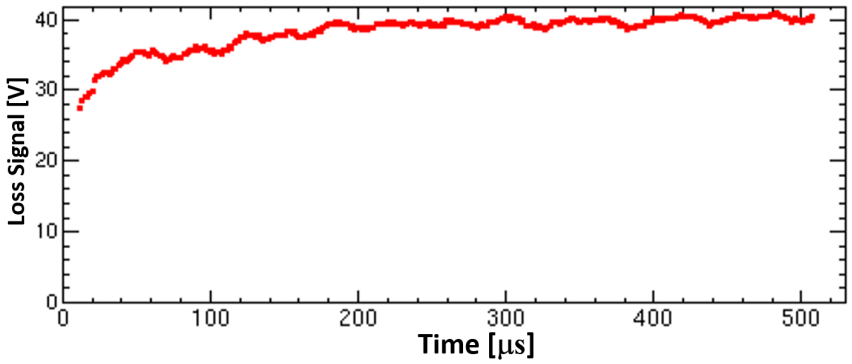

Figure 73: The time structures of the loss at I-4 with the 1/3 Mode.

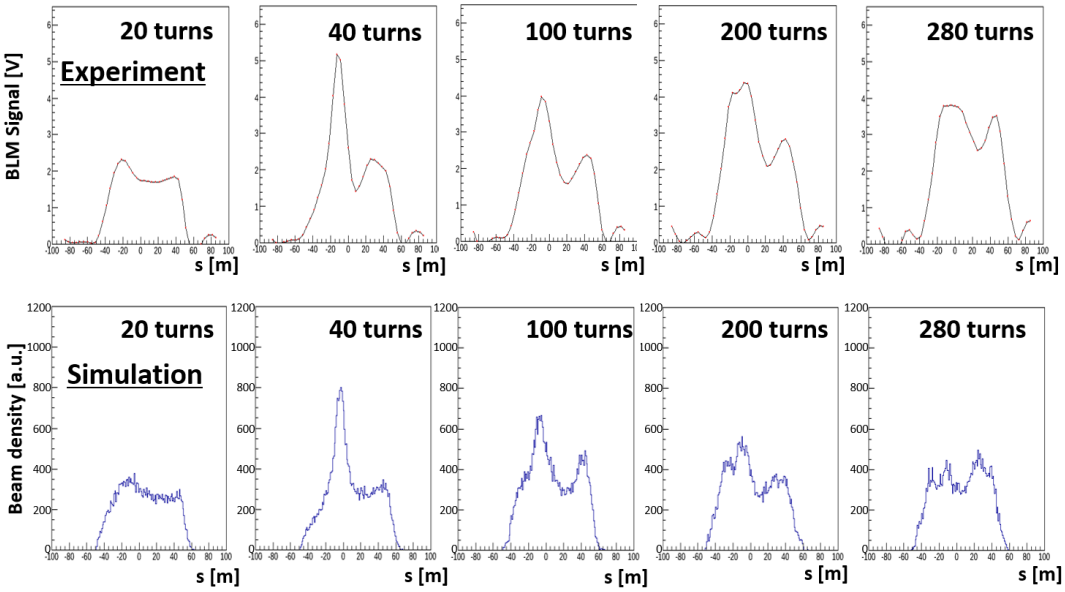

Figure 74: The each bunch time structures of the loss without absorber insertion during injection. The top and bottom figures indicate the experimental and simulation results.

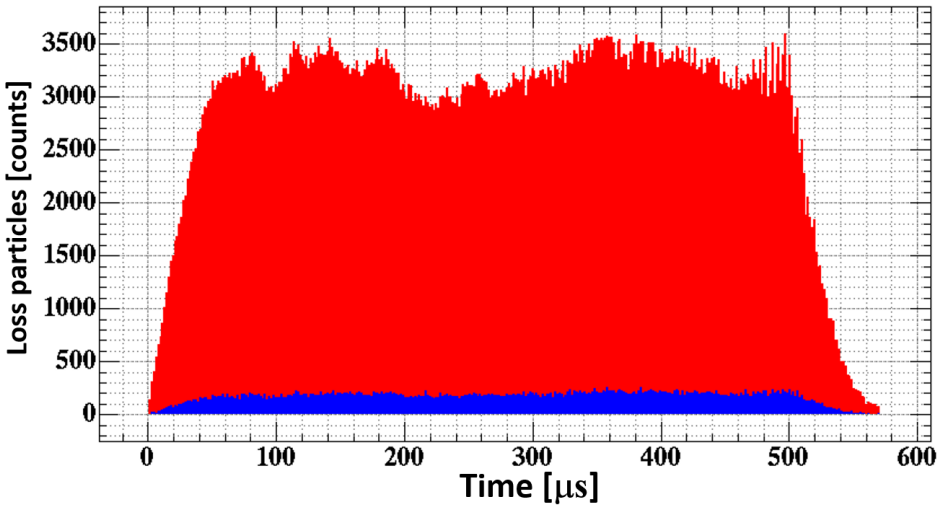

Figure 75: The simulation result of the time structures of the loss at I-4 without SB issure. The blue and red plots indicate the case with and without absorber insertion.

6.3 Localization effect in the 1 MW operation

The realistic simulation model was constructed as described in the above sections. Therefore, the localization effect of the collimator was estimated for the case of 1 MW operation. As shown in a previous section, the simulation result for the loss at the outside of the PB4 did not correspond well with the experiment because the loss was distributed across

a broad area around the PB4, and the acceptance of the BLM could be simulated well. Conversely, the loss at this point is not an issue. Actually, the residual dose at this point was approximately 1/4-1/3 of that at the inside of the BPM after 300 kW operation with absorber insertion. Therefore, the residual dose at the BPM chamber was estimated.

The optimization of the absorber was performed in the simulation using the same scheme as in the experiment. The beam conditions were defined as follows. The injection beam parameter was the design pattern shown in Table. 4. The painting pattern was the design 100 π Correlated pattern shown in Fig 61. The SB current was flat during the injection period. The horizontal foil edge was 10 mm from the injection beam center and the vertical size was 20 mm, corresponding to the present operation parameter. The number of foil hit simulated by SIMPSONS is shown in Fig. 76. As shown, the hit rate gradually increased along with the time because of the beam emittance growth due to the space-charge force. The number of foil hit per particle was 25.1. The loss dependence on the inside absorber position at I-4 is shown in Fig. 77. In this figures, two time ranges were adopted as the integral times of the loss. One was the range between 0 s and 100 μs which correspond to F-Timing. Another was the range between 400 μs and 500 μs, which corresponds to E-Timing. The ranges were called F-Range and E-Range, respectively. As introduced in the section 4.2, large insertion distance was required at the start of the injection period for the inside absorber. From these results, the inside absorber position was decided to be set to -63 mm.

Next, the angle optimization was performed using the LMM. The inside absorber positions was set to -72 mm. The F-Range was adopted for the inside optimization as the integral time of the loss. The loss dependence on the inside absorber angle at I-4 is shown in Fig. 78. The optimized angle was decided from the crossing point of the two linear lines that were fit to the data points as indicated in the figure. Specifically, the inside absorber angle was decided to be set to -17.5 mrad.

Finally, the time structure of the loss was simulated using the selected absorber positions and angles. The results are shown in Fig. 79. The outside absorber position and angle were also decided to be set to 77 mm and 14.3 mrad in the same manner as the inside case. As shown, the loss was suppressed. Thus, optimization of absorber was achieved. In addition, from the results of the PHITS simulation, the calculated residual dose of the entire BPM chamber was 6.9×10^4 Bq/cc after a 4 hour cooling period following one week long 1 MW operation. By applying the ratio of the calculated result to the detected residual dose introduced in section 6.2.4, the residual dose was estimated to be 3.6 mSv/h at the BPM on contact. Around the BPM, it was confirmed from detection results that the residual dose at a distance of one foot from the BPM, corresponding to approximately 30 cm, becomes 1/3-1/4 of that detected on contact. Therefore, the residual dose was estimated to be 0.91-1.2 mSv/h around the BPM. As a result, it was confirmed that the residual dose will become of 1 mSv/h order for 1 MW operation by the new collimator.

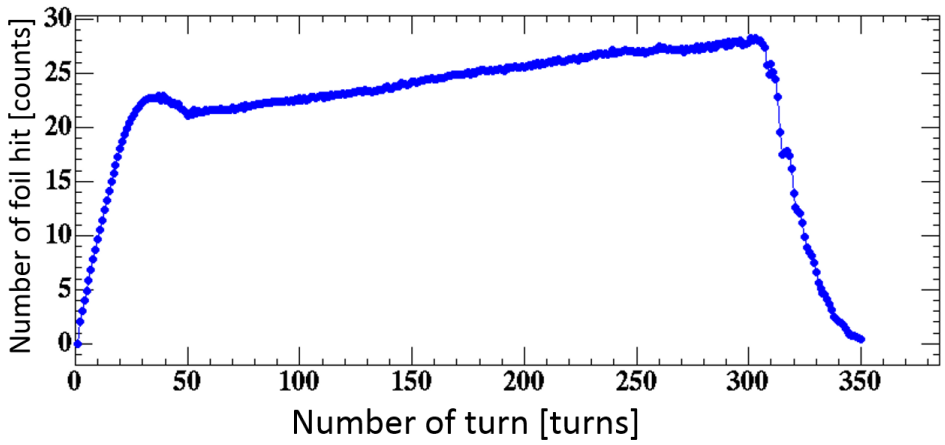

Figure 76: The number of foil hit simulated by SIMPSONS.

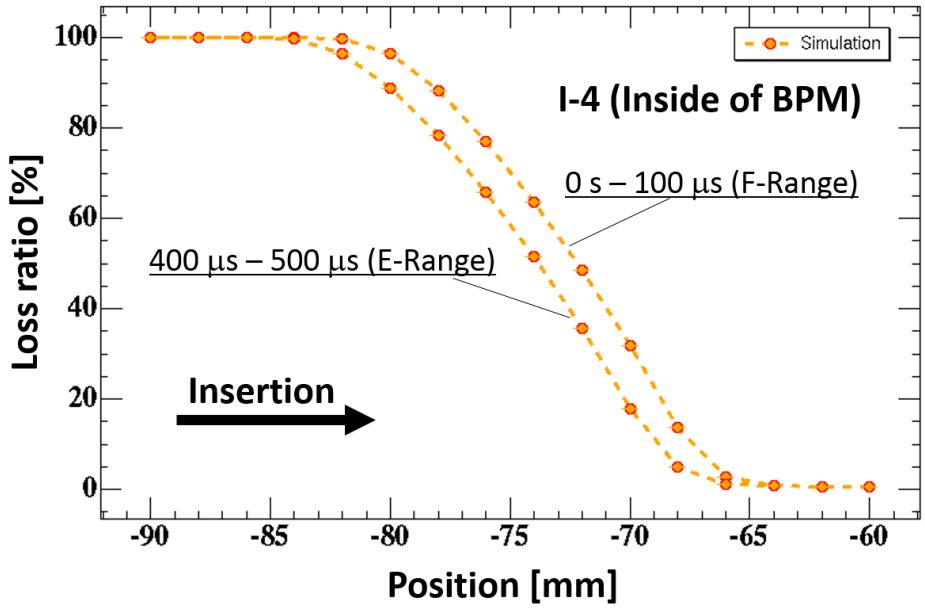

Figure 77: The loss dependence on the inside absorber position at I-4. The right and left slopes indicate the case of the F-Range and E-Range, respectively. The vertical axis is normalized by the maximum data point. The horizontal axis indicates the absorber position.

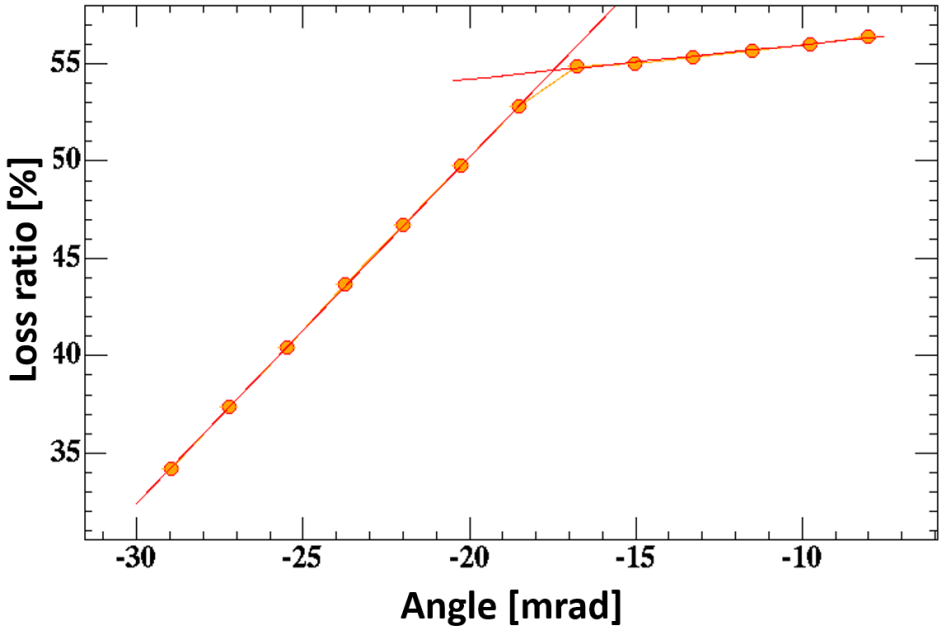

Figure 78: The loss dependence on the inside absorber angle at I-4. The integral time of the loss is F-Range. The red lines fit to data points. The vertical axis is normalized by the maximum data point. The horizontal axis indicates the absorber angle.

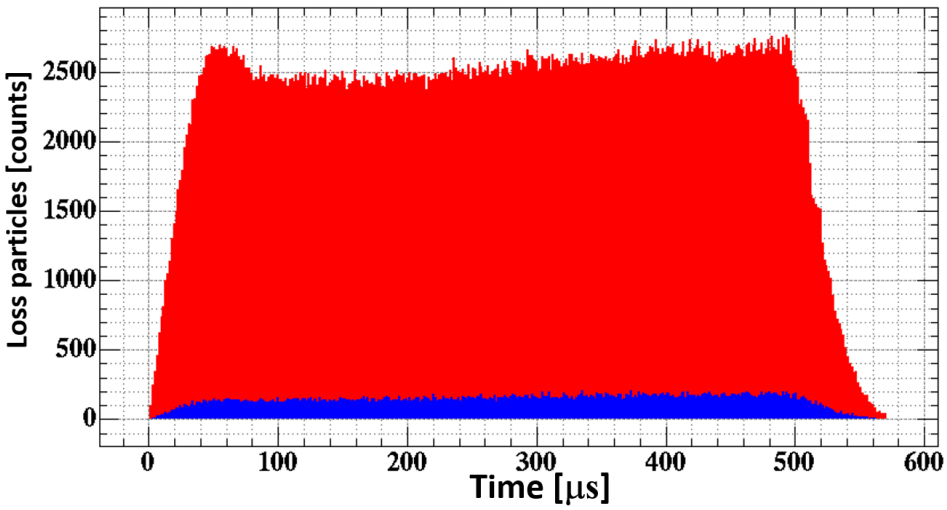

Figure 79: The time structures of the loss at I-4. The blue and red plots indicate the case with and without absorber, respectively.

6.4 Discussion for further beam loss suppression

6.4.1 The present remaining loss

The results of Fig. 71 show that the loss remained during the start of injection period when the absorber insertion distance was enough to remove the loss both experiment and

simulation. Although the discussion in the previous section confirmed that this remaining loss will not become an issue for the residual dose in the 1 MW operation, the source was identified by the simulation.

For the simulation result of the loss at I-4 shown in Fig. 80, the losses from the outside absorber and from others are shown in Fig. 80 separately. The loss source from the outside absorber was defined by the scattered and created protons by collision with the absorber in this simulation. Thus, the losses from the outside absorber were 21 % of whole losses. In other word, it was confirmed that a lot of protons leaked from around the inside absorber.

In the GEANT4 simulation model explained in section 4.1, the longitudinal length of the absorber was defined as 400 mm which was twice the original size. In addition, the vertical size of absorber was defined as 300 mm which was three times the original size. Figure 81 shows the loss dependence on the absorber geometry at I-4. In this simulation, the conditions corresponded to those of Fig. 80, except for the absorber size. Thus, as compared with the original geometry, the loss barely decreased even if the length was extended. Therefore, it was confirmed that the absorber had enough length to absorb the scattered 400 MeV proton. On the other hand, the loss became approximately 24 % compared with the original geometry when the vertical size was defined as 300 mm. Therefore, it became clear that the remaining loss source was particles passing through from the top and bottom of the absorber.

At present, the vertical size of absorber was decided to be 100 mm in order to keep space for assembly in the absorber chamber. However, reducing the loss further is possible through the vertical extension of the absorber.

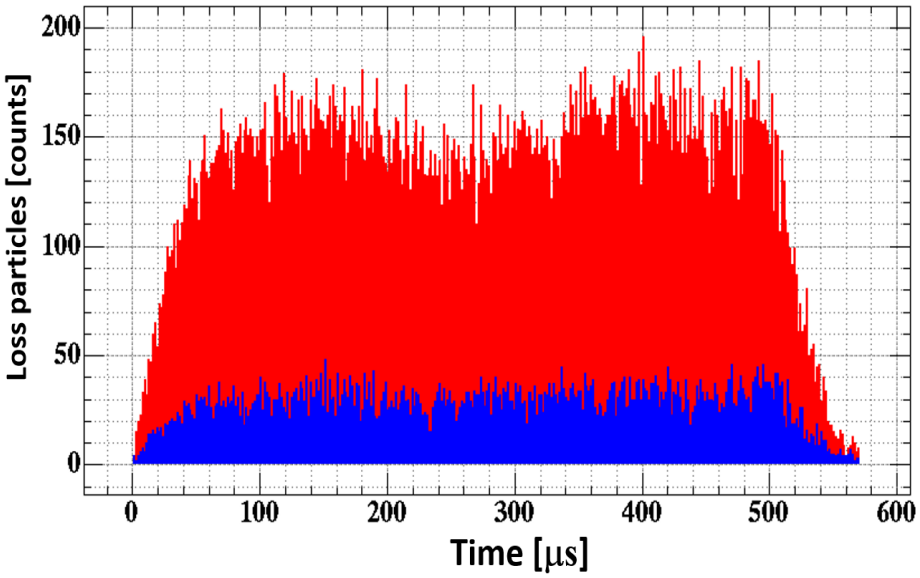

Figure 80: The losses from the outside absorber and from others at I-4. The blue plots indicate the loss from the outside absorber. The red plots indicate the loss from others.

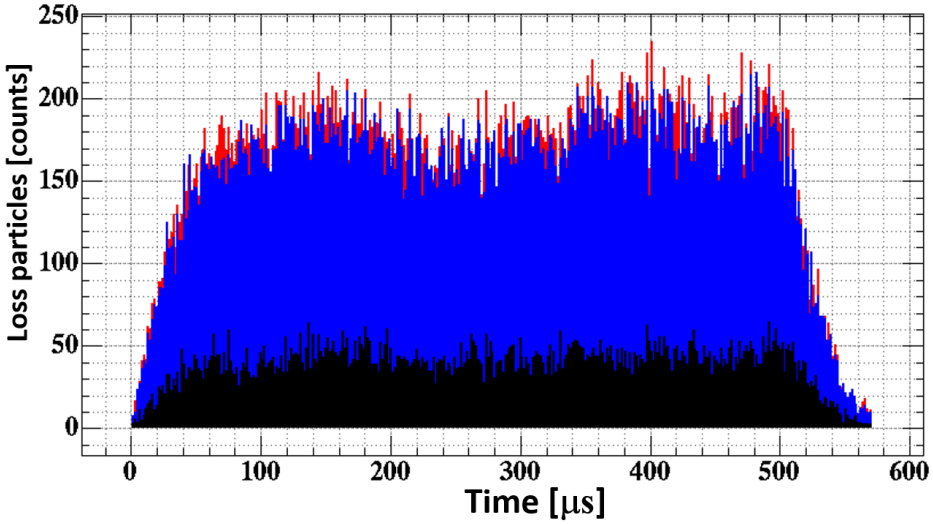

Figure 81: The loss dependence on the absorber geometry at I-4. The red plots indicate the loss with normal geometry. The blue plots indicate the loss with extended geometry. The black plots indicate the loss with large vertical size geometry.

6.4.2 The reduction method of the foil hitting probability

To reduce the large-angle scattering beam loss, reduction of the number of foil hits is most effective. Therefore, some methods to achieve this will be discussed in this section.

The most fundamental method is reducing the injection beam size because the foil area size depends on it. If the foil area size is sufficiently small as compared with the circulating beam size, the foil hitting probability can be suppressed. Figure 82 shows a schematic drawing of the injection beam and foil position. As shown, the vertical foil size can be reduced to the size of the injection beam. The horizontal foil edge position is also determined by the size of the injection beam. In the RCS, 15 foils which have various vertical sizes are prepared in the vacuum chamber connected to the injection point before the experimental beam tuning. By experimentally measuring the leakage of the injection beam from the foil, the vertical foil size and horizontal foil edge position are decided. Although reducing the injection beam size is effective for the reduction of the foil hitting probability, it is not a realistic method because the redesign of the L-3BT lattice and the replacement of the magnets would be required. Therefore, another method is discussed below.

As explained in section 2.4, the painting injection method can also reduce the number of foil hits. In particular, the Anti-Correlated painting can reduce this more effectively. Figure 83 and 84 show the number of foil hit in the case of Correlated and Anti-Correlated painting. The number of foil hits par particle is also shown in Fig. 83 and 84. This is the integral value of the number of foil hit divided by the number of stored particles during the injection period. In this simulation, the injection beam size and horizontal foil edge positions were the same as those shown in Fig. 82. The vertical foil sizes were 20 mm and 100 mm for Figs. 83 and 84, respectively. The space-charge effect was excluded. As shown in Fig. 83, the time structures of the number of foil hits were different from each other.

The number was large at the start of the injection period in the Correlated painting case. However, it was large at the end in the Anti-Correlated painting case. On the other hand, as shown in Fig. 84, both cases were almost the same when the vertical foil size was large enough to cover entire vertical phase-space area of the painting. From these results, it can be deduced that passing though the top and bottom of the foil caused this time structure difference. The particles having large vertical amplitude are injected and passed through at the start or end of the injection period in the Anti-Correlated or Correlated painting case, respectively. From the Fig. 83, the number of foil hit par particle became smaller when the Anti-Correlated painting was adopted. It was approximately 68.7 % compared with the case of Correlated painting. Because the particles can escape to vertical direction at the start of the injection period when most of the circulating beam area is covered with the foil on the horizontal phase-space, the number of foil hit become smaller in the case of Anti-Correlated painting.

In addition, the extension of the painting area can also reduce the number of foil hits effectively because the circulating beam get away from the foil early in the horizontal plane. Figure 85 shows the dependence of the number of foil hits on the paint area size. The number of foil hit per particle is also shown in Fig. 85. As shown, when 200-π Anti-Correlated painting is adopted, the number of foil hit can be reduced to 25 % compared with the case of the 100-π Correlated painting.

The selection of the Anti-Correlated painting and the extension of the painting area have an advantage for reduction of the foil hitting probability. The extension of the painting area also has an advantage for the mitigation of the space-charge force. However, as of 2014 in the RCS, the 100-π Correlated painting has been adopted because the beam loss is minimal as compared with that in any other pattern. The beam loss source in the over 100 π painting case is the lattice imperfection. This disturbs the symmetry of the RCS lattice. Then, the separatrix of the ring, which is the phase-space area where particles can remain stable, becomes small and the beam loss occurs in the over 100 π painting case. In particular, it was known in the RCS that the vertical edge focus by the Shift Bump Magnet causes the disorder of symmetry and the shrinking of the separatrix during the injection period. The cause of the larger loss in the Anti-Correlated painting case is also the lattice imperfection by the Shift Bump Magnet. In this painting pattern, the particles that have large horizontal amplitudes hit the foil repeatedly at the end of the injection period when the beam current is at a maximum. Therefore, these particles tend to move away from the shrunken separatrix because an additional angle was added by the foil scattering and space-charge force. Thus, in order to achieve over 100-π painting, the disordered symmetry will be compensated by the new Trim-Q magnet during the injection period [38]. In addition, to reduce the number of particles leaking from the selected painting area, the reduction of the injection beam tail is also desirable.

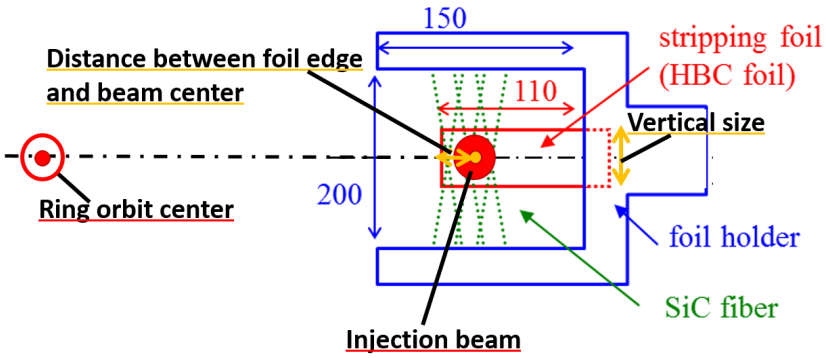

Figure 82: A schematic view of the injection beam and foil position.

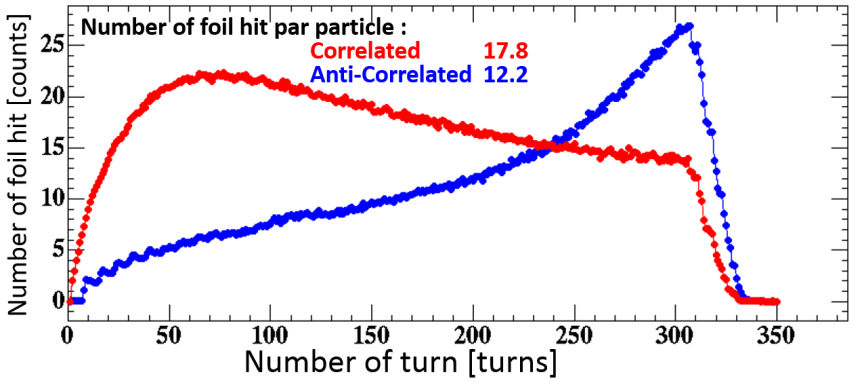

Figure 83: The number of foil hits for two painting patterns. The red and blue plots indicate the results of the Correlated and Anti-Correlated painting, respectively. The painting area is 100 π mm mrad.

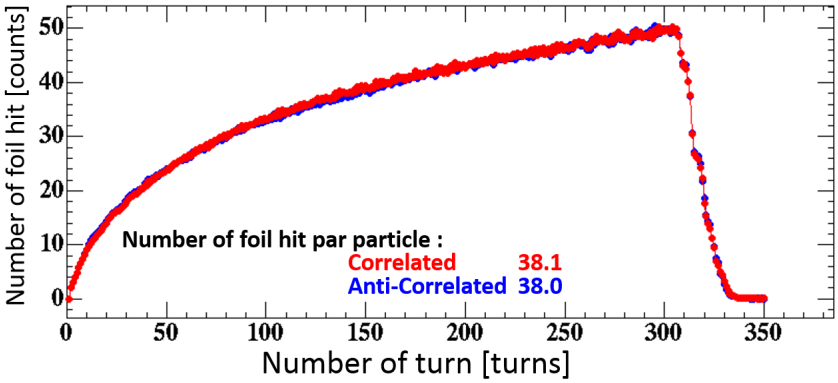

Figure 84: The number of foil hist for two painting patterns with a large vertical size foil. The red and blue plots indicate the results of the Correlated and Anti-Correlated painting, respectively. The painting area is 100 π mm mrad.

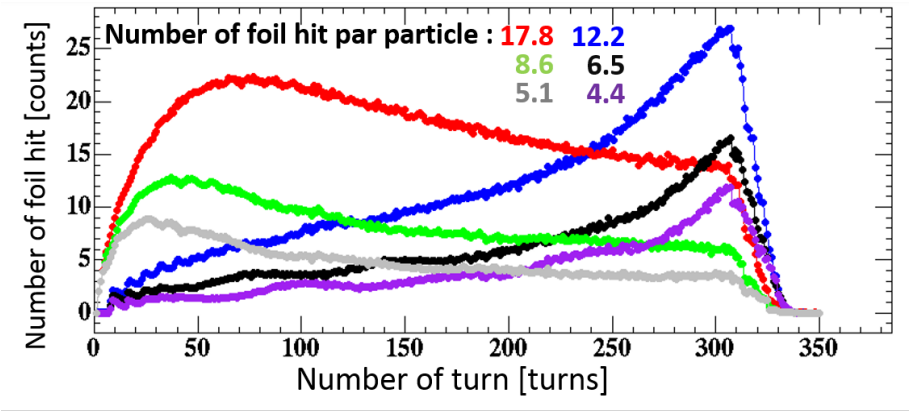

Figure 85: The dependence of the number of foil hits on the paint area size. The red, green and gray plots indicate the results of the 100, 150 and 200 π mm mrad Correlated painting, respectively. The blue, black and purple plots indicate the results of the 100, 150 and 200 π mm mrad Anti-Correlated painting, respectively.

6.4.3 New painting pattern for the foil hitting probability reduction

The reduction in the foil hitting probability would be enhanced if particles avoid the foil in the vertical direction during the painting injection scheme. Accordingly, if the ratio of particles that have a large vertical amplitude are increased during the injection, the number of foil hit may decrease. In order to satisfy this condition, the time variation of the injection beam position and angle should be modified for the painting injection scheme. Specifically, the vertical angle of the injection beam should be increased rapidly, more than in the present pattern in the case of Correlated painting. For the case of Anti-Correlated painting, the state of the injection start when the vertical angle of the injection beam is large should be keep as long as possible. Therefore, a new time function of the painting was defined as follows.

$$\begin{aligned} x\,and\,x' &\propto \sqrt[3]{\frac{t}{500\,\mu s}},\ y' \propto \sqrt[3]{\frac{t}{500\,\mu s}} \quad \text{for new Correlated Painting} \\ x\,and\,x' &\propto \sqrt[3]{\frac{t}{500\,\mu s}},\ y' \propto \sqrt[3]{1-\frac{t}{500\,\mu s}} \quad \text{for new Anti-Correlated Painting} \end{aligned} \tag{6}$$

Figure 86 shows the time variations of the injection beam positon and angle. In the new function, the injection beam is moved in proportion to the cubic root of the time. The time function of the horizontal beam positon and angle are also modified in order to keep the symmetry of the beam distribution. The new painting patterns are called 3-Corr Painting and 3-Anti Painting, respectively.

First, the reduction effect of the foil hitting probability is discussed. Figure 87 shows the dependence of the foil hit rate on the painting pattern. In this simulation, the painting area size was 100 π and the beam intensity was 1 MW. The lattice parameters, such as the tune or RF pattern, were the same as in the present user operation case. As a result, when the 3-Corr Painting was adopted, the number of foil hits became smaller compared with that in the Correlated painting case as expected. The reduction effect was

approximately 22 %. Similarly, when the 3-Anti Painting was adopted, it also became smaller compared with the Anti-Correlated painting case as expected. The reduction effect was approximately 12 %. In this way, it was confirmed that the new time function was effective for the reduction of the foil hitting probability. In other words, if the new time function was adopted, it is possible to reduce the large-angle foil scattering beam loss more than ever.

Next, the fluctuation of normal beam loss using the new time functions will be discussed. The beam loss does not mean the large-angle foil scattering beam loss, but the entire RCS beam loss localized at the ring collimator. Figure 103 shows the time structures of the beam loss which are dependent on the beam power. The simulation results are consistent with the experimental results. In the RCS, the beam loss is minimized at present by beam study and tuning. The source of the residual beam loss is almost the particles spilled from the separatrix by the foil scattering during the injection period up to the present 500 kW operation. With the additional simulation, it is expected that the beam loss can be minimized for 1 MW operation. Therefore, the beam loss occurrence was simulated for the case of Correlated, Anti-Correlated, 3-Corr and 3-Anti painting during the injection period with 1 MW beam power. Figure 88 shows the beam loss dependence on the painting patterns. As shown, the loss increased along with time. When the Anti-Correlated painting was adopted, a larger loss occurred as compared with that for the Correlated painting case, as explained in the previous section. The ratio of the loss was 1.14. Similarly, when 3-Anti painting was adopted, a larger loss occurred as compared with that for the Correlated painting case. The ratio of the loss was 1.60. On the other hand, when 3-Corr painting was adopted, the loss was suppressed to 80 % compared with the Correlated painting case because the particles had their large amplitudes increased.

The results of the above two discussions are arranged in Table 5. As a result, it was confirmed that both the large-angle scattering beam loss and the normal beam loss can be reduced by adopting the 3-Corr painting. If reducing the large-angle scattering beam loss as possible is necessary for over 1 MW operation in the future, the 3-Anti painting can also be used because the normal beam loss is localized sufficiently and the amount of the loss is sufficiently small as compared with the ring collimator limit, which is 4 kW.

Finally, the formed beam distributions of each painting pattern are discussed. As explained in section 2.4, the time function of the paint should be defined as proportional to the square root in order to arrange the injection beam uniformly on the phase-space. Therefore, it is expected that the distribution is not uniform in the 3-Corr and 3-Anti painting cases. However, it was suggested that the time function, which is proportion to the cubic root of time, contributes to form a uniform distribution rather than the square root function in the high current condition. The explanation for this is as follows [39].

When the space-charge force is strong, transverse motion including the space-charge force satisfies the envelope equation regardless of the distribution approximately as follows [40]:

$$\begin{aligned} \tilde{x} &= \sqrt{< x^2 >} \\ \varepsilon_{rms} &= \sqrt{< x^2 >< p_x^2 > - < x p_x >^2} \\ \frac{d\tilde{x}'}{ds} + k(s)\tilde{x} &= \frac{\varepsilon_x^2}{\tilde{x}^3} + k_{sc}\frac{1}{\tilde{x}+\tilde{y}} \end{aligned} \tag{7}$$

where $k(s)$ is the convergence force of the ring. k_{sc} is the space-charge force. This equation indicates that the beta function corresponding to the beam width is changed by the space-charge force. Through analysis of this differential equation, the modulated beta function is obtained [41]. The calculation results of the beta function after corr 100 π painting injection is shown in Fig. 89. The result shows that the horizontal beta function increase at the injection point. The painting area ellipse in the horizontal phase space at the injection point is shown in Fig. 90. From these results, it became clear that the horizontal beta function deformed and the painting area ellipse became slender for high currents. Therefore, it is considered that the injected particles moved in the phase space as shown in Fig. 90 and they do not spread as expected in the Correlated and Anti-Correlated painting cases. Figure 91 shows the simulation results of the ε_x-ε_y plane distributions after the painting injection for each of the painting patterns. The distribution is uniform in the phase-space when the distributions of the ε_x and ε_y are uniform. As expected, in the Anti-Correlated painting cases, particles did not spread and the beam density was large at the center of the beam though it should satisfy the relation in Eq. 3. In the Correlated painting cases, the beam density was larger. On the other hand, in the 3-Anti painting cases, the distribution was more uniform as compared with that in the two explained cases. In addition, the belt structure satisfying the relation of Eq. 3 appeared on the ε_x-ε_y plane. In the 3-Corr painting cases, the particles spread to the same level as the Anti-Correlated painting case. The reason for these results is that particles having a large emittance increase by arranging the injection beam outside faster at the beginning of the injection in the horizontal plane. In addition, the suppression of the beta function deformation by increasing the RMS emittance of the stored beam affects these results. Figure 92 shows the horizontal and vertical distributions after the injection period. In the 3-Corr painting cases, the distribution was almost the same as for the case of the Correlated painting. In the 3-Anti painting cases, the peak of the distribution was suppressed. These result confirmed that the new time functions of the paint did not disturb the uniformity of the distributions. In addition, it became clear that the new time functions affect to form the uniform distribution under high current condition.

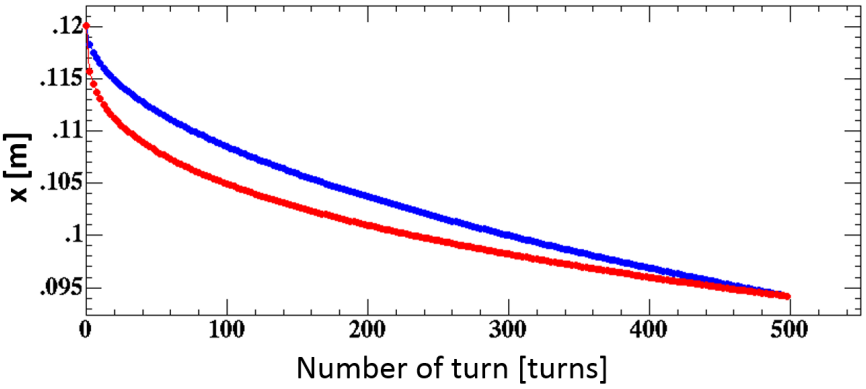

Figure 86: The time variations of the ring orbit. The blue and red plots indicate the Correlate and 3-Corr Painting, respectively. The painting area size is 100 π mm mrad.

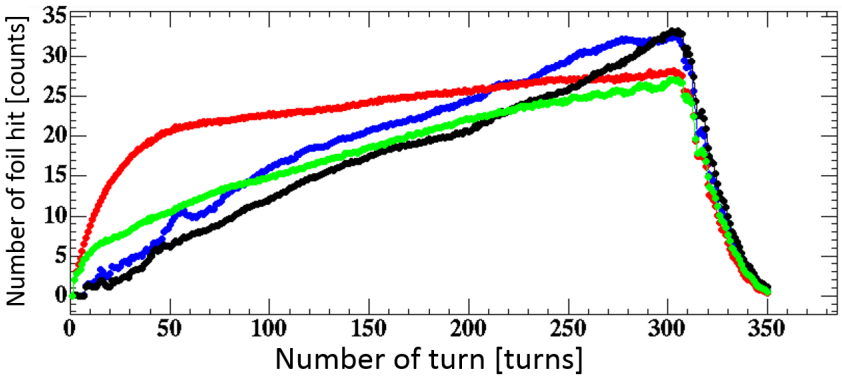

Figure 87: The dependence of the number of foil hits on the painting patterns. The red, green, blue and black plots indicate the results of the Correlated, 3-Corr, Anti-Correlated, and 3-Anti painting patterns, respectively.

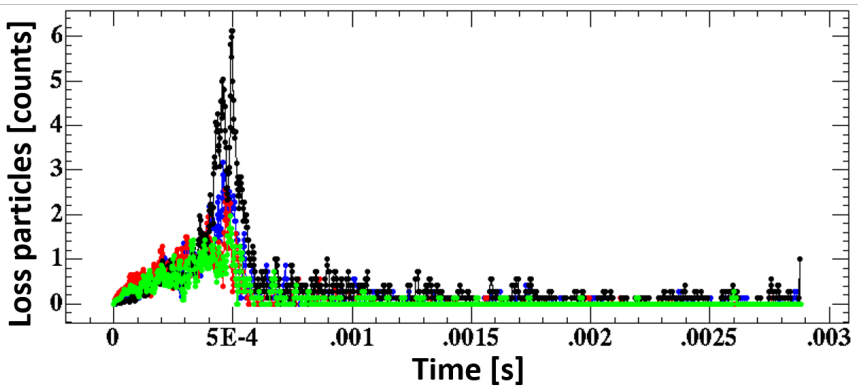

Figure 88: The beam loss dependence on the painting patterns. The red, green, blue and black plots indicate the results of the Correlated, 3-Corr, Anti-Correlated, and 3-Anti painting, respectively. The painting area size is 100 π mm mrad.

Table 5: The comparison between 4 painting patterns.

	Number of foil hit / particle	Beam Loss at 1 MW (W)
Correlated	24.7	92.9
Anti-Correlated	21.3	119.5
3-Corr	19.5	73.1
3-Anti	18.8	195.0

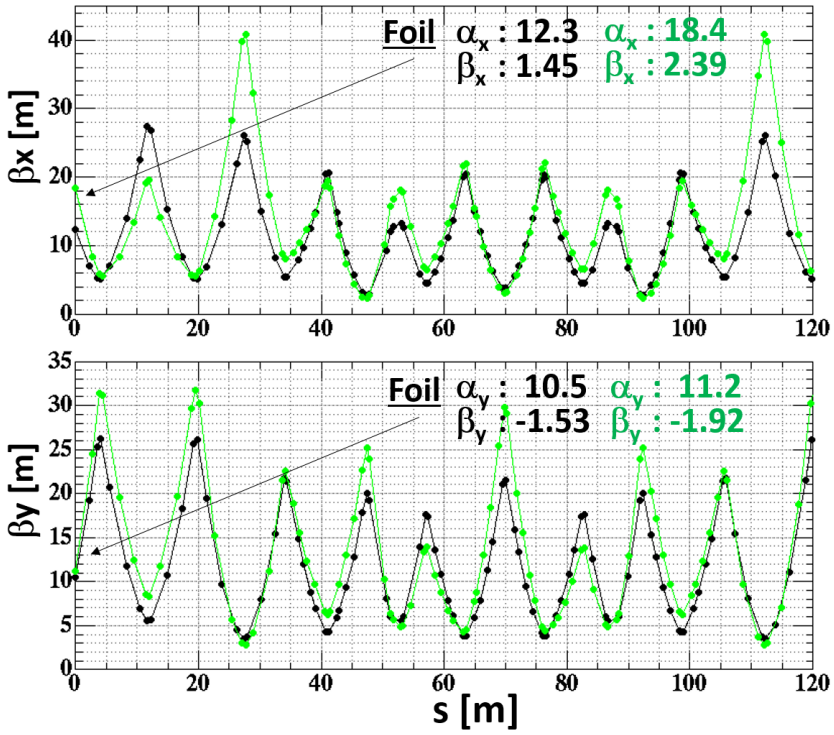

Figure 89: The beta functions after 100 π Correlated painting injection. The black and green plots indicate the results of the 0 current and 1 MW equivalent current case, respectively.

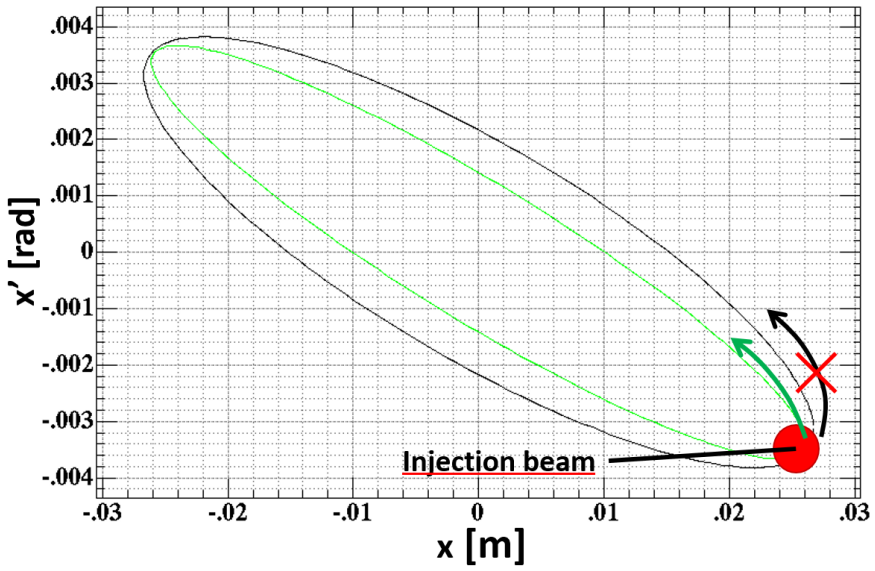

Figure 90: The painting area ellipse in the horizontal phase-space at the injection point. The black and green plots indicate the results of the 0 current and 1 MW equivalent current case, respectively.

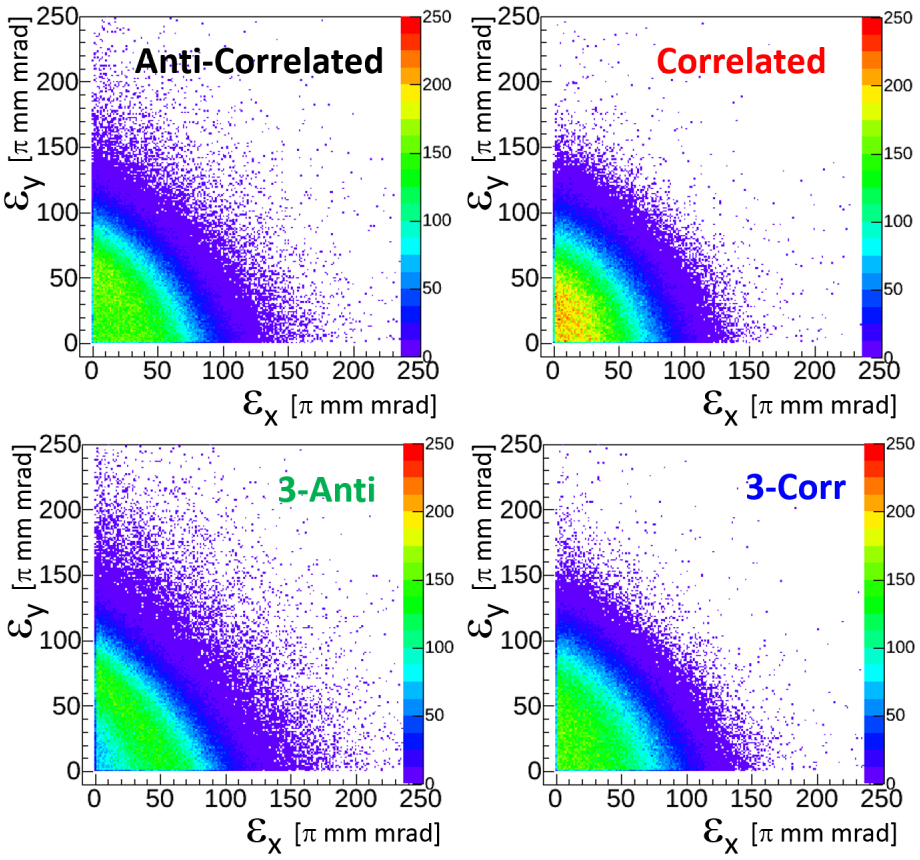

(a) ε_x-ε_y plane

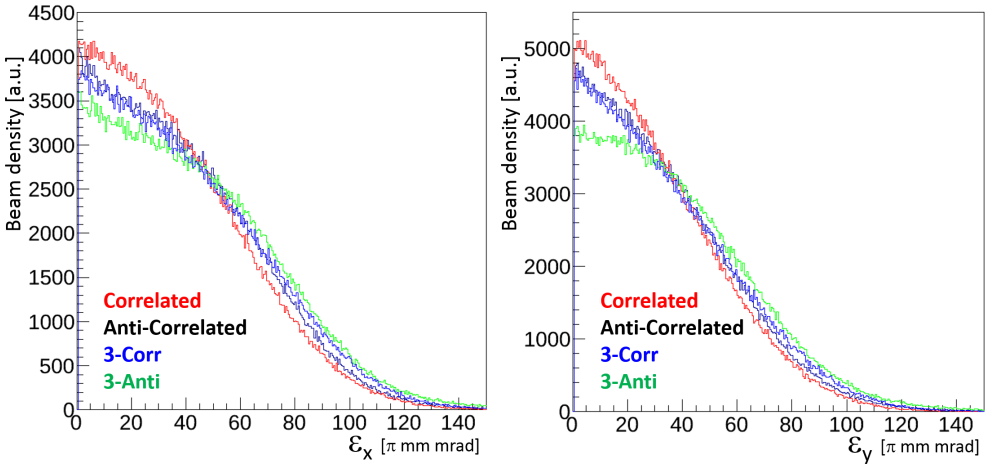

(b) ε_x and ε_y distributions

Figure 91: The ε_x and ε_y distributions dependence on the painting patterns.

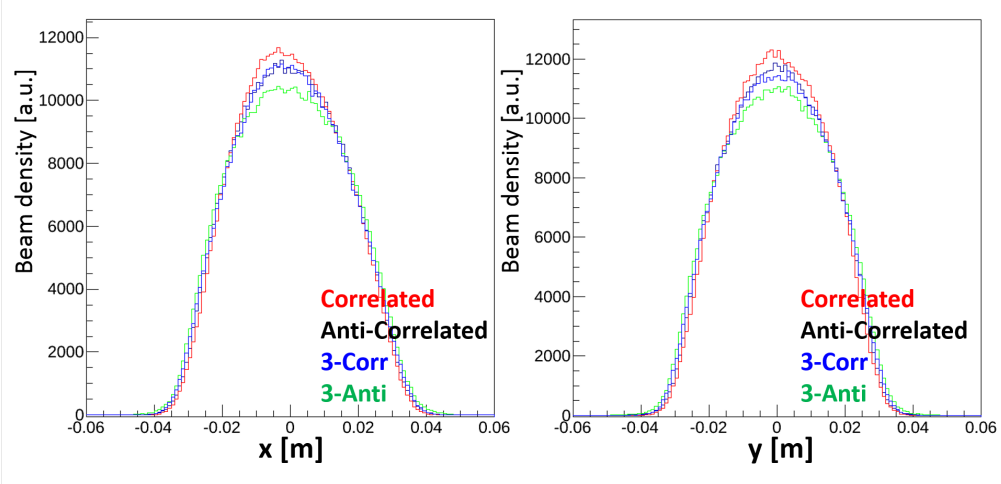

Figure 92: The horizontal and vertical distributions at the foil after painting injection. The red, black, blue and green plots indicate the results of the Correlated, Anti-Correlated, 3-Corr, and 3-Anti painting, respectively.

6.4.4 The loss dependence on the foil thickness around downstream area

In order to solve the issue of the large-angle foil scattering beam loss, the localization method and the reduction method of the foil hitting probability were discussed in this thesis. In addition, it can be thought that the reduction of the foil thickness may be effective for the reduction of that loss. However, the charge-exchange efficiency decrease when the foil is thinned down. Although the H^- and H^0 which are not converted into proton are led to the H^0 dump, the excited H^0(n) causes uncontrollable beam loss when the H^0(n) is broken down into H^+ by the peripheral magnetic field before reaching the 2^{nd} foil. In this section, the loss dependence on the foil thickness around downstream area of the injection will be discussed based on the experimental results of the RCS.

In the RCS, the H^0(n) can be broken down by the magnetic field of SB3 and SB4. The tracking simulation of the decayed H^0 is shown in Fig. 93. The injection point was same as that of 100 π painting case. The PB was off corresponding to the state at end of the injection. As shown, the decayed particles can be lost at the branch and the outside of the PB4.

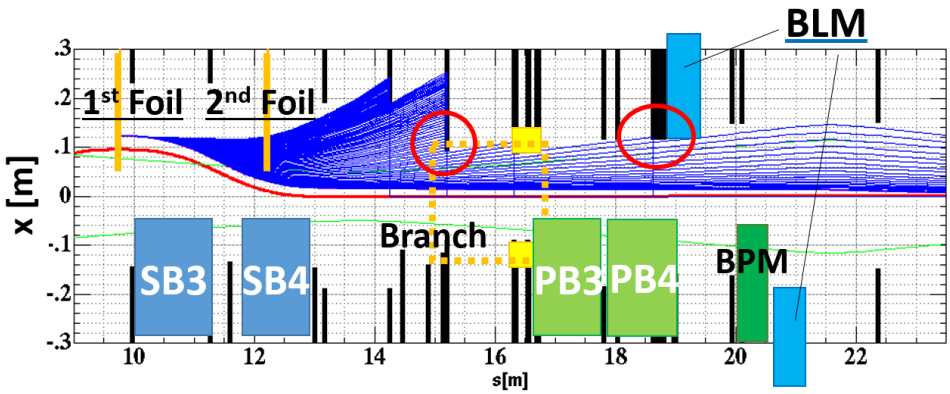

Figure 93: The tracking simulation of the decayed H^0 in the horizontal plane. The particles which was broken down at arbitrary position between 1^{st} and 2^{nd} foil were tracked. The blue lines indicate the particle tracks. The black bars indicate the apertures.

In the RCS, the $H^0(6)$ and $H^0(7)$ break down between the 1^{st} and 2^{nd} foil as shown in Fig. 11. By using the lifetime result in Fig. 11 and the magnetic field distribution of the SB, the decay points of $H^0(6)$ and $H^0(7)$ were calculated. The field distribution of the SB and the calculated decay points are shown in Fig. 94. In addition, the calculated loss points are shown in Fig. 95. As shown, all of $H^0(6)$ and $H^0(7)$ break down before reaching the 2^{nd} foil. However, all of decayed $H^0(7)$ are led to the ring collimator. Because the $H^0(7)$ break down near the 1^{st} foil, decayed particles are not much separated from the closed orbit. The only $H^0(6)$ causes the beam loss at downstream of the injection.

From the results of Fig. 95, the loss dependence on the foil thickness at the outside of the PB4 was detected. In this experiment, the loss at the inside of the BPM was also detected. The arrangement of the BLM is indicated in Fig. 93. During this experiment, two foils which thickness were 200 μg/cm^2 and 300 μg/cm^2 were applied. The schematic drawings of the foils are shown in Fig. 96. The foils whose thickness were 200 μg/cm^2 and 300 μg/cm^2 were named Thin foil and Thick foil, respectively. It was calculated that the power of beams led to H0 dump were 5.27 kW and 0.83 kW at 1 MW output power when the thin foil and the thick foil were applied, respectively.

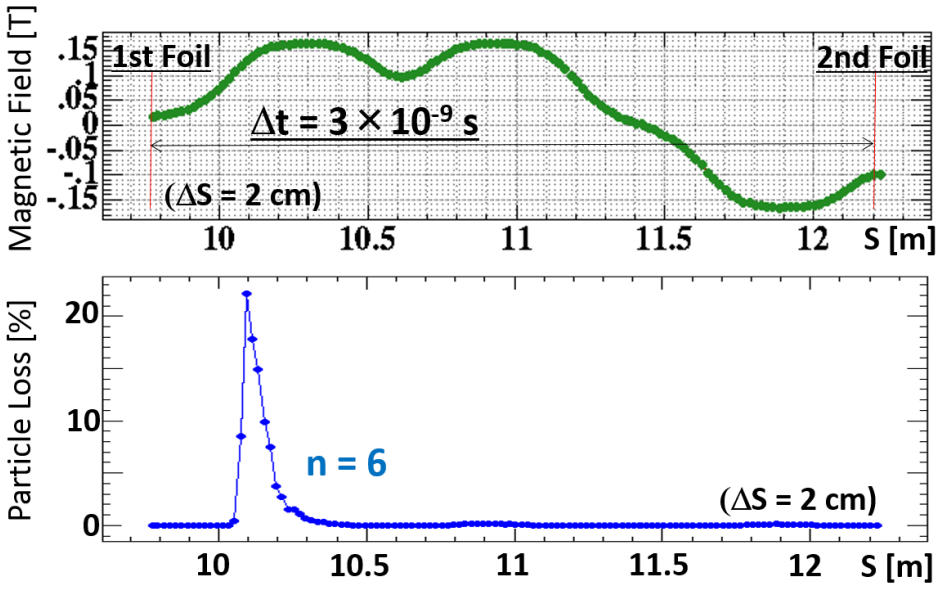

(a) The case of $H^0(6)$

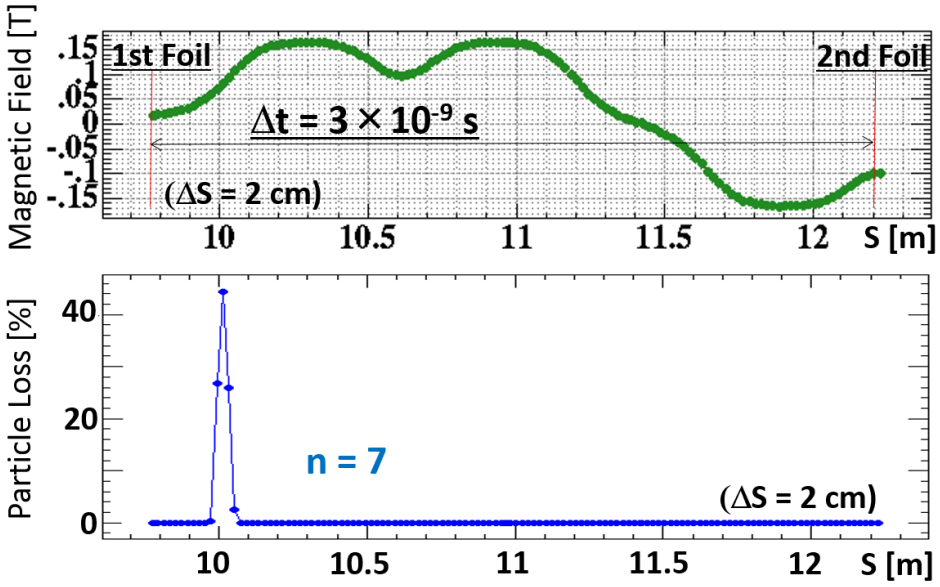

(b) The case of $H^0(7)$

Figure 94: The magnetic field distribution of the SB and the calculated decay points of the $H^0(6)$ and $H^0(7)$. The calculation step is $\Delta s = 2$ cm.

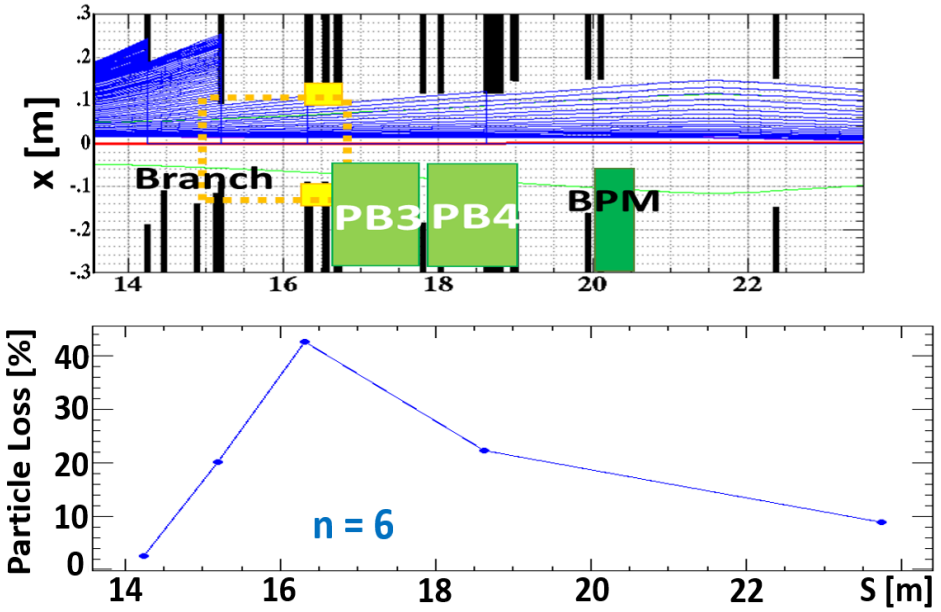

(a) The case of $H^0(6)$

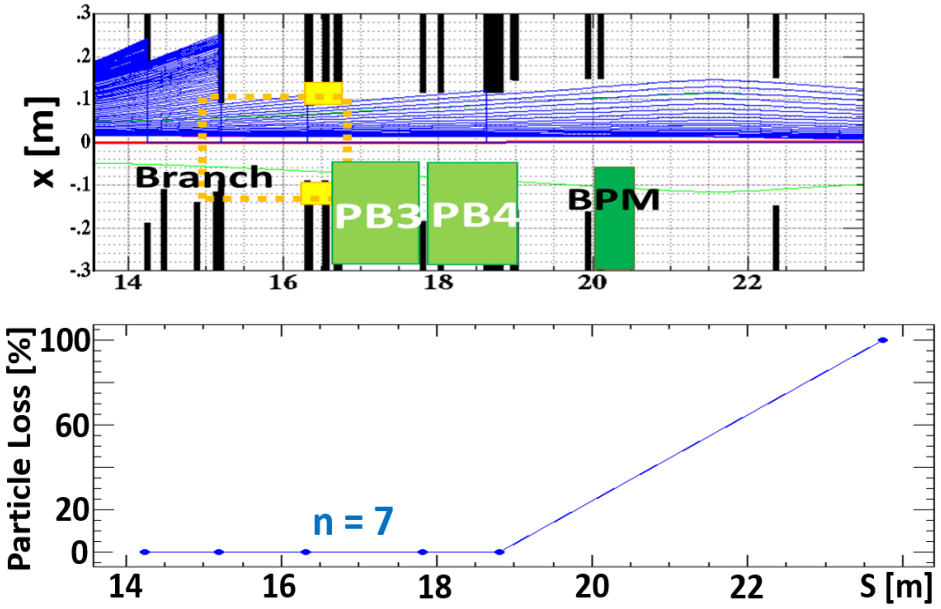

(b) The case of $H^0(7)$

Figure 95: The loss points of the decayed $H^0(6)$ and $H^0(7)$. The upper figures indicate the tracking simulation results corresponding to Fig. 93. The lower figures indicate the loss points.

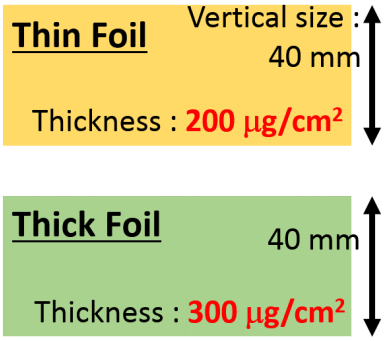

Figure 96: The schematic drawings of the foils adopted to the experiment.

First, the amount of the H^0 led to H^0 dump was detected by using special method [42]. As a result, that were 3.18 % and 0.683 % of the injection beam for the thin foil and the thick foil, respectively. By adopting these result to the table of the charge-exchange efficiency, the calculation results of the foil thickness were 211.8 μg/cm^2 and 295.2 μg/cm^2, respectively. From the results of Fig. 11, it could be considered that the state of detected H^0 were n = 1 to n = 5. By assuming that the yield of the excited state is proportional to n^{-3} shown in Eq. 4, the amount of the $H^0(6)$ for the thin foil and the thick foil were estimated to be 0.0124 % and 0.002663 %, respectively. The estimated power of decayed H^0 which could cause beam loss were 16.5 W and 3.55 W at 1 MW output power, respectively.

Figure 97 shows the SB and PB current patterns during the experiment. The injection beam position was fixed at the 100 π painting point. The horizontal foil edge distance from the injection center was 13 mm. The vertical foil size was 40 mm. The injection period was 100 μs. In order to keep the ring orbit height and to increase the foil hitting probability as much as possible during injection period, the PB height was fixed during 400 μs. The linac peak current was 15 mA and the only fundamental RF was applied. Figure 98 shows the time structure of the loss at the outside of the PB4 and the inside of the BPM. As shown, the loss for the thin foil was larger than that for the thick foil during injection at PB4 because the H^0 increased. On the other hand, the loss for the thin foil was lower during 100 to 400 μs because the scattered beam decreased. The loss for the thin foil was 2.1 times of that for the thick foil during the injection period.

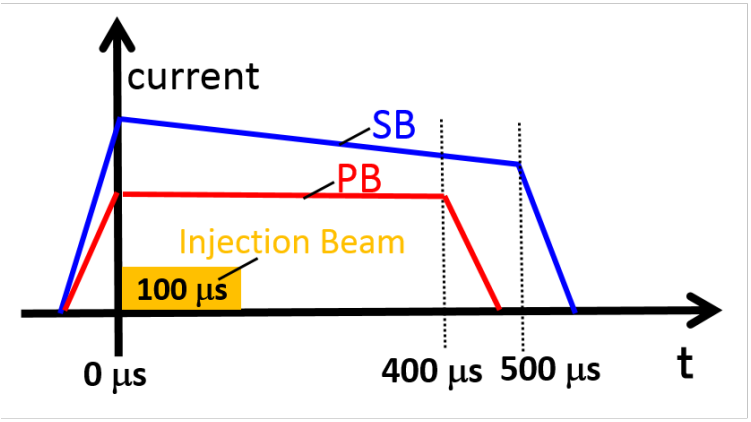

Figure 97: The SB and PB current patterns during the experiment.

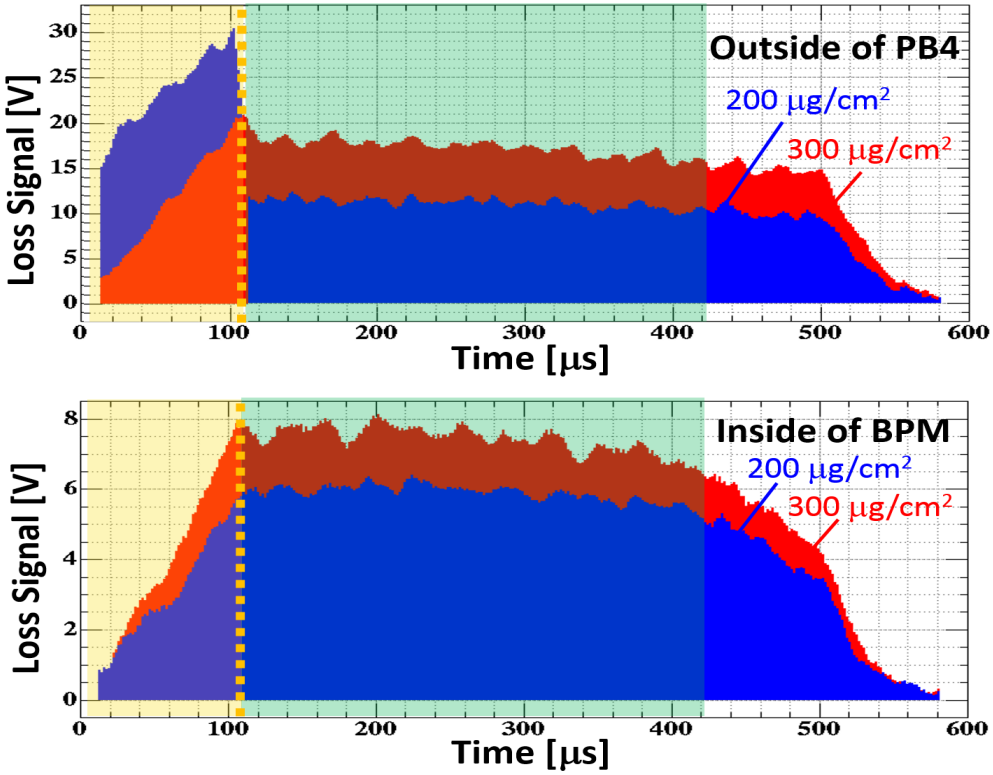

Figure 98: The time structure of the loss at the outside of the PB4 and the inside of the BPM. The upper figure indicates the loss at the outside of the PB4. The lower figure indicates the loss at the inside of the BPM. The blue and red plots indicate the loss for Thin foil and Thick foil, respectively. The yellow meshes indicate the injection period. The green meshes indicate the time range when the PB current was constant.

The loss ratio between the decayed H^0 and the scattered beam at the outside of the PB4 was discussed using the result of Fig. 98. First, the decrement of the scattering

beam loss owing to thin foil was estimated. From the Fig. 98, when the thin foil was adopted, the loss decreased both during and after injection period at the inside of the BPM. In addition, the loss ratio between the thin foil and the thick foil during injection period indicated yellow mesh and that after injection period indicated green mesh were almost same. Specifically, the loss for the thin foil was 80 % of that for the thick foil. Therefore, the decrement of the scattering beam loss was estimated at 80 % assuming that the decayed H^0 was not mixed at the inside of the BPM. Second, the increment of the decayed H^0 owing to thin foil was estimated. As explained above, the amount of the $H^0(6)$ for the thin foil was 4.7 times of that for the thick foil. Third, the number of foil hit per particle was estimated during the injection period. Because the increment of the loss was almost proportional to time, it was assumed that all circulating beam collide with foil every turn during the injection period. Therefore, the number of foil hit per particle was estimated at 30.5 because the injection turns were 61 corresponding to 100 μs.

Finally, the loss ratio between the decayed H^0 and the scattered beam at the outside of the PB4 was estimated using parameters explained above. When the ratio of the decayed H^0 and the scattered beam were defined x and y, respectively for the thick foil, the equations was constructed as follow: $x + y = 1$ and $4.7x + 0.8y = 2.1$. The results were $x = 33.3$ % and $y = 66.7$ %. By dividing y by the number of foil hits per particle, the loss ratio without the foil re-collision was estimated. The loss ratio was $15.2 : 1$ for the thick foil. On the other hand, it was $71.4 : 0.8$ for the thin foil. Because the number of foil hits per particle was approximately 20 for the present 100 π Correlated painting, the estimated ratio were $15.2 : 20$ and $71.4 : 16$ for the thin foil and the thick foil, respectively. Therefore, when the the thin foil is adopted, the decayed H^0 become main issue instead of the scattering beam loss. For Thin foil, the amount of the loss was also 2.5 times of that for the thick foil.

From the result of Fig. 95, it is estimated that at most 22 % of $H^0(6)$ loss at the outside of the PB4 because the loss become maximum in the case of PB off shown in Fig. 95. Therefore, at most 3.63 W of $H^0(6)$ can loss when the thin foil is adopted. This value is not negligible. In addition, the residual dose at the inside of the BPM will become only just 80 %. On the other hand, the residual dose at the H^0 bump will become 6.37 times not only the increase of the loss at the outside of the ring. Therefore, the reduction of the foil thickness is not suitable for the reduction of the loss at downstream area.

For the RCS operation, the foil thickness is 340 μg/cm^2. The amount of the H^0 was 43.7 % of that for the thick foil. Therefore, approximately 75 % of the loss was the scattering beam loss.

7 Conclusion

To efficiently perform experiments in particle, nuclear, and condensed matter physics, a high intensity proton accelerator is greatly desired in the world. To achieve high intensity, the reduction or control of the beam loss is very important because the beam loss causes activation of the equipment. In particular, in the high intensity accelerator, some new beam loss sources appear that are not a problem in the low-intensity accelerator. Therefore, research on these beam loss mechanisms is necessary. In this thesis, the research around a countermeasure against the beam loss caused by the multi-turn charge-exchange injection, which is an essential scheme for a high intensity synchrotron or storage ring, was performed using the J-PARC RCS as an example.

1. It was indicated from the example of the RCS that large-angle foil scattering beam loss could become an issue associated with the high intensity case for the first time in the world. In the RCS, the unexpected beam loss was detected downstream of the injection point. For example, the residual dose was 6.2 mSv/h on contact at the inside of the BPM after 200 kW operation with an injection energy of 181 MeV. In the RCS, this beam loss limits the attainable beam intensity. Using a high precision simulation and focusing on foil scattering, it was indicated that this significant loss was caused by large-angle charge-exchange foil scattering of the injection and circulating beams during the injection period. The probability of the large-angle scattering that causes the loss was very low of 10^{-5} in the RCS. Therefore, this was a special loss for the high intensity proton synchrotron and ring.

2. The countermeasure against the large-angle scattering beam loss was discussed for the RCS. Because this loss cannot be handled in principle, localization was performed using a collimator. Using a beam tracking simulation, a localization point was decided. Thus, the whole of the H^0 branch duct, covered with a radiation shield, was constructed as a new collimator. Because particles scattered in the horizontal plane should be removed, two absorbers were included on the right and left side of the duct. In addition, the angle was appended to their surface because the scattered particles which should be removed collided with those having horizontal angles. An adjustment mechanism for the absorber position and angle was also added.

3. The realistic simulation model was constructed through the combining of some simulation codes. The SIMPSONS code was applied to simulate the beam distribution at the foil. The SAD code was used for beam tracking. The GEANT4 code simulated the interaction between the particles and absorber. In addition, a simplification method was applied to obtain the large statistics because the probability of the large-scattering event was very low.

4. The method for optimizing the absorber angle was developed. The relation between the absorber and the angle of the colliding particle had not been considered thoroughly before. However, in this thesis, it was indicated that the absorber and particle angles should be adjusted in parallel for efficient localization using simulation. Also, a beam-based angle optimization method called LMM was developed.

5. The localization effect was confirmed to be successful by experiment. The absorber position and angle were optimized. Specifically, the LMM, our newly developed method, was established. Thus, the residual dose was suppressed to 900 μSv/h on contact at the inside of the BPM where the loss was largest after 300 kW operation.

6. The comparison between the experiment and simulation results was discussed. By adopting the detected injection beam size and the time function of the painting, the simulation results corresponded with the experimental results. In other words, the validity of the simulation model was confirmed. Using this model, the residual dose was estimated for future 1MW operation. The result confirmed that the residual dose around the BPM would be approximately 1 mSv/h, which is an acceptable level for accelerator maintenance. In other words, the beam loss issue, which originally prevented the achievement of 1 MW power, was solved. Therefore, as a result of this research, further evolution of particle, nuclear and condensed matter physics through experiments in the J-PARC is expected.

7. The modification of the painting injection was discussed for higher beam intensities. Thus, it was indicated that further suppression of the loss was possible through extension of the painting area and the modification of the painting time function.

This thesis comprehensively discusses the large-angle scattering beam loss and its countermeasure for the first time in the world. In particular, a localization method of the loss was established. Because the lattice design will not be prevented by large-angle scattering beam loss as long as the collimator space is kept in the downstream area of the injection point, this method will be standard for future high intensity proton synchrotrons and rings.

Acknowledgements

First, I would like to express my great gratitude to my supervisor, Prof. M. Kinsho of Tohoku University for his advice, full support and detail discussion during this thesis work. I am very glad that I was gave the opportunity to develop the key device of the RCS and to be educated about the whole of accelerator physics.

I would like to express my gratitude to Dr. K. Yamamoto, and Dr. M. Yoshimoto of Japan Atomic Energy Agency (JAEA) for the development of the new collimator, their extensive advice, full support and detail discussion during this thesis. I am very glad that I could experience not only the operation of the device but also the mechanical construction.

I would like to express my gratitude to Dr. H. Harada of JAEA for his extensive advice, full support and detail discussion during this thesis. Particularly, the construction of the experimental detection system and the development of the simulation model were performed thanks to his great support. I am very glad that I could study about the accelerator research from him.

I would like to express my gratitude to Dr. H. Hotchi, Dr. P.K. Saha, Dr. Y. Shobuda and Dr. K. Okabe of JAEA and members of RCS beam commissioning group for their extensive advice, full support and detail discussion during this thesis. Particularly, this thesis work was based on their tireless work of beam commissioning. I am very glad that I could research in the highest quality commissioning.

I would like to express my gratitude to Dr. S. Machida of Rutherford Appleton Laboratory for his advice and detail discussion during improvement of RCS simulation model. Particularly, his simulation code made this research more precise than ever.

I would like to express my gratitude to Dr. J. Kamiya of JAEA and members of vacuum group for their educational advice, full support and detail discussion during this thesis. Particularly, the vacuum test of the new duct was performed with their great cooperation.

I would like to express my gratitude to Dr. F. Tamura, Dr. M. Yamamoto of JAEA and members of RF group for their educational advice, full support during RCS beam commissioning and the experiment of this thesis. I would like to express my gratitude to Dr. T. Takayamagi of JAEA and members of magnet group for their educational advice, full support during this thesis. I wish to appreciate Dr. N. Tani of JAEA for position survey multiple times.

I would like to express my gratitude to Dr. N. Hayashi, Dr. S. Hatakeyama of JAEA and members of monitor group for their educational advice, full support during this thesis. I wish to appreciate Mr. Iwama for his support to preparing device.

I would like to express my gratitude to Mr. O. Takeda, Dr. Y. Yamazaki of JAEA and members of system commissioning group for full support during this thesis. I wish to appreciate Mr. Tobita for his support to the confirmation of the alignment.

I would like to express my gratitude to Ms. M. Aramaki of JAEA for full support of working environment.

I also would like to express my great gratitude to Prof. O. Hashimoto, Prof. H. Tamura and Prof. S. N. Nakamura of Tohoku University and members of nuclear physics group for educational advice, full support and discussion during my undergraduate days.

I am very glad that I could experience the basic education of the nuclear physics and experimental method. It became a good chance to have an interest in accelerator physics. I wish to appreciate Dr. M. Kaneta for his education about basic programing.

I would like to express my gratitude to my colleagues working individually now. Their encouragement gave me high motivation.

Finally, I express my thanks to my family.

A The Linear betatron motion and the tracking method of SIMPSONS

In an accelerator, particles oscillate around the closed orbit in the transverse plane. This oscillation is called "betatron oscillation". Therefore, a curvilinear coordinate system shown in Fig. 99 is usually applied for particle motion in synchrotrons.

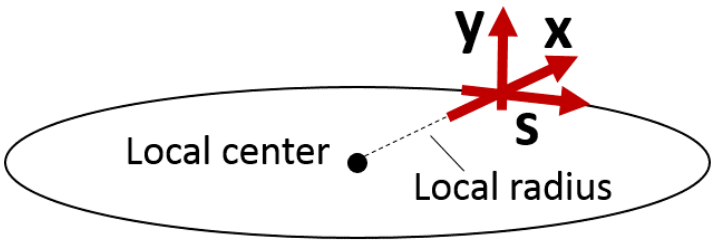

Figure 99: A curvilinear coordinate system.

When the magnetic field is stable and B_s is 0, B_x and B_y can be expanded as follow.

$$\frac{1}{(B\rho)}(B_y + jB_x) = \sum_{n=0}^{\infty}(b_n + ja_n)(x+jy)^n \tag{8}$$

$$b_n = \frac{1}{(B\rho)n!}\frac{\partial^n B_y}{\partial x^n} \tag{9}$$

$$a_n = \frac{1}{(B\rho)n!}\frac{\partial^n B_x}{\partial x^n} \tag{10}$$

where ρ is bending radius, b_n indicates the $2(n+1)$-pole component and a_n indicates the skew-component. When only dipole and quadrupole components are taken, the linearized betatron equation of motion are as follows.

$$x'' + (\frac{1}{\rho^2} + \frac{1}{(B\rho)}\frac{\partial B_y}{\partial x})x = 0 \tag{11}$$

$$y'' - \frac{1}{(B\rho)}\frac{\partial B_y}{\partial x}y = 0 \tag{12}$$

The solution of this equation can be expressed as the transfer matrix M which is shown as follow.

$$\begin{pmatrix} x_2 \\ x_2' \end{pmatrix} = M(s_2|s_1)\begin{pmatrix} x_1 \\ x_1' \end{pmatrix} \tag{13}$$

For example, the transfer matrix for a sector dipole magnet whose edge cross a reference orbit at right angles is

$$M_x = \begin{pmatrix} \cos\phi & \rho\sin\phi \\ -(1/\rho)\sin\phi & \cos\phi \end{pmatrix} \tag{14}$$

$$M_y = \begin{pmatrix} 1 & \rho\phi \\ 0 & 1 \end{pmatrix} \tag{15}$$

where ϕ and ρ are bending angle and radius, respectively. The transfer matrix for a horizontal focusing quadrupole is

$$M_x = \begin{pmatrix} \cos\sqrt{|K_1|}l_{mag} & \frac{1}{\sqrt{|K_1|}}\sin\sqrt{|K_1|}l_{mag} \\ -\sqrt{|K_1|}\sin\sqrt{|K_1|}l_{mag} & \cos\sqrt{|K_1|}l_{mag} \end{pmatrix} \tag{16}$$

$$M_y = \begin{pmatrix} \cosh\sqrt{|K_1|}l_{mag} & \frac{1}{\sqrt{|K_1|}}\sinh\sqrt{|K_1|}l_{mag} \\ \sqrt{|K_1|}\sinh\sqrt{|K_1|}l_{mag} & \cosh\sqrt{|K_1|}l_{mag} \end{pmatrix} \tag{17}$$

$$K_1 = \frac{1}{(B\rho)}\frac{\partial B_y}{\partial x} > 0 \tag{18}$$

where l_{mag} is the magnet length. The particle tracking can be achieved using the transfer matrix for each magnetic component.

For the SIMPSONS, it is inconvenient that the magnet components have its length because particles are moved to the $+s$ direction with the time step of Δt for the self-consistent calculation of the space charge force and importing the time variable components. Therefore, the thin-lens approximation with $l \to 0$ is applied. For example, the transfer matrix for a horizontal focusing quadrupole reduces to

$$M_x = \begin{pmatrix} 1 & 0 \\ -1/f & 1 \end{pmatrix} \quad M_y = \begin{pmatrix} 1 & 0 \\ 1/f & 1 \end{pmatrix} \tag{19}$$

$$f = \lim_{l\to 0}\frac{1}{|K_1|l_{mag}}. \tag{20}$$

As shown, the matrix add the kick angle indicated $1/f$. In the SIMPSONS, the particles are tracked in the drift space and are added the kick angle at the magnet position. This is called "kick and drift".

Figure 100 shows the kick and drift scheme in the SIMPSONS. For the Δt, the drift length is defined as

$$l_s = v_s \Delta t. \tag{21}$$

For the particle of No. 1, the coordinates are transformed as

$$s_2 = s_1 + l_s \tag{22}$$

$$x_2 = x_1 + l_s x_1' \tag{23}$$

$$x_2' = x_1' \tag{24}$$

because the particle passes through only the drift space. On the other hand, the particle of No. 2 passes through the magnet during Δt. In this case, the tracking of the drift space is divided and the kick angle is added at the magnet position. The kick angle by the $2(n+1)$-pole magnet are

$$\Delta x_n' = \mathrm{Re} \mid (b_n + ja_n)(x_1 + jy_1)^n \mid l_{mag} \tag{25}$$

$$\Delta y_n' = (-1)^n \mathrm{Im} \mid (b_n + ja_n)(x_1 + jy_1)^n \mid l_{mag}. \tag{26}$$

When the skew component is 0, the kick angle by the quadrupole magnet ($n = 1$) are

$$\Delta x' = b_1 x_1 \tag{27}$$

$$\Delta y' = -b_1 y_1 \tag{28}$$

and the kick angle by the sextuple magnet ($n = 2$) are

$$\Delta x' = b_2 x_1^2 - b_2 y_1^2 \quad (29)$$

$$\Delta y' = 2 b_2 x_1 y_1. \quad (30)$$

After all, the horizontal and vertical angle is changed as follows.

$$x_2' = x_1' + \Delta x' \left(\frac{p_0}{1 + \frac{\Delta p}{p_0}} \right) \quad (31)$$

$$y_2' = y_1' + \Delta y' \left(\frac{p_0}{1 + \frac{\Delta p}{p_0}} \right) \quad (32)$$

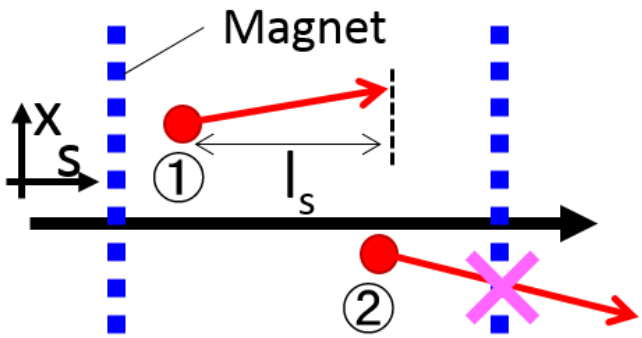

Figure 100: The kick and drift scheme in the SIMPSONS. The blue dashed lines indicate the magnet components. The red circles indicate the particles. The pink mark indicates the kick point.

Figure 101 shows the focusing components by the bending magnet and the rectangular bending magnet model for the SIMPSONS. The sector bending magnet has the horizontal focusing component which correspond with (2,1) component of Eq. 14. The rectangular bending magnet has the edge focusing components additionally at the entrance and exit. The bending magnet of the RCS is rectangular type. In the SIMPSONS, the bending magnet are divided into 5 parts as shown in the bottom of Fig. 101. Specifically, the horizontal focusing component is divided into 5 parts with thin-lens and the edge focusing components are arranged at the entrance and exit of the bending magnet section.

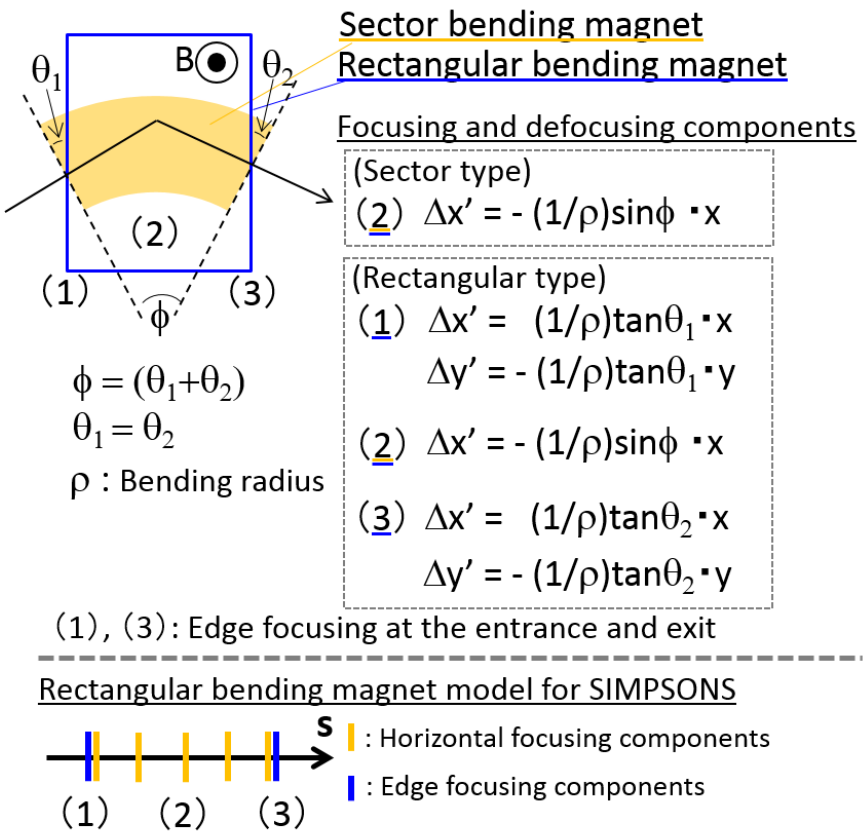

Figure 101: The focusing components by the bending magnet and the rectangular bending magnet model for SIMPSONS.

B Calculation method of the Poisson equation in SIMPSONS

The calculation method of the Poisson equation in SIMPSONS is described in the following [30] [32] [43]. In the cylindrical coordinates, the potential is expanded with the harmonic components of the azimuthal direction. The Poisson equation is solved with a boundary condition of circular cross sectional beam pipe.

Figure 102 shows the cylindrical mesh. In the SIMPSONS, the mesh size is $N_z = 50$, $N_r = 50$, and $N_\varphi = 64$. The number of macro-particles is 5×10^5. The potential and the electric field are calculated at each grid point.

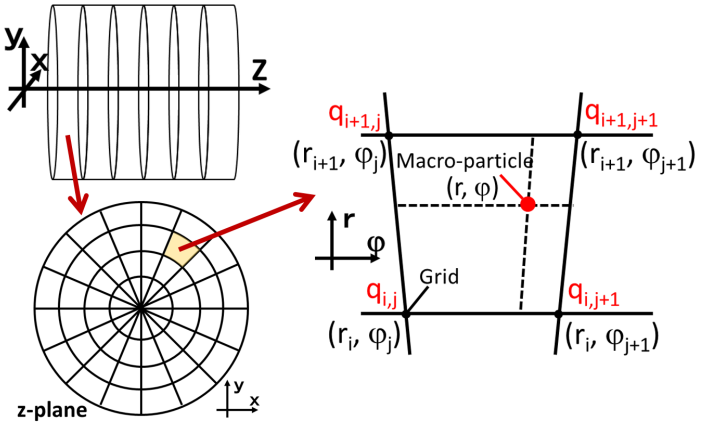

Figure 102: The cylindrical mesh.

The scalar potential satisfies the following formula in the Lorenz gauge.

$$E_r = \frac{\partial \phi}{\partial r},\ E_\varphi = \frac{1}{r}\frac{\partial \phi}{\partial \varphi},\ E_z = \frac{\partial \phi}{\partial z}. \tag{33}$$

$$\Delta\phi - \varepsilon_0\mu_0\frac{\partial^2\phi}{\partial t^2} = -\frac{\rho}{\varepsilon_0\gamma^2} \tag{34}$$

where the ε_0, μ_0, and ρ indicates the dielectric constant in vacuum, the magnetic permeability in vacuum, and the charge, respectively. A contribution from the magnetic field is taken into account with a $1/\gamma^2$ factor. Because the longitudinal beam size is approximately 3 orders large compared with the transverse beam size, the approximation is adopted as following formula.

$$\begin{aligned} \Delta\phi &= \frac{1}{r}\frac{\partial}{\partial r}\left(r\frac{\partial\phi}{\partial r}\right) + \frac{1}{r^2}\frac{\partial^2\phi}{\partial\varphi^2} + \frac{\partial^2\phi}{\partial z^2} \\ \frac{\partial^2\phi}{\partial z^2} &\sim \varepsilon_0\mu_0\frac{\partial^2\phi}{\partial t^2} \ll \frac{1}{r}\frac{\partial}{\partial r}\left(r\frac{\partial\phi}{\partial r}\right) + \frac{1}{r^2}\frac{\partial^2\phi}{\partial\varphi^2} \end{aligned} \tag{35}$$

As a result, the Poisson equation is formed as following formula.

$$\frac{1}{r}\frac{\partial}{\partial r}\left(r\frac{\partial\phi}{\partial r}\right) + \frac{1}{r^2}\frac{\partial^2\phi}{\partial\varphi^2} = -\frac{\rho}{\varepsilon_0\gamma^2} \tag{36}$$

In order to solve this equation, the charge and the potential are Fourier transformed in the azimuthal direction.

$$\phi = \sum_{m=-\infty}^{\infty} \phi_m \exp(im\varphi) \tag{37}$$

$$-\frac{\rho}{\varepsilon_0 \gamma^2} (\equiv n) = \sum_{m=-\infty}^{\infty} n_m \exp(im\varphi) \tag{38}$$

with the inverse transform,

$$\phi_m = \frac{1}{2\pi} \int_0^{2\pi} \phi(r, z, \varphi) \exp(-im\varphi) d\varphi \tag{39}$$

$$n_m = \frac{1}{2\pi} \int_0^{2\pi} n(r, z, \varphi) \exp(-im\varphi) d\varphi \tag{40}$$

For each m-mode, the following equation is satisfied using the relation of $n_{-m} = {n_m}^*$.

$$n_m(r, z) = \frac{1}{r} \frac{\partial}{\partial r} \left(r \frac{\partial}{\partial r} \phi_m(r, z) \right) - \frac{m^2}{r^2} \phi_m(r, z) \tag{41}$$

When $m \geq 0$, the general solution is as follow.

$$\phi_m = \alpha \left(\frac{r}{b} \right)^m + W(r) - \left(\frac{r}{b} \right)^m W(b) \tag{42}$$

where b indicates the boundary radius, which means beam pipe radius. Using the boundary conditon ($\phi_m = 0$ at $r = b$), the equation is formed as follow.

$$\phi_m = W(r) - \left(\frac{r}{b} \right)^m W(b) \tag{43}$$

when $m = 0$,

$$W(r, z) = \int_0^r \ln \frac{r}{r'} n_m(r', z) r' dr' \tag{44}$$

and when $m \neq 0$,

$$W(r, z) = \frac{r^m}{2m} \int_0^r r'^{(1-m)} n_m(r', z) dr' - \frac{r^{-m}}{2m} \int_0^r r'^{(1+m)} n_m(r', z) dr' \tag{45}$$

where $\phi_{-m} = {\phi_m}^*$ is used to calculate ϕ_m for $m < 0$. As a result, the electric field can be calculated as follows.

$$\begin{aligned} E_r &= \sum_{m=-\infty}^{\infty} \frac{\partial}{\partial r} \phi_m \exp(im\varphi) \\ E_\varphi &= \sum_{m=-\infty}^{\infty} \frac{1}{r} \frac{\partial}{\partial \varphi} \phi_m \exp(im\varphi) \\ E_z &= \sum_{m=-\infty}^{\infty} \frac{\partial}{\partial z} \phi_m \exp(im\varphi) \end{aligned} \tag{46}$$

The calculated electric fields are allocated to the macro-particles using the Area Weighting Method. The momentum of the macro-particle is changed from the state of 1 to 2 by the impulse as follows.

$$p_{s2} = p_{s1} + E_{z-macro}\Delta t \tag{47}$$

$$p_{x2} = p_{x1} + E_{x-macro}\Delta t \tag{48}$$

$$p_{y2} = p_{y1} + E_{y-macro}\Delta t \tag{49}$$

where $E_{z-macro}$, $E_{x-macro}$, $E_{y-macro}$ indicate the allocated electric field.

C Comparison between the experimental results and the SIMPSONS simulation

In the RCS, the SIMPSONS simulations are performed on the basis of the measured beam parameters and the imperfections. For example, a leakage field and time variable ripples of some magnetic fields are added in the simulation. And then, simulation results are compared with the experimental results in order to understand the high-intensity beam behavior and the loss mechanism. By the continuous improvement of the SIMPSONS, the simulation results corresponds well with the experimental results. In other words, the consistent results between the measurement and the simulation ensure the accuracy of the SIMPSONS.

The results of the comparison between the measurement and the SIMPSONS simulation were described in Ref. [44] in detail. The injection beam energy was 181 MeV then. In this article, the beam survival rate, the time structure of the beam loss and the longitudinal distribution which corresponds to bunching factor were compared for 420 kW equivalent beam. In particular, some transverse and longitudinal painting patterns were applied in order to modify the charge density. As a result, the simulation results corresponded well with the measured results. For example, the beam survival rate which depends on the painting pattern corresponded with the measured results.

For the SIMPSONS, the comparison and the improvement of the code is performed continuously. Figure 103 shows the time structures of the beam loss in the case of 400 MeV injection energy. In this experiment, 100 π Correlated transverse paint was applied. The beam intensity was modified by thinning out the injection beam during the multi-turn injection. As shown, the simulation result corresponded with the measured results. In addition, the comparison of the coherent tune depression caused by the space charge force was also performed [45].

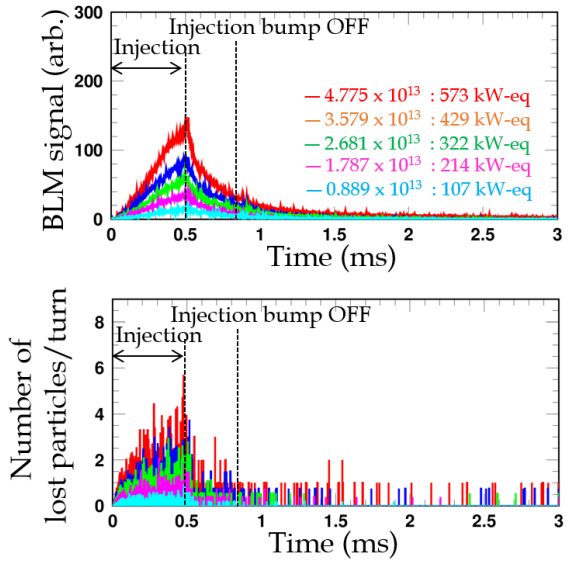

Figure 103: The time structures of the beam loss [5]. The upper and lower figures indicate the experimental and simulation results, respectively.

References

[1] Accelerator Technical Design Report for High-Intensity Proton Accelerator Facility Project, JAERI Report No. JAERI-Tech 2033-004 and KEK Report No. 2002-13.

[2] J. Wei, *et al.*, Phys. Rev. ST Accel. Beams **3** (2000) 080101.

[3] H. Hotchi, *et al.*, Phys. Rev. ST Accel. Beams **12** (2009) 040402.

[4] H. Hotchi, *et al.*, Prog. Theor. Exp. Phys. **2012**, 02B003.

[5] H. Hotchi, *et al.*, in Proceedings of the 54^{th} ICFA Advanced Beam Dynamics Workshop on High-Intensity and High-Brightness Hadron Beams (HB2014), East Lansing, USA, 2014 (FRIB, East Lansing, 2014). (to be published)

[6] Y. Saito, M. Kinsho and Z. Kabeya, Journal of Physics: Conference Series **100** (2008) 092020.

[7] C. Ohmori, *et al.*, in Proceedings of the 2^{nd} International Accelerator Conference, San Sebastian, Spain, 2011 (IPAC11), pp. 2885–2887.

[8] K. Yamamoto, Ph.D. thesis.

[9] H. Harada, the text of the high-energy accelerator seminar (OHO′2010), Chap–8 (2010).

[10] H. Harada: KEK Report No. 2009–7.

[11] I.M.Kapchinskij and V.V.Vladimirskij : Limitations of Proton Beam Current in a Strong Focusing Linear Accelerator Associated with the Beam Space Charge, Proceedings of the Second International Conference on High Energy Accelerators, pp. 274–288, 1959.

[12] F. Tamura, *et al.*, Phys. Rev. ST Accel. Beams **12** (2009) 041001.

[13] M. Yamamoto, *et al.*, Nucl. Instr. and Meth. A, 621 (2010) 15–32.

[14] I. Sugai, *et al.*, Nucl. Instr. and Meth. A, 521 (2004) 192–196.

[15] R.J. Damburg and V.V. Kolosov,"Theoretical Studies of Hydrogen Atoms in Electrical Fields" in "Rydberg States of Atoms and Molecules", R.F. Stebbings, F.B. Dunning, Cambridge Univ. Press, 1983, pp. 31–71.

[16] M. S. Gulluey, et al, Phys. Rev. A **53** (1996) 3201.

[17] JHF Project Office : KEK Report 97-16, JHF-97-10, 1998-3.

[18] W. Chou, *et al.*, Nucl. Instr. and Meth. A, 590 (2008) 1–12.

[19] K. Yamamoto, *et al.*,in Proceedings of the 1^{st} InterNational Particle Accelerator Conference (IPAC10), Kyoto, Japan, 2010 (ICR, Kyoto, 2010), pp. 2842–2844.

[20] P. K. Saha, in Proceedings of the 46^{th} ICFA Advanced Beam Dynamics Workshop on High-Intensity and High-Brightness Hadron Beams (HB2010), Morschach, Switzerland (2010), pp. 324–328.

[21] http://acc-physics.kek.jp/SAD/

[22] K.Oide, KEK Proceedings 93–6 (1993).

[23] http://geant4.cern.ch/

[24] L. Urban, A multiple scattering model, CERN-OPEN-2006-077, Dec. 2006.

[25] H.W. Lewis. Phys. Rev. **78** (1950) 526.

[26] S. Kato, J. Kamiya, K. Yamamoto, M. Yoshimoto, and M. Kinsho, J. Vac. Soc. Jpn. 55 (2012) No. 4, 160–163.

[27] http://www-ap.fnal.gov/MARS/

[28] H. Harada, Private Communication.

[29] S. Machida, SSCL-PREPRINT-197 (1993).

[30] S. Machida, M. Ikegami, in Proceedings of the Workshop on Space Charge Physics in High Intensity Hadron Rings, Long Island, 1998, and KEK Preprint 98–189, Nov. 1998, A.

[31] T. Sato, *et al.*, J. Nucl. Sci. Technol. 50:9, 913–923 (2013).

[32] S. Machida, the text of the high-energy accelerator seminar (OHO′2000), Chap–3, pp. 15–17 (2000).

[33] S. Kato, *et al.*, Phys. Rev. ST Accel. Beams **16** (2013) 071003.

[34] P.K. Saha, *et al.*, Phys. Rev. ST Accel. Beams **16** (2013) 120102.

[35] P.K. Saha, *et al.*, in Proceedings of the 54^{th} ICFA Advanced Beam Dynamics Workshop on High-Intensity and High-Brightness Hadron Beams (HB2014), East Lansing, USA, 2014 (FRIB, East Lansing, 2014). (to be published)

[36] Y. Shobuda, *et al.*, Phys. Rev. ST Accel. Beams **12** (2009) 032401.

[37] J. Kamiya, *et al.*, Nucl. Instr. and Meth. A, 763 (2014) 329–339.

[38] H. Hotchi, *et al.*, Nucl. Instr. and Meth. A, 778 (2015) 102–114.

[39] S. Kato, *et al.*, JPS Conf. Proc. 1, 013015 (2014).

[40] M. Reiser, Theory and Design of Charged Particle Beams (Wiley, New York, 1994), pp. 358–364.

[41] K. Okabe, Private Communication.

[42] P.K. Saha, *et al.*, Nucl. Instr. and Meth. A, 776 (2015) 87–93.

[43] P.M. Morse and H. Fechback, "Methods of Theoretical Physics", MacGrew-Hill, 1953.

[44] H. Hotchi, *et al.*, Phys. Rev. ST Accel. Beams **15** (2012) 040402.

[45] H. Hotchi, *et al.*, in Proceedings of the 5^{th} International Accelerator Conference, Dresden, Germany, 2014 (IPAC14), pp. 899–903.